MASTER OF SCIENCE

Implementation of a near-wake model to improve the radial induction distribution of an existing BEM code validated by comparison to CFD results

Qasim Manzoor
2017 August 08

EWEM

SIEMENS Gamesa
RENEWABLE ENERGY

DTU

TU Delft

Implementation of a near-wake model to improve the radial induction distribution of an existing BEM code validated by comparison to CFD results

MASTER OF SCIENCE THESIS

For obtaining the degree of Master of Science in Engineering Wind Energy at Technical University of Denmark and in Aerospace Engineering at Delft University of Technology.

Qasim Manzoor

08 August, 2017

European Wind Energy Master - EWEM

Abstract

The Blade Element Momentum (BEM) method is a widely used model for rotor performance and aeroelastic calculations but it has assumptions in its formulation which limit its accuracy. The theoretical background of these limitations has been studied and an improvement in the form of the Near Wake Model (NWM) has been identified. The model adds near wake vorticity effects to the BEM along with modeling the interdependence of the different annular elements. A coupled model based on the NWM has been developed for steady state analysis of turbine rotors. The model performance has been analyzed for the DTU 10 MW Reference Wind Turbine (RWT) and compared to Computational Fluid Dynamics (CFD) simulations. The comparison has been carried out for even and uneven loading distribution. The uneven loading has been modeled by modifying the chord distribution of the blade. Though the aim was to improve the induction distribution, due to the known difficulties of calculating induction from CFD, the aerodynamic loads were investigated rather than focusing on the induction distribution. For an evenly loaded blade, the loads from the coupled model are improved because of the added flow physics. For uneven loading, the coupled model improves upon the standard BEM, but if modified locally over a large section of the blade to represent the uneven loading, it is seen that the coupled model has a large difference compared to CFD. Finally, for slender blades with uneven loading, the model performs reasonably well showing a significant improvement to the BEM in the in-plane forces and an overall improvement in the out-of-plane forces as well when compared to CFD.

Acknowledgements

My educational journey so far has been everything I ever dreamed of. The European Wind Energy Master has been full of exciting and challenging times, as well as remarkable memories. Writing my thesis at Siemens Gamesa Renewable Energy has definitely been the best way to finalize this masters. I would like to thank my parents for supporting me in all my endeavors, all that I am and all that I will ever be, I owe to them.

The thesis could not have been completed without the valuable feedback and support my supervisors have provided in my work. I would like to thank Helge Madsen, Carlos Ferriera, Maximilian Kosmale and Georg Pirrung for all the interest they have taken in my work. The complex coordination between all the involved members made it difficult at times but I felt like each and every one of them was there for me every step of the way. I would especially like to mention Max for always being available and giving me direction as my daily supervisor, and Georg for always providing amazing insight in my work and answering all my questions time and again. I cannot thank either of them enough.

I would also like to thank Alex Loeven and his team at Siemens Gamesa Renewable Energy who gave me this opportunity and made me feel right at home. The guidance they have provided means a lot to me and every one of them has helped with their kindness and support. I would specially like to thank Morten Quistgård who helped with all the CFD runs and Alejandro Gonzalez whose scientific prowess has helped clarify things more times than I can count.

Lastly, I would like to thank my sister Reem Manzoor, for being my strength in life, and my fiancée Hafsa Mahmood for her confidence in me and for being by my side through all of it.

Contents

List of Figures

List of Tables

List of Acronyms

BEM Blade Element Momentum

BET Blade Element Theory

CFD Computational Fluid Dynamics

DNS Direct Numerical Simulation

DTU Danmarks Tekniske Universitet

FEM Finite Element Method

HawC2 Horizontal Axis Wind turbine simulation Code 2nd generation

LES Large Eddy Simulations

NWM Near Wake Model

RANS Reynolds Averaged Navier Stokes

RWT Reference Wind Turbine

List of Symbols

α Angle of attack

β Angular displacement of vortex arc behind blade

β^* Modified displacement of the vortex element for straight vortices

δ Kronicker delta function

$\dot{m}$ Flow of air through rotor

Γ Circulation

μ_t Turbulent viscosity

∇ Fluid flow gradient operator

ω Rotational speed of rotor

Φ	Geometric parameter for Near Wake Model
ϕ	Inflow angle at blade element
Φ^*	Convection corrected geometry parameter for Near wake model
Φ_{circ}	Near wake model geometry parameter for circular vortices
Φ_C	Root corrected geometric parameter Φ
$\Phi_{straight}$	Near wake model geometry parameter for straight vortices
ρ	Density of air
σ	Solidity of the rotor
$\mathbf{N}$	Matrix of coefficients for standstill correction for negative h/r
$\mathbf{P}$	Matrix of coefficients for standstill correction for positive h/r
θ	Twist angle at the blade element
$\vec{\omega}$	Angular velocity of fluid element
$\vec{\zeta}$	Vorticity
$\vec{x}$	Vector between vortex location and calculation point
A	Rotor Area
a	Axial induction factor
$a^{'}$	Tangential induction factor
a_l	Local induction
a_{FW}	Far wake axial induction factor
a_{NW}	Near wake axial induction factor
a_{ref}	Reference BEM axial induction factor
B	Number of blades in rotor
$c(r)$	Chord distribution
C_d	Drag coefficeint
C_l	Lift coefficient
C_n	Non-dimensional force in normal direction at the blade element

C_P	Power coefficient
C_T	Thrust coefficient
C_t	Non-dimensional force in tangential direction at the blade element
C_{root}	Root correction factor for geometric parameter Φ
$C_{T,red}$	Reduced thrust coefficient
D_w	Induction from the newest trailed vortex element
dw_0	Induction at the lifting line
F	Tip loss factor
f	Convection correction factor for NWM
h	Distance between vortex trailing point and calculation point along blade
k	Turbulent kinetic energy
k_Φ	Interpolation factor for standstill convection correction
k_{FW}	Coupling factor for Near Wake Model
L	Lift Force
M	Torque moment of the rotor
P	Rotor Power
R	Rotor radius
r	Radial distance at which vortex is trailed
S	Blade span
T	Thrust force acting on rotor
u	Velocity at rotor plane
u_1	Velocity in wake downstream of rotor
u_{FW}	Induced velocity from far wake
V_0	Freestream velocity
v_{axial}	Axial component of velocity at blade element
V_{rel}	Relative velocity at the blade element

v_{tan} Tangential component of velocity at blade element

w Induced velocity at blade

W_i Total induction at time step i

$W_{analytical}$ Analytical induced velocity at a blade or wing

W_{tot} Total induced velocity at blade from near and far wake

X_i Slow decaying component of Near wake induction

Y_i Fast decaying component of Near wake induction

Chapter 1

Introduction

Sustainable Energy production has been growing rapidly due to the increasing energy demand of governments, industry and citizens. According to the DTU International Energy report [1], wind energy is the leading renewable energy technology slated to provide up to 34 % of EU electricity by 2030. From an environmental and sustainable perspective wind energy is a very lucrative form of energy and is definitely shaping the future of the global energy map. In the last 25 years, development in wind energy has driven wind turbines to grow massively from sizes of 50 kW in the 1980s to almost 6-8 MW with rotor diameters of up to 180 m at present. Examples of such turbines are seen in the offshore portfolio of companies such as Siemens Gamesa Renewable Energy and MHI Vestas. This significant growth has forced engineering practices in the industry to evolve from simple design rules to sophisticated finite element method (FEM) analyses during the structural design of the wind turbines. This has in turn driven the development of aerodynamic models over the past decades since realistic loads are needed as input for the structural models. The design process has become more and more intricate and interlinked with the rapid growth of the wind industry.

As the process for the design of a turbine has evolved, so too has the process for certification of the design. The approval process for modern wind turbines requires an extensive list of load cases that prove that the wind turbine can withstand a wide range of external wind and wave conditions [2]. The evaluation of these load cases involves up to a few thousand time consuming aeroelastic simulations which tackle the coupled aerodynamic and structural behaviour of the wind turbine. As such the aerodynamic models in these aeroelastic codes need to be computationally fast and efficient. For this reason the Blade Element Momentum method (BEM) proposed by Glauert [3] is still the most widely used aerodynamic model. Over the decades a series of corrections and engineering models have been added to the classic BEM to include more flow physics.

Higher fidelity models like vortex wake models and full scale Computational Fluid Dynamics (CFD) computations are more accurate aerodynamic models which are capable of resolving more of the flow physics. However, this comes at a greater cost in terms of time and computational power. Even with modern day computer clusters, these aerodynamic models can take hours or days to give results and therefore cannot completely replace the BEM method in performing exhaustive aeroelastic simulations. Granted that the BEM method is very fast, its results near the root and tip are fairly different when compared to higher fidelity models especially CFD. A method which is closer to CFD calculations in terms of accuracy while still being fast like the BEM method is therefore a useful utility for aeroelastic calculations.

1.1 Project Aim

In this study, modifications will be identified and incorporated in the BEM method to improve the results compared to CFD. The focus will be on the calculation of the induction distribution which is an important parameter in the estimation of loads and thus a cornerstone in the iterative BEM process. Accurately calculating the induction distribution is crucial for gauging the performance of a wind turbine rotor. The BEM method gives an axial induction distribution that is too simplified in comparison to CFD codes. Modifications to the BEM method need to be incorporated to improve its accuracy. As such, one modification in the form of the Near Wake Model (NWM) [4] will be implemented to

see the potential benefits of taking into account the induced vorticity due to the near wake of the turbine. Thereafter possible recommendations will be made to further improve the fit between CFD and BEM by a critical analysis of the flow physics defining the differences of the observations.

The research objective is to improve the induction distribution from the Blade Element Momentum method as compared to CFD by incorporating modifications to an existing BEM code and validating against CFD. One particular modification that will be looked at is the Near-Wake model [5] and the effects of the near wake on the induction distribution. These will be validated against CFD runs for the DTU 10 MW reference turbine [6]. Additionally it has been seen that the disparity between CFD and BEM is greater in the case of uneven load distributions and this will be one important test case for the new model. The results will provide an insight into the shortcomings of the BEM method and a solid explanation of the underlying physics behind the differences will pave the way for further improvements. Further, the effects near the tip of the blade and uneven load distributions are interesting cases to study with this coupled implementation of the BEM and near-wake model.

1.2 Research Questions

In order to achieve the project aim and to steer the efforts of the research in the correct direction a set of core research questions are formulated. For the current study there are two important questions that need to be answered. First, *Which modifications can be implemented to bridge the gap between BEM and CFD results for the induction distribution of the rotor.* Second, *Whether or not the near wake model can satisfactorily accomplish this task?.* These questions can further be divided into the following sub-questions:

- What are the implications of the assumptions made in BEM method?
- What are the different methods and corrections that have been used to augment the standard BEM method?
- How does the near wake model add to the flow physics to counter the assumptions in BEM?
- Does the near wake model improve the induction and load distribution for the case of unevenly loaded blades?
- What are the limitations of the near wake model? How can these be overcome or improved?
- How much of the flow physics is captured and resolved by CFD simulations?
- Can the differences in the results from CFD and the improved BEM be attributed to physical phenomena?

The formulation of the research questions allows a more concentrated search for information in the right direction and establishes the relevance of the thesis and what it aims to achieve.

1.3 Research Framework

The research framework allows a schematic representation of the research objective and links how the different phases are connected and the logical steps involved in the research. The Figure 1.1 shows the framework.

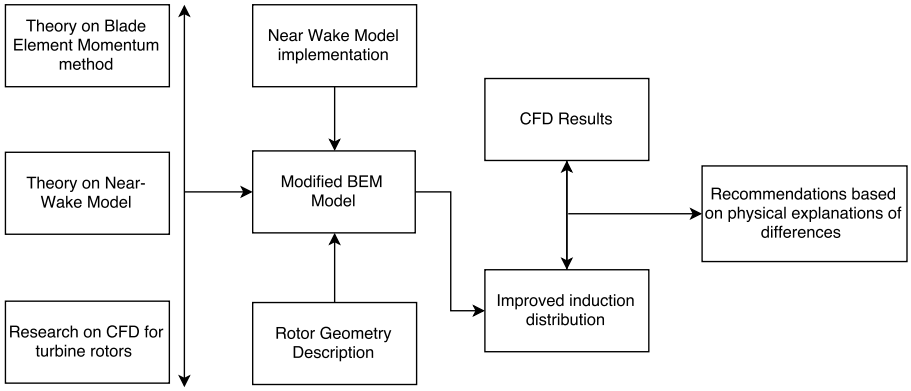

Figure 1.1: Schematic representation of research framework

1.4 Methodology

It is important to briefly mention how different components of the research framework shape the project and the methodology that is used to answer the research questions in a comprehensive and orderly manner. The first layer of the framework is related to acquiring knowledge and practical information on the methods that are being studied. A literature study has been carried out to accomplish this and the focus of this study has been on the theory of the Blade Element Momentum method and the near wake model. In addition, a small portion of the study is focused towards the methods of calculating the induction from rotor CFD simulations as this has been an interesting and debatable topic in academia and industry. In the second stage of the research framework, a near wake model is programmed that is then coupled with the blade element momentum method based on the acquired knowledge in the literature study. The model is implemented using FORTRAN and MATLAB. The model itself is programmed using FORTRAN and it is called and interfaced using MATLAB.

The rotor geometry used for the testing and analysis of the model is the DTU 10 MW reference wind turbine (RWT) [6]. The turbine is designed by Danmarks Tekniske Universitet (DTU) for research purposes. The results of the simulations for the DTU 10 MW RWT with the BEM method and near wake coupled model are compared with CFD simulations. The geometry of the blade is modified to represent the uneven loading when testing the model. The modified chord distribution of the blade models changes in the circulation distribution along the blade. This is reflected in the induction distribution and the performance of the model in estimating the induction in such uneven loading conditions is also analyzed.

1.5 Outline

The outline of the report content is briefly defined here. The introduction chapter is followed by a look at the theoretical background of the methods that are relevant to the thesis in Chapter 2 based on the literature study. Next a description of the NWM is presented in Chapter 3. The implementation of the coupled model is also described along with flowcharts in this chapter. The setup of the simulations and model operating conditions are explained in Chapter 4 with a description of the DTU 10 MW RWT and the turbine operational settings for the tests. The CFD setup is described for the comparison results from CFD simulations followed by the geometries used for the uneven loading analysis. The results from the model and the comparisons are presented in Chapter 5. The last two chapters discuss the presented results and the conclusions and findings that can be derived from the current study.

Chapter 2

Theoretical Background of Aerodynamic Models

In this chapter, an overview of the various aerodynamic models for analysis of wind turbines is presented in order to understand their advantages and limitations. It has already been discussed briefly in the introduction that the BEM method is the most widely used tool in most aeroelastic codes such as FAST, HawC2, Phatas, FOCUS, just to name a few. In terms of a comparison of the BEM with other methods such as CFD or vortex wake codes it is seen from the work of Schepers [7] that CFD and BEM are at the opposing edges of the spectra in terms of computational effort and the incorporated flow physics. Whereas, other modifications and vortex wake methods lie in between these two.

2.1 Blade Element Momentum Model

The Blade Element Momentum method is a coupling of the 1-D momentum theory with the Blade Element Theory (BET). Originally presented by Glauert [3], it can be used to calculate the steady loads on a wind turbine for varying values of wind speed, pitch angle and rotational speed. The blade element theory describes the aerodynamics of a blade section using two-dimensional aerodynamics. The momentum theory analyzes the overall momentum balance over a control volume to relate the forces acting on the rotor to the changes in velocity.

2.1.1 BEM mathematical formulation

The BEM method couples features of momentum theory and Blade Element Theory (BET) to develop a model for rotor design and analysis. The following section will deal with the mathematical formulation of the BEM and elucidate the assumptions and contributions of both theories to the final BEM model. The notations and equations presented here are taken from Hansen [8] and a more detailed description can be found therein. From the 1-D momentum theory, the rotor is treated as a permeable disc enclosed in a stream tube. The rotor disc slows the wind down from far upstream of the rotor V_o to u at the rotor plane and then further to u_1 in the wake downstream of the rotor. This change in momentum is translated into a thrust and torque force which in turn can be used to find the power generated by the rotor. This is depicted in Figure 2.1 which shows the streamtube and the velocity of the flow upstream, downstream and at the rotor plane. The thrust force can be defined in terms of the pressure drop across the rotor as shown in Equation (2.1) where A is the area of the rotor. By applying the Bernoulli equation upstream and downstream of the rotor, the pressure drop across the rotor can be expressed as shown in Equation (2.2)

$$T = \Delta p A \tag{2.1}$$

$$\Delta p = \frac{1}{2}\rho(V_0^2 - u_1^2) \tag{2.2}$$

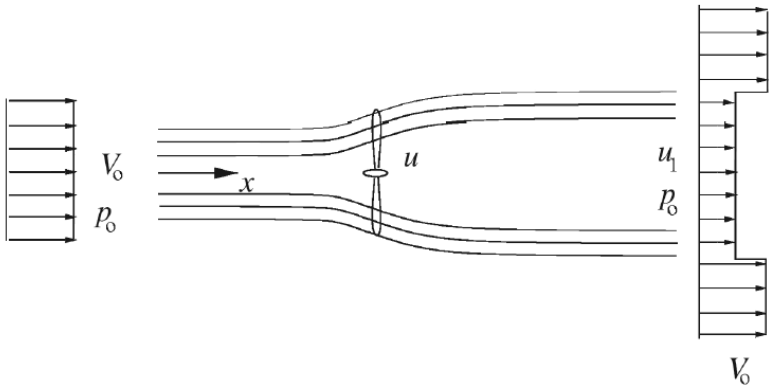

Figure 2.1: Streamtube depicting streamlines past the rotor[8]

The momentum equation and mass conservation can be applied to a control volume of cross-sectional area A_{cv} enclosing the streamtube as shown in Figure 2.2. This results in an expression of the thrust force in terms of the change in momentum across the rotor as shown in Equation (2.3) [8]

$$T = \rho u A(V_0 - u_1) = \dot{m}(V_0 - u_1) \tag{2.3}$$

From combining Equation (2.3) and Equations (2.1) and (2.2) it can be shown that the velocity at the rotor plane is the mean of the velocities far upstream and downstream of the rotor (Equation (2.4)). Note that this is not true if rotation imparted to the flow is taken into consideration [3], however this result is still useful in defining the velocities in the rotor plane and the wake. The velocity of the flow can be described in terms of the axial induction factor a, which is the factor by which the wind speed is reduced as the wind passes through the rotor.

$$u = \frac{1}{2}(V_0 + u_1) \tag{2.4}$$

$$u = (1 - a)V_0 \tag{2.5}$$

Then using Equations (2.4) and (2.5) it can be shown that the velocity in the far wake is as shown in Equation (2.6)

$$u_1 = (1 - 2a)V_0 \tag{2.6}$$

As in the case of the thrust, an expression can be obtained for the shaft power of the rotor by applying the energy equation on a control volume since frictionless flow is assumed meaning that the change in internal energy is zero through the control volume [8]. This results in:

$$P = \frac{1}{2}\rho u A(V_0^2 - u_1^2) \tag{2.7}$$

By substituting the values of u and u_1 from Equations (2.5) and (2.6) the thrust and power can be redefined in terms of the induction and incoming wind speed V_0:

$$T = 2\rho V_0^2 a(1 - a)A \tag{2.8}$$

$$P = 2\rho V_0^3 a(1 - a)^2 A \tag{2.9}$$

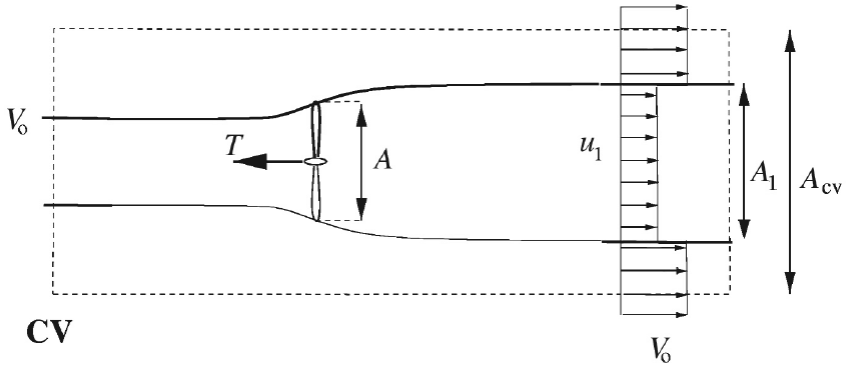

Figure 2.2: Control volume enclosing the streamtube and rotor [8]

The thrust and power of the rotor are usually expressed in terms of non-dimensional coefficients as shown in Equations (2.10) and (2.11). These coefficients can also be expressed in terms of the axial induction and wind speed by combining with Equations (2.8) and (2.9) to give Equations (2.12) and (2.13).

$$C_T = \frac{T}{\frac{1}{2}\rho V_0^2 A} \tag{2.10}$$

$$C_P = \frac{P}{\frac{1}{2}\rho V_0^3 A} \tag{2.11}$$

$$C_T = 4a(1-a) \tag{2.12}$$

$$C_P = 4a(1-a)^2 \tag{2.13}$$

The 1-D momentum theory considers the rotor as ideal, i.e. there is no rotation in the wake, however, in reality as a consequence of passing the rotor, there is a rotational velocity component a' imparted to the wind in the wake which needs to be catered for in the power calculation. This was introduced into the model through the more generalized momentum theory in Glauert's original implementation(1935). More importantly, the 1-D momentum theory does not consider the actual geometry of the rotor blades, and therefore the effect of the airfoil geometry, number of blades and twist distribution is introduced in the formulation through the blade element theory (BET). From this theory, the blade is discretized into different blade elements and 2-D aerodynamics is used to analyze the velocity triangle and lift and drag acting on the blade element. The velocities at the rotor plane are analysed for different airfoil sections along the span of the blade and these velocities are linked to the velocity obtained from the momentum theory. In this way, the Blade Element Momentum method establishes a link between both the Momentum theory and the Blade Element Theory. This corresponds to discretizing the streamtube discussed earlier in the momentum theory description into N annular elements and each annular element or strip is then considered independently with the blade element theory. A typical velocity triangle as seen for a blade element is shown in Figure 2.3

From Figure 2.3 it can be seen that there is an induced velocity w at the blade element which can be decomposed into an axial and tangential component. Note that from this figure, it can be seen that the axial velocity at the rotor plane is indeed as expressed in Equation (2.5). The rotor thrust and torque are generated as a result of the lift and drag force acting on each blade element. The lift and drag are resolved into tangential and normal forces which in turn give the differential power and thrust for each blade element. The Figure 2.4 shows the forces acting on the blade element and Equation 2.14 through 2.19 give the equations governing the angles and non-dimensional forces.

$$\tan\phi = \frac{(1-a)V_0}{(1+a')\omega r} \tag{2.14}$$

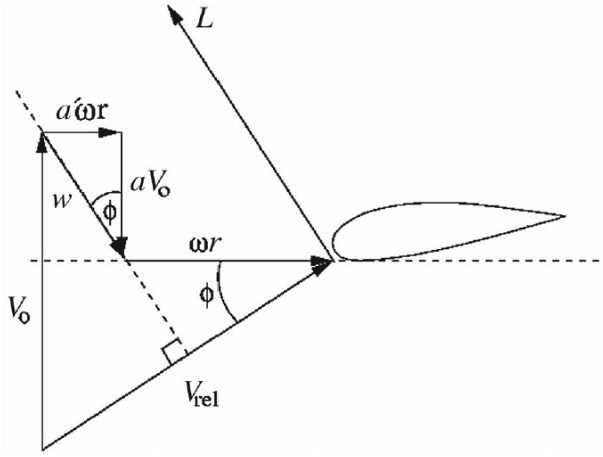

Figure 2.3: Velocity triangle showing induced velocities as seen for a 2-D blade element along a wind turbine blade [8]

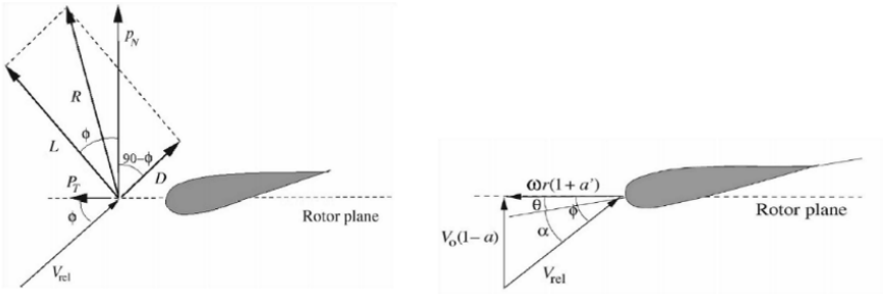

Figure 2.4: Velocity triangle showing forces on blade element(left) and velocities at rotor plane(right) [8]

$$\alpha = \phi - \theta \tag{2.15}$$

$$C_n = C_l(\alpha)\cos\phi + C_d(\alpha)\sin\phi \tag{2.16}$$

$$C_t = C_l(\alpha)\sin\phi - C_d(\alpha)\cos\phi \tag{2.17}$$

Here C_n and C_t are the normal and tangential force coefficients obtained by normalizing the normal force p_n and tangential force p_t with $\frac{1}{2}\rho A V_{rel}^2 c$. The differential contribution of each blade element or radial section to the thrust and torque of the rotor can then be expressed in terms of the normal and tangential force acting on each blade element and multiplied with the number of blades B to take into account the contribution from the whole rotor.

$$dT = Bp_n dr \tag{2.18}$$

$$dM = rBp_t dr \tag{2.19}$$

and the differential power is given as:

$$dP = \omega dM \tag{2.20}$$

Recalling that the BEM method discretizes the streamtube containing the rotor into distinct annuli each consisting of a blade element, the thrust T and torque M can be expressed in differential form for each small control volume at the rotor plane using the formulation from 1-D momentum theory (see Equation (2.3)). If the cross section area of each control volume is $2\pi r dr$ then:

$$dT = (V_0 - u_1)d\dot{m} = 2\pi r\rho u(V_0 - u_1)dr \tag{2.21}$$

The torque on the discretized annuler element is given through Euler's turbine equation

$$dM = rC_\theta d\dot{m} = 2\pi r^2 \rho u C_\theta dr \tag{2.22}$$

where C_θ is the rotational component of velocity added to the wake of the rotor and is defined as $2a'\omega$. Thus, using Equations (2.5) and (2.6), the above expressions defining dT and dM become:

$$dT = 4\pi r \rho V_0^2 a(1-a)dr \tag{2.23}$$

$$dM = 4\pi r^3 \rho V_0 \omega (1-a)a' dr \tag{2.24}$$

Comparing Equations (2.18) and (2.23) and Equations (2.19) and (2.24), the following expressions for the axial and tangential induction are obtained:

$$a = \frac{1}{\frac{4\sin^2\phi}{\sigma C_n} + 1} \tag{2.25}$$

$$a' = \frac{1}{\frac{4\sin\phi\cos\phi}{\sigma C_t} - 1} \tag{2.26}$$

$$\sigma = \frac{Bc(r)}{2\pi r} \tag{2.27}$$

where σ is the solidity of the blade and is defined as the ratio of the reference area from the blade element theory ($Bcdr$) and the reference area from the momentum theory ($2\pi r dr$). The above equations for the inductions are implicit and therefore an iterative algorithm is used to solve for the values of the induction and from the inductions, the thrust and power of the rotor can be calculated easily.

2.1.2 Limitations and corrections of the BEM method

The mathematical formulation of the BEM model in the previous section lists several assumptions that are necessary for the BEM model to be valid. These assumptions lead to inaccuracies in the solution and therefore engineering models and corrections are used to reduce the limiting effect of these assumptions in most current aeroelastic simulation tools. A brief description of some of these assumptions is listed here and they are listed in Table 2.1.

For ***heavily loaded rotors***, Equation (2.12) describing the thrust on an actuator disc becomes invalid as the momentum theory does not hold for heavily loaded cases as was evident from early experimental results of Glauert [9]. This can be seen from Equation (2.6), where for values of the axial induction $a > 0.5$, the velocity in the far wake becomes negative indicating flow reversal behind the rotor disc. This means that a large amount of kinetic energy is being converted to large scale turbulent modes. Numerical simulations with a heavily loaded disc carried out by Madsen et al. (2010) [10] also corroborate these effects and an important conclusion from this study is that the induction is not uniformly distributed over the rotor disc due to expansion and rotation in the wake even for prescribed uniform loading. Empirical corrections need to be made for high values of the induction to correct for this limitation of the momentum theory. A well-known correction is the one obtained by Glauert through experimental results [9]. The thrust equation is modified with this correction to give a new relation shown in Equation (2.28). This correction is applied in the differential thrust equations in the BEM method for each radial section (see Hansen (2015) [8]).

$$C_T = 4a(1 - \frac{1}{4}(5-3a)a), \text{ for } a > \frac{1}{3} \tag{2.28}$$

The BEM model is formulated assuming the rotor to behave as an actuator disc or having an ***infinite number of blades*** with no tip-loss effects since the flow in the rotor plane is assumed to be uniform. In reality, with a finite number of blades the flow at the rotor is not uniform and this non-uniformity is catered for by Prandtl's tip loss factor F shown in Equation (2.29), where R is the rotor diameter and r is the radial location at which the correction is applied. Schepers [7] describes the Prandlt tip loss factor as a ratio between the local axial induction at the blade as seen in the BET and the azimuthally averaged axial induction from momentum theory. Thus, it can be said that this correction is

necessary to cater for the discrepancy of actually having a finite number of blades (BET) while using the assumption of an actuator disc with infinite blades (momentum theory).

$$F = \frac{2}{\pi}\cos^{-1}\left(\exp\left(-\frac{B(R-r)}{2r\sin\phi}\right)\right) \tag{2.29}$$

The tip loss effect is an important concept and there is confusion about the tip loss factor and its effect on the flow physics. In his original implementation Glauert [3] thought of the tip loss factor as a decrease in the average induction in the wake which subsequently reduces the thrust as calculated by the momentum theory. Alternatively, from vortex theory, it can be expected to increase the local induction at the blade due to trailed vorticity from finite number of blades thereby reducing the effective angle of attack and hence loads. In either case, there is a reduction in the forces on the rotor and this reduction is modeled by multiplying the thrust and torque equations (Equations (2.23) and (2.24) with the Prandtl tip loss factor F. This results in a slightly updated form of the final expressions defining a and a' in Equations (2.25) and (2.26).

Another source of uncertainty in the method is ***airfoil data***. The calculation of the loads on the rotor is highly dependant on the lift and drag coefficients of the blade element section. These coefficients are usually obtained from 2D airfoil polars obtained from experiments carried out at specific Reynolds' numbers. However there are many 3D effects that arise due to rotation of the rotor and the airfoil data needs to be corrected for the 3D effects. An example of such effects due to rotation was identified by Himmelskamp [11], who noted a stall delay at the sections close to the root in a rotating propeller. At root sections, stall is delayed until higher angles of attack than predicted from 2D airfoil data which causes the loads to be higher. Scheper [7] attributed this to boundary layer stabilization due to centrifugal forces in a rotating rotor. Additionally, 3D geometrical effects such as taper and twist, are more important at the tip sections and 2D airfoil data is not sufficient to analyze the flow. In their review of wind turbine aerodynamics Hansen and Madsen [12], cited airfoil data as a major source of inaccuracies in BEM computations and recommended to use reliable 3D corrected airfoil data for better results.

The BEM method considers ***independence of the annular elements*** such that there is no influence of one radial/annular element to the next. Glauert [3] reported that although this assumption cannot be verified, the error associated to it is small. Wilson and Lissaman [13] modeled an annular element in the wake of a turbine by superposition of two vortex cylinders with different radii R_0 and r_0 where $R_0 > r_0$. The vortex cylinders were assumed to have the same circulation strength but opposite signs. The net effect of the circulation in such a model can only be felt in the annular element bound between R_0 and r_0 since below r_0 the two circulations cancel each other out. Thus their analysis demonstrated independence of the annular elements in case of lightly loaded rotors with an infinite number of blades. Further, Fiedel [14] did a simple analysis which showed that for finite number of blades the annuli are not independent and the induction from neighboring annular elements interacts with each other. This was done with the assumption of no wake expansion and for lightly loaded rotors. It is expected that the dependence of the annular elements is a function of both the number of blades and the effect of the wake expansion at the rotor. Madsen et al. [15] reported that the wake expansion causes a flow deceleration on the outboard parts of the blades and since the standard BEM assumes no wake expansion, it overestimates the loads on the outer parts of the blade. A correction for this was proposed in the same study by Madsen et al. [15].

Table 2.1: Limitations or Assumptions of the BEM and the corresponding theories

Limitation /Assumption	**Theory**
Light loading	Momentum Theory
Infinite number of blades	Actuator Disc / Vortex
2-D Airfoil Data	BET
Independence of Annuli	Momentum / BET
No wake expansion	Momentum / BET
Steady and Axial Inflow	Momentum / BET

The assumptions described in the preceding paragraphs are summarized in Table 2.1. In addition to the major assumptions and limitations that are highlighted, there are other limitations of the BEM, which arise because it has been developed assuming ***steady and axially aligned flow***. In practice, the incoming flow is not uniform and is altered

by effects such as wind shear, yaw misalignment and tower shadow. Unsteady effects also arise due to the time lag between a change in lift and the corresponding response of the induction in the wake. These aspects of unsteadiness and yaw misalignments are usually corrected by different models in most aeroelastic simulation tools such as HawC2, FAST, FOCUS working in the time domain. A verification study comprising common aeroelastic codes showed a typical difference of 5-10 % between measured and simulated results[16]. Research for complex flow phenomena such as yawed flow, fast variations in pitch and rotor speed, flow close to root and tip and wake effects indicates that the standard BEM does not accurately model the loads in such conditions and higher fidelity models need to be used such as CFD or vortex wake codes [12].

2.2 Computational Fluid Dynamics

The most advanced aerodynamic models in terms of modeled flow physics use Computational Fluid Dynamics to solve the Navier-Stokes equations numerically and obtain the loads and the behavior of the flow field. Different techniques are utilized to model turbulence or rotor geometry in CFD computations. For a history of development in CFD for wind energy applications, see [17]. In wind energy, the most widely used CFD codes are Reynolds Averaged Navier Stokes (RANS) models or Large Eddy Simulation (LES) methods as stated by Sanderse et al. [18] which solve the well-known Navier-Stokes equations. The Navier-Stokes equations[19] are as shown in Equation (2.30)

$$\rho\left(\frac{\partial u_i}{\partial t}+u_j\frac{\partial u_i}{\partial x_j}\right)=\rho g_i+\frac{\partial}{\partial x_j}\left(-p\delta_{ij}+\mu\left(\frac{\partial u_i}{\partial x_j}+\frac{\partial u_j}{\partial x_i}\right)\right) \tag{2.30}$$

here the Navier-Stokes equation is given in indicial notation and t is the time, g_i is the volume force and x_i is the Cartesian coordinates. The pressure is defined as p, viscosity is μ and the Kronecker delta is defined as:

$$\delta_{ij}=\begin{cases}1, & \text{for i=j}\\ 0, & \text{for i}\neq\text{j}\end{cases}$$

The RANS models mentioned previously use the Navier-Stokes equations after averaging over time and then based on Reynolds decomposition, split into mean and fluctuating parts for all the flow variables. The resulting equation is titled the Reynolds equation and there is an additional term in the form of Reynolds stresses given as $-\rho\overline{u_i^{'}u_j^{'}}$. The Reynolds stresses are a feature of turbulent flows and comprise of six components [20]. Now, for turbulent flows, it is seen that the system is not closed i.e. there are more unknowns (three velocity components, pressure p, six Reynolds stresses) than equations (three Reynolds equations and continuity equation). This means that additional equations need to be used for solving the system. These equations stem from different turbulence closure models which model the turbulent terms. For detailed mathematical descriptions the reader is referred to [20].

Most turbulence models employ the Boussinesq eddy-viscosity assumption [21] which expresses the Reynolds stresses as the product of the strain rate $\frac{d\overline{u}}{dy}$ and the turbulence viscosity μ_t, which is again estimated using various models. These can be in the form of simple algebraic models or turbulence-energy equation models. The algebraic models simply express the turbulence viscosity in terms of a "mixing length". The turbulence-energy equations on the other hand employ the turbulent kinetic energy, $k=\frac{1}{2}(\overline{u_i^{'}u_i^{'}})$ to calculate the turbulent viscosity μ_t and they are distinguished based on the number of equations employed.

Sanderse et al. [18] states that the $k-\epsilon$ model is used mostly for wake simulations and the $k-\omega$ model with shear stress transport ($k-\omega$ SST) in the region close to the blade. The $k-\omega$ SST model can also model lightly separated flows on airfoils which proves to be problematic for the $k-\epsilon$ model as noted in [22]. The Large Eddy Simulation (LES) model computes the large scale eddies in the fluid and models the small scale motion by modeling the smaller eddies using equations describing the subgrid-scale stresses. The LES models are computationally more expensive than the RANS models however they are still faster than Direct Numerical Simulation (DNS) methods which solve the Navier-Stokes equations directly and there is no closure problem. Naturally this makes the DNS methods very computationally expensive and therefore even with state-of-the-art computers such simulations are too time taking to be practically implemented for complex systems such as wind turbines. The rotor can be represented by various methods while performing CFD calculations and varying degrees of detail are modeled through the different methods.

Generalized Actuator Disc implementations simplify the influence of the rotor by representing the rotor in terms of an applied force acting as a momentum sink. This is done to make the simulations computationally efficient however including the actual geometry of the rotor can give much more insight into the flow physics at the blade. In case the detailed rotor geometry is modeled, the mesh needs to be adapted near the blades to better capture the flow effects. Especially near the root and tip region of the blade the mesh has to be generated with care. This is in order to better resolve the vortices generated at the root and tip of the turbine. In most wind energy applications, structured grids are used in mesh generation with occasional usage of hybrid meshes using unstructured grids away from the blade [17].

Lastly it is important to mention and highlight that there are multiple solvers, convection schemes, turbulence modeling settings, mesh types and configurations which increase the options available for the kind of simulations possible. This also means that a certain level of expertise is required to set up the ideal settings to model the case under investigation as realistically as possible. Of course this is not always achievable even if the most advanced computing setup is available due to the numerical limitations of the methods at our disposal. In addition there are also numerical dissipation issues related to CFD. While CFD calculations can resolve the turbulence and give accurate load distributions with the highest level of detail, they are far too time consuming for practical implementation to simulate the hundreds of load cases required for aeroelastic analysis of a wind turbine. Therefore, other methods need to be researched and implemented as a compromise between the speed of BEM and the accuracy and detail of CFD.

2.3 Introduction to fluid dynamics concepts and Biot-Savart law

Most lifting line models and panel methods use the Biot-Savart law which calculates the induction at a point due to vorticity in a fluid. A short introduction to the Biot-Savart law is essential to understand the framework of the Near wake model which is in essence a lifting line model. This section aims to introduce the fluid properties and the theory behind the law, but for a deeper understanding of how potential flow theory describes fluid flow around airfoils and a better mathematical description of vorticity and induction due to vorticity the reader is guided to aerodynamics books by Katz and Plotkin [23] or Anderson [24]. The Biot-Savart law which primarily relates the magnetic field due to an electric current is applied to aerodynamics in a similar manner. With this law the induction caused due to the vorticity of a free vortex in a fluid flow can be calculated.

The generation of lift from a wind turbine blade is directly tied to the vorticity in the wake caused by shed and trailed vortices. The vorticity $\vec{\zeta}$ in a fluid defines the tendency of fluid particles to rotate and is a vector quantity that describes the rotary motion or path of a particle at a point in a fluid. For the case of *free vortices*, the vorticity is zero at any point other than the axis of the vortex, and the velocity of the fluid particles is inversely proportional to the distance from the core of the vortex. Since the vorticity is a measure of the rotation of a fluid element it is defined as twice the angular velocity $\vec{\omega}$ of that element, and is also given by the curl of the velocity field $\vec{v}$ representing the fluid elements in the fluid flow [23].

$$\vec{\zeta} \equiv 2\vec{\omega} = \nabla \times \vec{v} \tag{2.31}$$

The circulation Γ, which is defined as the line integral of the velocity field along a closed curve C, is then related to the surface integral of the vorticity by employing Stoke's theorem on a surface S bounded by the curve C where the normal vector to the surface is $\vec{n}$.

$$\Gamma \equiv \oint_C \vec{v}.d\vec{l} = \int_S \nabla \times \vec{v} \cdot \vec{n} dS = \int_S \vec{\zeta} \cdot \vec{n} dS \tag{2.32}$$

The circulation Γ is tied to the lift generated by an airfoil or wing placed in incoming flow V_∞ by the Kutta-Joukowski theorem which gives that:

$$L = \rho_\infty V_\infty \Gamma \tag{2.33}$$

Therefore, if there is some vorticity in a fluid flow, it leads to a circulation Γ, which in turn gives rise to a lift force. Vorticity is introduced in flows through vortice elements such as vortex lines and vortex tubes. As explained in the

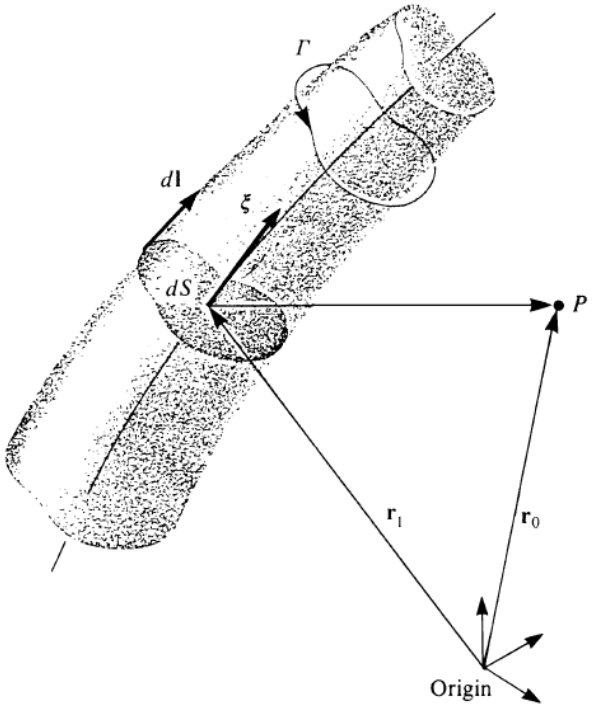

Figure 2.5: Induction at a point P due to a vortex element [23]

preceding text, the presence of a vortex effects the velocity field around it and the velocity induced at a particle or a point in space due to the vortex is inversely proportional to the distance from the vortex element. The Biot-Savart law gives the induced velocity at a point P in space due to a vortex element with strength $\vec{\zeta}$ and direction $d\vec{l}$ as:

$$\vec{u}_{ind} = \frac{\Gamma}{4\pi} \int \frac{d\vec{l} \times (\vec{r}_0 - \vec{r}_1)}{|\vec{r}_0 - \vec{r}_1|^3} \tag{2.34}$$

where Γ is the circulation, given by the area integral over the surface S bounded by a curve enclosing the vortex element as shown in Figure 2.5 and $\vec{r}_0$ and $\vec{r}_1$ give the position of the point P and vortex element in space.

Most lifting line and panel method models utilize the Biot-Savart law in some form or the other. Such models replace a three dimensional lifting surface such as a wing or a blade by a volume,surface or line consisting of vortex elements having some spanwise circulation distribution $\Gamma(y)$ which can be used to predict the lift generated by the lifting surface. The line of vortex elements representing the blade cannot end in space according to Helmholtz theorems which has the following three postulates [23]:

- The strength of a vortex filament remains constant along its length
- A vortex filament cannot end in a fluid; it must extend to the boundaries of the fluid or form a closed path
- In the absence of rotational external forces, a fluid that is initally irrotational remains irrotational

Through these theorems it is established that a vortex filament must start and end at a solid boundary or form a closed loop in a fluid. Thus, the flow field around a lifting surface is represented by a vortice system comprising of vortices trailed at the tips of the lifting surface and the vorticity shed from the trailing edge of the lifting surface forming a closed ring or loop of vortices.

2.4 Numerical Vortex Codes

As explained in the beginning of this chapter vortex wake codes lie in between the spectra of aerodynamic models defined by CFD and basic models such as the BEM model. Therefore a brief and small commentary is presented here to conclude the theoretical background chapter. Using the Helmholtz theorems introduced in the previous section at their core, numerical vortex codes employ vortex theory to construct the velocity flowfield around a body. The simplest form of a vortex code is a lifting line model. An aerodynamic body is replaced with a lifting line consisting of vortice elements. The induced velocity at the lifting surface due to these vortices can be estimated by the Biot-savart law and then using the relative velocity at the airfoil section, the lift can be calculated from the velocity profile at the airfoil section. Lifting line models are preferred as they calculate the lift at a section of a lifting surface in a way that takes into account the neighboring sections as well which is very important in the case of 3D lifting surfaces which have spanwise effects that cannot be ignored. Katz & Plotkin [23] explain the lifting line model by replacing a lifting body with a vortex line along its quarter chord as shown in Figure 2.6. The wake in this formulation comprises of horseshoe vortices of constant strength made of vortex lines having equal magnitude and opposite sign based on the circulation strength at that section of the lifting body.

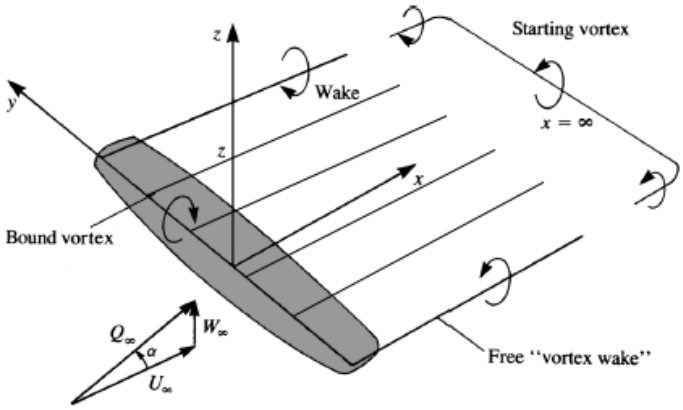

Figure 2.6: Horseshoe vortex system representing vortex line [23]

Most lifting line models assume that the lifting line has to be straight thus demanding some modifications in order to account for swept wings or blades with planar deflections in the lifting surface. A convenient feature of the lifting line models however is that they are valid for slender blades which is the norm for most modern wind turbine blades. Phillips et al. [25] resolved the straight lifting line requirement by accounting for influence of the bound vortex elements which from the original theory by Prandtl would cancel each others effect out. In addition Phillips et al. also suggested that the wake in such models be aligned with the free stream to conserve the correct boundary conditions.

Other vortex codes shown by Katz & Plotkin [23] model the lifting surface in more detail such as a surface or a volume by representing the planform and camber of the lifting surface in terms of vortice elements or vortice lattice elements. This results in more accuracy at the cost of complexity and computation time.

It should be mentioned here that wakes created by rotors are more complex than the wakes of wings and therefore greater detail is required for the wakes of rotors. Two most common methods based on this distinction of wakes are the free wake vortex codes and frozen wake or prescribed wake vortex codes. Free wake vortex codes model the change in the wake itself caused due to the induction from the vortices in the wake. Thus the wake is "free" to evolve its geometry. This means that the flow field is more physically described with free vortex codes. This also means that the complexity and number of calculations scale proportionally since the induction has to be calculated at each vortex element in the wake in addition to the lifting body or line.

In contrast to the free wake vortex codes, frozen wake codes use a prescribed geometry of the wake where the locations of the vortice elements in the wake is already known through experiments or modeled based on the convection speed of the incoming flow or similar parameters. Since the wake is considered to be frozen, the vorticity

from the vortice elements does not affect the other vortice elements and thus the induction only needs to be calculated at the lifting line. Thus frozen wake models are much faster than the free wake models [26].

Another interesting type of vortex codes represent the wake by means of vorticity blobs or parcels containing vorticity. These type of codes represent the large wake structures in a more detailed way thus they can be considered a special form of Computational Fluid Dynamics. Their formulation is based on the theory by Winckelmans et al. [27]. Since these methods give a better description of the larger wake they are very suitable for analysis of wind turbines in farms however they offer a lower level of detail near the turbine blades themselves since the models are still based on lifting line assumptions.

Chapter 3

Near Wake Model Description

In this chapter, an in depth look at the methodology of the Near Wake Model is presented. A description of the original model is given after a general introduction, followed by the corrections that have been added with further developments to add more physical credence to the model. The equations and framework of coupling the model to the BEM method is presented next alongside an algorithm explaining the logical flow of the computations in the current implementation.

From the limitations of the BEM theory highlighted in the previous chapter, the inaccuracies arising due to the infinite number of blades assumption (actuator disc theory) and the independence of the annuli assumption (momentum theory) are expected to be addressed due to the near wake effects from the NWM.

3.1 Near Wake Model

The near wake model (NWM) is a prescribed lifting line model based on a model proposed by Beddoes in 1987 [28]. This model essentially utilizes the lifting line methods explained in the previous section which calculate the local lift force on each section based on the induction due to the vortices in the flow field. For a more detailed discussion on lifting line theory and vortex codes, the reader is directed to Katz and Plotkin [23]. The near wake model computes the steady and unsteady induction from the trailed vorticity behind the rotor blades. The model takes into account the vorticity trailed during one quarter revolution of the rotor only, assuming that the effect of the trailed vortex is diminished significantly after a quarter revolution. Since a BEM model is based on an actuator disc assumption, it does not model detailed induction effects at the individual blades which is compensated for by the NWM.

The near wake model calculates the induction from the near wake of the rotor only, however, to get a complete picture of the induction, the effect of the far wake is also needed and this is accomplished by coupling the NWM with the BEM method. When coupled with BEM as done in [4] the near wake model is seen to improve the results from BEM by adding near wake trailed vorticity [29]. It is important to note that the far wake effects and slower dynamic inflow effects which are not due to the trailed vorticity in the vicinity of the blades are taken care of with the induction from the BEM model. Thus the BEM method contributes the effect of the far wake to the coupled model, giving a complete representation of the induction from the rotor. The benefit of the NWM in terms of added flow physics to the implementation is that it accounts for both the root and tip vortices, adds aerodynamic coupling between the different annuli along the blade span as well as modeling the near wake induction dynamics.

The near wake model has a basic assumption stating that the induction due to the trailed vorticity reaches zero within a quarter revolution. To make the computation of the induction more efficient, the trailed vorticity is assumed to follow prescribed arcs in the rotor plane. The axial induction is usually found by numerically solving a modified form of the Biot-Savart law (Equation (2.34)), however this numerical integration is a time taking process.

Beddoes [28] suggested a fast algorithm to speed up the numerical integrations to solve the Biot-Savart law. The induction is computed from a vortex element at the lifting line and this value is decreased as the vortex element is shed into the wake and moves away from the blade. The induction at the lifting line dw_0 can be used to non-dimensionalize the induction from a vortex element dw at a location behind the blade after being trailed by a distance defined by the

angle β. A spatial decay function is setup to define this non-dimensional induction, which decays from 1 to a very small value for increasing β i.e. distance from the blade. This spatial decay of the induction is efficiently represented by exponential indicial functions based purely on geometrical factors. The geometrical factor depends on the arc radius r and the distance h from which the vortex is trailed. The utility of these indicial functions is that they are fast to calculate thus greatly decreasing the computation time as compared to standard free vortex wake codes [23]. Beddoes' trailing wake algorithm determines the induction W at a given blade location as a sum of a slowly decaying component and fast decaying component of the induction. This slow and fast component contribution from all shed vortices is summed to get the induction at every point along the blade. The contribution to the induction W from previous time steps is added to the induction from the most recent trailed vortex for each time step. This estimated induction W calculated at different radial locations on the blade behaves as the induced velocity aV_0 from the BEM method.

The NWM originally considers the trailed vorticity to stay in the rotor plane which is a good assumption for high tip speed ratio operation. However, above rated wind speed the trailed vorticity is convected downwind much faster and therefore a helical path is more appropriate to model the vorticity as was depicted by Wang et al. [30], however they did not incorporate the decrease in induction due to larger distance between the blade and the trailed vortex due to a larger helix angle; this was corrected by Pirrung et al. [5]. Close to the blade root, especially in cases when the trailing point is farther outboard than the calculation point it is seen that the indicial function decay becomes slower. This means that the effect on the induction does not reach zero within a quarter revolution even for high convection speeds. This leads to an overestimation of the induction from the NWM and this was resolved in the form of a root correction by Pirrung et al. [5]. It must also be noted that when introducing a coupling between the BEM and the NWM, the induction from the BEM has to be reduced so as to ensure that the induction from the NWM is not modeled redundantly and this is done using a coupling factor which was presented by Andersen [31] and an alternative was suggested by Pirrung et al [5]. A more in depth description of these corrections and their formulations existing in literature is presented after the framework of the model in Section 3.3. In this study, the NWM is coupled with a BEM code to study the steady state behavior of a rotor and analyze the performance of this modified aerodynamic model for non-uniform loading and comparing with CFD results. As such the original dynamic NWM is modified for steady state implementation in this work and special attention is needed to ensure stability of the solution for such an application since this has not been explicitly done before.

3.2 Model framework

With the background presented in the preceding section, the framework and goal of the near-wake model can be elucidated in a better manner. Suppose that there is a wind turbine blade which rotates and as it does so, it leaves a trail of vortices behind it at different radial positions along the blade. If it is desired to calculate the induction from these trailed vortices at different points along the blade the Biot-savart law (Equation (2.34)) can be used directly. Based on Figure 3.1, the vortex is trailed at a distance r from the blade root and the calculation point is located at distance h from the trailing location [5]. The angle β defines the position of the vortex filament after it has been trailed behind the rotating blade. Now, the Biot-Savart law uses vector quantities defining the distance between the vortex element and calculation point as well as the vector defining the vortex element. If $\vec{x}$ points from the vortex filament location to the point of calculation and $\vec{ds}$ is the vector definition of the vortex which points in a direction away from the blade. Then the vector quantities needed for the Biot-Savart law can be given as:

$$\vec{x} = (-r\cos\beta + r - h)\hat{i} + r\sin\beta\hat{j} \tag{3.1}$$

$$\vec{ds} = -ds\cdot\sin\beta\hat{i} - ds\cdot\cos\beta ds\hat{j} \tag{3.2}$$

where the x-axis is positive from blade root to tip, y-axis is positive in front of the blade in the rotor plane [5]. The induction $\vec{dw}$ at the calculation point h on the blade section can then be estimated from the Biot-Savart law as:

$$\vec{dw} = \frac{\Delta\Gamma}{4\pi}\frac{\vec{x}\times\vec{ds}}{|\vec{x}|^3} \tag{3.3}$$

The axial induction can then be calculated as the upwind component of the vector $\vec{dw}$

$$dw = \frac{\Delta\Gamma}{4\pi} \frac{x_{\hat{i}} ds_{\hat{j}} - x_{\hat{j}} ds_{\hat{i}}}{|\vec{x}|^3} \tag{3.4}$$

Using the values specified in Equation (3.2) this can be expressed as:

$$dw = \frac{\Delta\Gamma}{4\pi} \frac{(-r\cos\beta + r - h)(-\cos\beta \cdot ds) - (r\sin\beta)(-\sin\beta \cdot ds)}{(\sqrt{(-r\cos\beta + r - h)^2 + (r\sin\beta)^2})^3} \tag{3.5}$$

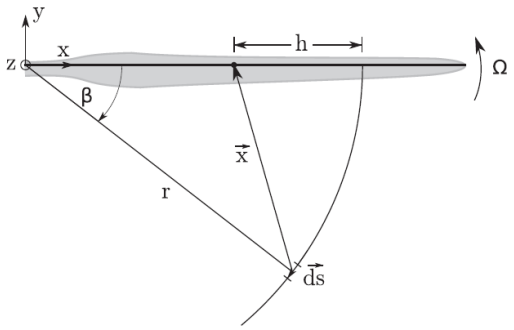

Figure 3.1: Blade geometry description where blade rotates with angular velocity Ω as the vortex is trailed behind it in a circular arc with angular displacement β [5]

$$dw = \frac{\Delta\Gamma}{4\pi} \frac{r\cos^2\beta ds - r\cos\beta ds + h\cos\beta ds + r\sin^2\beta ds}{(\sqrt{r^2\cos^2\beta + r^2 + h^2 - 2r^2\cos\beta - 2rh + 2rh\cos\beta + r^2\sin^2\beta})^3} \tag{3.6}$$

and using the trigonometric identity $\sin^2\beta + \cos^2\beta = 1$

$$dw = \frac{\Delta\Gamma}{4\pi} \frac{rds\left(1 - \left(1 - \frac{h}{r}\right)\cos\beta\right)}{\left(r\sqrt{1 + \left(1 - \frac{h}{r}\right)^2 - 2\left(1 - \frac{h}{r}\right)\cos\beta}\right)^3} \tag{3.7}$$

which results in Equation (3.8) giving the axial induction dw_{ax} at the lifting line as shown:

$$dw = \frac{\Delta\Gamma ds}{4\pi r^2} \frac{1 - \left(1 - \frac{h}{r}\right)\cos(\beta)}{\left[1 + \left(1 - \frac{h}{r}\right)^2 - 2\left(1 - \frac{h}{r}\right)\cos(\beta)\right]^{3/2}} \tag{3.8}$$

In the above equation, ds denotes the length of the vortex element along a circular arc with vortex strength of $\Delta\Gamma$ which is the change in circulation from one section to another.

Now, the induction can be calculated by numerically integrating the expression presented above directly however this is a computationally expensive task if the induction at each calculation point is then calculated for all the trailed vortices in the wake of the blade. As mentioned before, this integral can be redefined by calculating the induction from all the vortex filaments in the wake at the lifting line and then decaying this value gradually. To calculate the induction of the vortex elements at the lifting line, the arc angle β is zero in the expression above and the induction value at the lifting line dw_0 is calculated.

$$dw_0 = dw(\beta = 0) = \frac{\Delta\Gamma ds}{4\pi r^2} \frac{1 - \left(1 - \frac{h}{r}\right)}{\left[1 + \left(1 - \frac{h}{r}\right)^2 - 2\left(1 - \frac{h}{r}\right)\right]^{\frac{3}{2}}} = \frac{\Delta\Gamma r d\beta}{4\pi h|h|} \tag{3.9}$$

From vortex theory it is known that the induction from a free vortex decreases with increasing distance from the vortex. Based on this, if the induction from the vortex elements at the lifting line is calculated, then it follows that the induction value decreases as the vortex elements trail away from the lifting line. If the induction dw from an element at position β behind the blade is then non-dimensionalized with the value of induction at the lifting line dw_0 then the result is a function whose value starts at 1 and decays to 0 for increasing values of β.

$$\frac{dw}{dw_0} = \frac{\left(\frac{h}{r}\right)^2 \left[1 - \left(1 - \frac{h}{r}\right)\cos(\beta)\right]}{\left(1 + \left(1 - \frac{h}{r}\right)^2 - 2\left(1 - \frac{h}{r}\right)\cos(\beta)\right)^{\frac{3}{2}}} \tag{3.10}$$

The decay function shown in Equation (3.10) was approximated by Beddoes as a sum of exponential functions with a fast and slow decaying component. The Equation (3.11) shows the exponential function used to express the non-dimensional induction as a function of the vortex position on the circular arc β, and a geometric parameter Φ. Where Φ is based on the ratio of the distance h between the calculation point and vortex trailing point, and the distance from the origin to the vortex trailing point r.

$$\frac{dw}{dw_0} \approx 1.359e^{-\frac{\beta}{\Phi}} - 0.359e^{-\frac{4\beta}{\Phi}} \tag{3.11}$$

The expression for Φ is given by Madsen et al. [4] and expressed as:

$$\Phi = \left(\frac{\pi}{4}\right)\left|\left(1 + \frac{h}{2r}\right) ln\left(1 - \frac{h}{r}\right)\right| \tag{3.12}$$

With the induction defined as a sum of two exponential functions, the effect of the induction from all trailed vortices on the arc can be calculated by computing the integrated downwash. Numerically, this can be shown for a single time step i as:

$$W_i = X_i + Y_i \tag{3.13}$$

and X_i and Y_i are the slow and fast decaying components of the exponential function described above and are further dependent on the decayed induction obtained from the previous time steps as well as the induction from the vortex element trailed in the current time step [5]:

$$X_i = X_{i-1}e^{-\Delta\beta/\Phi} + 1.359D_w e^{-\Delta\beta/2\Phi} \tag{3.14a}$$

$$Y_i = Y_{i-1}e^{-4\Delta\beta/\Phi} - 0.359D_w e^{-2\Delta\beta/\Phi} \tag{3.14b}$$

Here $\Delta\beta$ is the movement of the vortex defined by Beddoes [28] as $\Omega\Delta t$. D_w is the induction from the newest trailed vortex element [5] and is given by using the Biot-Savart law assuming that the new element is straight and perpendicular to the lifting line. As seen in Equations (3.14a) and (3.14b), D_w is split into a fast and slow decaying part which is calculated at half time steps. The accumulated induction from the previous time steps is then added to these components.

$$D_w = \frac{\Delta\Gamma\left(\frac{\Delta s}{|h|}\right)}{4\pi h\left[1 + \left(\frac{\Delta s}{h}\right)^2\right]^{1/2}} \tag{3.15}$$

3.3 Model modifications

Since its conception by Beddoes [28] and implementation for wind turbine rotors by Madsen [4], modifications have been done to reduce errors related to the assumptions in the NWM. This section deals with the proposed modifications and how the governing equations are affected by them.

3.3.1 Correction for negative h/r values

As explained in the previous section Φ is a geometric parameter which depends on h and r. Using the original definition of Φ lead to an error in case of negative values of h/r i.e. when the vortex is trailed inboard as compared to the calculation point. Wang et al. [30] suggested a correction for such cases redefining the parameter Φ as:

$$\Phi = \frac{ln\left(1-\frac{h}{r}\right)}{1.5+ln\left(1-\frac{h}{2r}\right)} \qquad \text{if } h/r < 0 \tag{3.16a}$$

$$\Phi = \left(\frac{\pi}{4}\right)\left|\left(1+\frac{h}{2r}\right)ln\left(1-\frac{h}{r}\right)\right| \qquad \text{if } 0 < h/r < 1 \tag{3.16b}$$

This definition of Φ is the one that is used in the current implementation. Further modifications are done to Φ for incorporating other effects and their basis will be presented in the subsequent sections.

3.3.2 Convection Correction

The original model considers the vortices trailed by the blade to follow circular arcs, however in reality these vortices are convected downstream with the incoming wind speed and therefore follow helical arcs behind the blade. Especially for higher wind speeds, the vortices tend to be convected at a higher helix angle and therefore the assumption of circular arcs no longer remains valid.

Convection of Vortices resulting in Helical Vortice Arcs

There have been modifications to include the helix angle in the model, Wang et al. [30] suggested a modification to the geometrical parameter Φ with the helix angle included. However this did not account for the decrease in the induction when the vortices are convected away from the blade. A modification suggested by Pirrung et al. [5] takes this into account by modifying the Equation (3.10) to include downwind convection of the arcs. The new expression adds the effect of the increased distance between blade and vortice elements using the helix angle φ of the arc followed by the trailed vortices. This is accomplished by modifying the vector quantities introduced in Equations (3.1) and (3.2).

$$\vec{x} = (-r\cos\beta + r - h)\hat{i} + r\sin\beta\,\hat{j} + r\beta\tan\varphi\,\hat{k}$$

$$\vec{ds} = \frac{ds}{\sqrt{1+\tan^2\varphi}}(-\sin\beta\,\hat{i} - \cos\beta\,\hat{j} - \tan\varphi\,\hat{k})$$

The modified expression for the axial induction is shown in Equation (3.17) obtained from the same method followed to obtain Equation (3.8). A corresponding expression for tangential induction is presented in Equation (3.18) obtained by considering the y-component of the product $\vec{x}\times\vec{ds}$ while solving the Biot-Savart law Equation (3.3).

$$\frac{dw_{ax}}{dw_{0,ax}} = \frac{\left(\frac{h}{r}\right)^2\left[1-\left(1-\frac{h}{r}\right)\cos(\beta)\right]}{\left(1+\left(1-\frac{h}{r}\right)^2-2\left(1-\frac{h}{r}\right)\cos(\beta)+\left(\beta\tan\varphi\right)^2\right)^{\frac{3}{2}}} \tag{3.17}$$

The term $\beta \tan\varphi$ is the additional term in Equation (3.17) when compared to Equation (3.10) and is the result of incorporating the increased distance between vortex and calculation point due to convection.

$$\frac{dw_{tan}}{dw_{0,tan}} = \frac{\left(\frac{h}{r}\right)^2 \left[1 - \frac{h}{r} - \cos(\beta) - \beta\sin(\beta)\right]}{\left(1 + \left(1 - \frac{h}{r}\right)^2 - 2\left(1 - \frac{h}{r}\right)\cos(\beta) + \left(\beta\tan\varphi\right)^2\right)^{\frac{3}{2}}} \tag{3.18}$$

Having modified the decay function of the induction, the correction for downwind convection is then derived by equating Equations (3.11) and (3.17) and integrating both sides over $d\beta$. The value of Φ which satisfies both sides of the equation can be found numerically as the optimal $\Phi_{opt,conv}$ with downwind convection. Similarly, an optimal value $\Phi_{opt,noconv}$ without convection can be obtained by integrating and equating the original equations, Equation (3.10) and Equation (3.11). The ratio of these optimal parameters defines the correction f giving the modified parameter Φ^* as:

$$\Phi^* = \Phi \frac{\Phi_{opt,\text{conv}}}{\Phi_{opt,\text{no conv}}} \approx \Phi f \tag{3.19}$$

where f is a function of both h/r and the tangent of the helix angle $\tan\varphi$. Since f depends on the helix angle it must be calculated during each iteration of the model. Through curve fitting, it is estimated to be represented by the expression given in Equation (3.20)

$$f = 1.1e^{-b_1\tan\varphi} + a_1 e^{-b_2\tan\varphi} - 0.1 - a_1 \tag{3.20}$$

where b_1,b_2 and a_1 are functions of h/r approximated by exponential functions

$$b_1 = a_{1,1} + a_{1,2}e^{a_{1,3}h/r} + a_{1,4}e^{a_{1,5}h/r} \tag{3.21}$$

$$b_2 = a_{2,1} + a_{2,2}e^{a_{2,3}h/r} + a_{2,4}e^{a_{2,5}h/r} \tag{3.22}$$

$$a_1 = a_{3,1} + a_{3,2}e^{a_{3,3}h/r} + a_{3,4}e^{a_{3,5}h/r} \tag{3.23}$$

The coefficients which define b_1,b_2 and a_1 are obtained through curve fitting and are listed here as the elements of the matrix A, given for positive and negative values of h/r as:

$$A = \begin{bmatrix} 0.0748 & 0.3217 & 0.2720 & 0.2596 & 2.5328 \\ 0.2464 & 1.3197 & 2.5445 & 1.2137 & 0.3018 \\ 1.1736 & 0.0529 & 1.4179 & -1.5000 & -0.0018 \end{bmatrix} \quad \text{if } h/r < 0 \tag{3.24a}$$

$$A = \begin{bmatrix} 1.9223 & -1.2524 & -0.8313 & 0.0055 & 6.1569 \\ 14.0826 & -11.0331 & -0.3656 & 0.0034 & 8.8199 \\ -0.2441 & -0.0639 & 2.8980 & 0.0441 & 3.3352 \end{bmatrix} \quad \text{if } 0 < h/r < 1 \tag{3.24b}$$

The same approach can be used to calculate a modified Φ^*_{tan} for the tangential induction however the added accuracy is not worth the computation time increase especially since an accurate tangential induction is not that important as compared to the axial induction.

Convection of vortices in standstill or high wind speeds

In a more recent publication, Pirrung et al. [32] extended the model for standstill operation of a rotor to analyze aeroelastic behavior of rotors in standstill conditions. This means that the model can not only handle circular or helical arcs but also straight vortex lines trailed at different points along the blade due to standstill operation. For standstill cases or for very high wind convection speeds, the vortices would be trailed in straight lines or at very high helix angles i.e. close to straight lines. This means that the original definition of the angle β needs to be redefined as shown in Equation (3.25). It can be seen that if the vorticity remains in the rotor plane meaning there is no convection then the old and new definition of β give the same result.

$$\beta^* = \frac{V_{rel}\Delta t}{r} \tag{3.25}$$

The modification in this case is again applied to Φ in the sense that a linear interpolation is applied between the $\Phi_{straight}$ for straight trailed vortices and Φ_{circ} for the circular arcs given in Equation (3.16). The resulting corrected Φ^* is shown in Equation (3.26).

$$\Phi^* = k_\Phi \Phi_{straight} + (1 - k_\Phi)\Phi_{circ} \tag{3.26}$$

where $\Phi_{straight}$ is defined by:

$$\Phi_{straight} = -0.788\frac{h}{r} \qquad \text{if } h/r < 0 \tag{3.27a}$$

$$\Phi_{straight} = 0.788\frac{h}{r} \qquad \text{if } 0 < h/r < 1 \tag{3.27b}$$

The interpolation factor k_Φ is dependent on the helix angle φ and the h/r ratio. It is defined separately for positive and negative values of h/r as shown in Equation (3.28) which is obtained through curve fitting.

$$k_\Phi = a_{hr,1} + a_{hr,2}e^{a_{hr,3}(\frac{\pi}{2}-\varphi)} + a_{hr,4}e^{-8(\frac{\pi}{2}-\varphi)} - a_{hr,2} - a_{hr,4} \qquad \text{if } h/r < 0 \tag{3.28a}$$

$$k_\Phi = a_{hr,1} + a_{hr,2}\varphi + a_{hr,3}\varphi^2 + a_{hr,4}\varphi^3 \qquad \text{if } 0 < h/r < 1 \tag{3.28b}$$

where the $a_{hr,i}$ are also characterized through curve fitting as functions of h/r with different expressions for positive and negative h/r values

$$a_{hr,i} = n_{i,1} + n_{i,2}e^{n_{i,3}(\frac{h}{r})} + n_{i,4}e^{n_{i,5}(\frac{h}{r})} - n_{i,2} - n_{i,4} \qquad \text{if } h/r < 0 \tag{3.29a}$$

$$a_{hr,i} = p_{i,1} + p_{i,2}\left(\frac{h}{r}\right) + p_{i,3}\left(\frac{h}{r}\right)^2 + p_{i,4}\left(\frac{h}{r}\right)^3 \qquad \text{if } 0 < h/r < 1 \tag{3.29b}$$

Finally, the matrices **N** and **P** define the values of $n_{i,j}$ and $p_{i,j}$ and they simply state the coefficients obtained from curve fitting the equations to the integral solutions

$$\mathbf{N} = \begin{bmatrix} 1.01933 & -0.13567 & 0.39552 & 0.08018 & 44.83475 \\ 12.98745 & 50.0 & 0.00235 & 11.31161 & 3935.34323 \\ -0.69016 & 101.23878 & -0.00154 & 3.99520 & 0.39454 \\ -0.26925 & 50.0 & -0.00248 & 0.40364 & 1.16610 \end{bmatrix} \tag{3.30}$$

$$\mathbf{P} = \begin{bmatrix} -1.64637 & 8.14821 & -12.17849 & 5.02653 & 21.77131 \\ -0.49901 & 6.08465 & -15.17120 & 14.82541 & -2.42319 \\ 3.90836 & -18.76623 & 39.12433 & -29.48701 & -60.29473 \\ -1.60623 & 7.42953 & -15.85948 & 11.68702 & -195.06087 \end{bmatrix} \tag{3.31}$$

Pirrung et al. [32] exhibit that the approximation for the final corrected Φ^* (Equation (3.26)) shows a good representation of the optimal Φ for a range of helix angles between 0 and 89 degrees. This range means that with the new correction the NWM can handle cases with no convection (i.e. circular arcs so helix angle is 0 degrees), as well as standstill cases representing a very high wake convection (i.e. straight vortices trailed so helix angle is 90 degrees) and any extent of convection lying in between these limiting cases. It is also noted by Pirrung et al. [32] that the approximation shows deviations when $h/r \to 1$ i.e. representing the induction on root sections from vortices close to the tip. However, this effects only the innermost part of the blade roughly around 5% which is usually just a cylindrical section and effectively has no aerodynamic contribution.

3.3.3 Trailing function modification

The approach presented in Section 3.2 showed that the induction from the most recently trailed vortex element D_w is split into two parts that are calculated at half time steps [5]. This leads to an error in the induction distribution near the root and tip of the blade where the induction is underestimated [5]. In addition, it was stated that the newest vortex

element is a straight line perpendicular to the lifting line. Pirrung et al. [5] improved the trailing function for the newest element to avoid this underestimation of the induction.

The contribution of the newest element to the induction can be expressed in a different formulation based on the chain rule and then multiplying it with the average of the decay function over the length of the newest element. Here $\frac{dw_0}{d\beta}\Delta\beta$ represents the constant induction along an element which is compensated by multiplication with the averaged decay function

$$D_w = \frac{dw_0}{d\beta}\Delta\beta\left\langle\frac{dw}{dw_0}\right\rangle \tag{3.32}$$

From Equation (3.9) if both sides are divided by $d\beta$ the resulting expression can be substituted in Equation (3.32) to get

$$D_w = \Delta\Gamma\frac{r}{4\pi h|h|}\int_0^{\Delta\beta}\frac{dw}{dw_0}d\beta \tag{3.33}$$

and upon replacing the decay function in the above expression with its exponential form shown in Equation (3.11) it can then be integrated to give

$$D_w = \Delta\Gamma\frac{r}{4\pi h|h|}\Phi\left[1.359(1-e^{-\Delta\beta/\Phi}) - \frac{0.359}{4}(1-e^{-4\Delta\beta/\Phi})\right] \tag{3.34}$$

where the terms multiplied with the exponential terms are the new fast and slow decaying components of the induction due to the newest vortex element

$$\equiv \Delta\Gamma\left[D_X(1-e^{-\Delta\beta/\Phi}) + D_Y(1-e^{-4\Delta\beta/\Phi})\right] \tag{3.35}$$

Thus Equation (3.14) becomes

$$X_i = X_{i-1}e^{-\Delta\beta/\Phi} + D_X(1-e^{-\Delta\beta/\Phi}) \tag{3.36a}$$

$$Y_i = Y_{i-1}e^{-4\Delta\beta/\Phi} + D_Y(1-e^{-4\Delta\beta/\Phi}) \tag{3.36b}$$

And D_X and D_Y are defined as

$$D_X = 1.359\frac{r}{4\pi h|h|}\Phi \qquad D_Y = -\frac{0.359}{4}\frac{r}{4\pi h|h|}\Phi \tag{3.37}$$

The axial and tangential components of the D_X and D_Y are simply calculated by multiplying the above by the cosine and sine of the helix angle φ of the vortex arcs.

$$D_{X,axial} = D_X\cos\varphi \qquad D_{Y,axial} = D_Y\cos\varphi \tag{3.38a}$$

$$D_{X,tan} = D_X\sin\varphi \qquad D_{Y,tan} = D_Y\sin\varphi \tag{3.38b}$$

These are the final expressions which are used in the current implementation of the NWM. A benefit of using these factors D_X and D_Y is that they only depend on the discretization of points on the blade and thus can be calculated only once at the beginning of the code as compared to the previous value D_w which had to be updated in every iteration because of its dependency on Δs as exhibited in Equation (3.15).

Another advantage of this modification is that for a steady state implementation, it is assumed that the vortex has been convected to a large enough distance from the blade and that the flow has reached a steady state. In the context of the near wake model this means that a very large value of the angle β should be used. If the original formulation for the slow and fast decaying induction components X and Y is used, then it can be seen from Equation (3.14) that the right hand side would just become zero for large β. With the trailing function modification described here, a high β angle results in the steady state solution of the induction simply being the sum of D_X and D_Y as can be seen from Equation (3.36)

3.3.4 Root correction

It is noted by Pirrung et al. [5] that in cases where the calculation point is far inboard as compared to the vortex trailing point i.e. $h/r \rightarrow 1$, the induction decay function Equation (3.10) and the approximation by Beddoes Equation (3.11) do not reach small values within one quarter revolution. In fact the function values decrease slower comparatively. This means that the contribution from previous vortex elements does not diminish fast enough and the contribution from the new element is compounded on these values, which eventually leads the approximation in Equation (3.36) to evaluate the integral of the decay function to infinity instead of only a quarter revolution.

This was corrected by Pirrung et al. [5] by limiting the NWM steady state induction to one quarter revolution or 90° and dividing by the induction estimated if the integral was evaluated till infinity:

$$C_{root} = \frac{D_w, \pi/2}{D_w, \infty} = \frac{D_X(1 - e^{-\pi/2\Phi}) + D_Y(1 - e^{-2\pi/\Phi})}{D_X + D_Y} \tag{3.39}$$

$$\Phi_C = \Phi C, \qquad D_{X,C} = D_X C, \qquad D_{Y,C} = D_Y C \tag{3.40}$$

This correction factor is then applied to Φ, which in turn gives updated values of D_X and D_Y. This correction essentially improves the estimate of the induction at the root sections due to the tip vortex or vortices that are close to the tip whose influence does not decay for root sections during a quarter revolution.
With these modifications and improvements established, the implementation of the NWM in the current case can be described more appropriately in the subsequent sections.

3.4 Implementation

The following section deals with the implementation of the NWM developed during this thesis and details the algorithm followed while implementing the model. First an overview is presented for the main NWM scheme involving the operations needed to calculate the induction solely from the Near wake. Then the coupled NWM model with BEM equations is introduced and an algorithm for the steady state coupled model is explained in the end.

3.4.1 Scheme for Near Wake induction

First the discretization of points for the vortex trailing locations and calculation points along the blade span need to be specified. The discretization is important because if the points are too far apart the change in circulation cannot be represented accurately enough as the circulation is only defined at discrete points along the blade. This will be explained later in the discussion of the results for the analytical test case.

With the point discretization specified, the h/r ratio is calculated for every calculation point using each vortex trailing point. Through Equation (3.16), the Φ parameter is calculated for all the h/r values. These values are then updated by applying the root correction described in Section 3.3.4. Values of the D_X and D_Y are also already calculated at this step since they are only dependent on the geometric distribution of points. After the geometry dependent parameters have been calculated, the iteration loop can be initiated to calculate the induction.

An initial guess of the axial and tangential inductions W_{ax} and W_{tan} from the near wake is needed for the first iteration to define the complete velocity profile acting at the different points along the span of the blade. Based on this velocity profile, the local angle of attack α_{local} can be obtained at the calculation points which is necessary to calculate the sectional lift coefficient. The sectional lift coefficient is necessary to calculate the circulation at the calculation points along the blade where circulation before the root and after the tip of the blade is defined as 0. Using this the change in circulation $\Delta\Gamma$ can be calculated which gives rise to the trailed vorticity and is used as the strength of the vortex in the induction calculations.

$$v_{axial} = V_0 - W_{axial}$$
$$v_{tan} = \Omega r + W_{tan}$$

$$\alpha_{local} = \tan^{-1}\left(\frac{v_{axial}}{v_{tan}}\right) - twist - pitch \tag{3.41}$$

$$\Gamma = \frac{1}{2} V_{rel} c C_l \tag{3.42}$$

where v_{rel} is the relative inflow velocity calculated from the axial and tangential components. V_0 and Ω are the mean wind speed and the rotational speed of the rotor respectively.

The helix angle φ is considered to be the same as the local inflow angle as the model only takes the near wake effects into account so the angle of the helical arc close to the blade should follow the angle of the inflow velocity profile. As the induction values and hence velocity profile are calculated at the calculation points, the velocity profile is extrapolated to the vortex trailing points in order to get the helix angle for the vortices. The vortex position β after one time step also needs to be calculated using Equation (3.25). The relative velocity for β calculation is again taken at the vortex trailing points. Since the current implementation is a steady state one, the time steps in the original model are treated as iterations. The time t necessary for the computation of β is considered to be a very large value. This ensures that the β angle is large meaning the vortex has moved a large distance away from the blade.

The convection correction discussed in Section 3.3.2 is then applied to the root corrected Φ calculated earlier to get the final Φ^* from Equation (3.26). With this value of the corrected geometric parameter, Equation (3.36) can be used in conjunction with Equation (3.37) to calculate the slow and fast decaying induction components X and Y respectively. The X and Y components are calculated for both in plane and out of plane inductions at each section. These components are then summed to calculate the total induction for that iteration W. The resulting induction is then bounded using a relaxation factor r that limits the solution through Equation (3.43). This has to be introduced because for a steady state implementation the near wake induction could significantly overshoot over one iteration which would result in the solution eventually diverging.

$$W_i = \mathrm{r} \cdot W_{i-1} + (1 - \mathrm{r}) \cdot W_i \tag{3.43}$$

This computed value of W is then compared to the induction that was used to determine the velocity triangle and if the difference is lower than a specified tolerance, then the solution is attained and the calculated induction is correct. In case the difference is higher than the tolerance, the induction W is fed back to calculate a new velocity profile using the inflow conditions and updated induction. The calculation of the velocity profile dependent parameters is repeated in an iterative loop till the convergence criteria is satisfied. This whole process is shown in the flowchart shown in Figure 3.2.

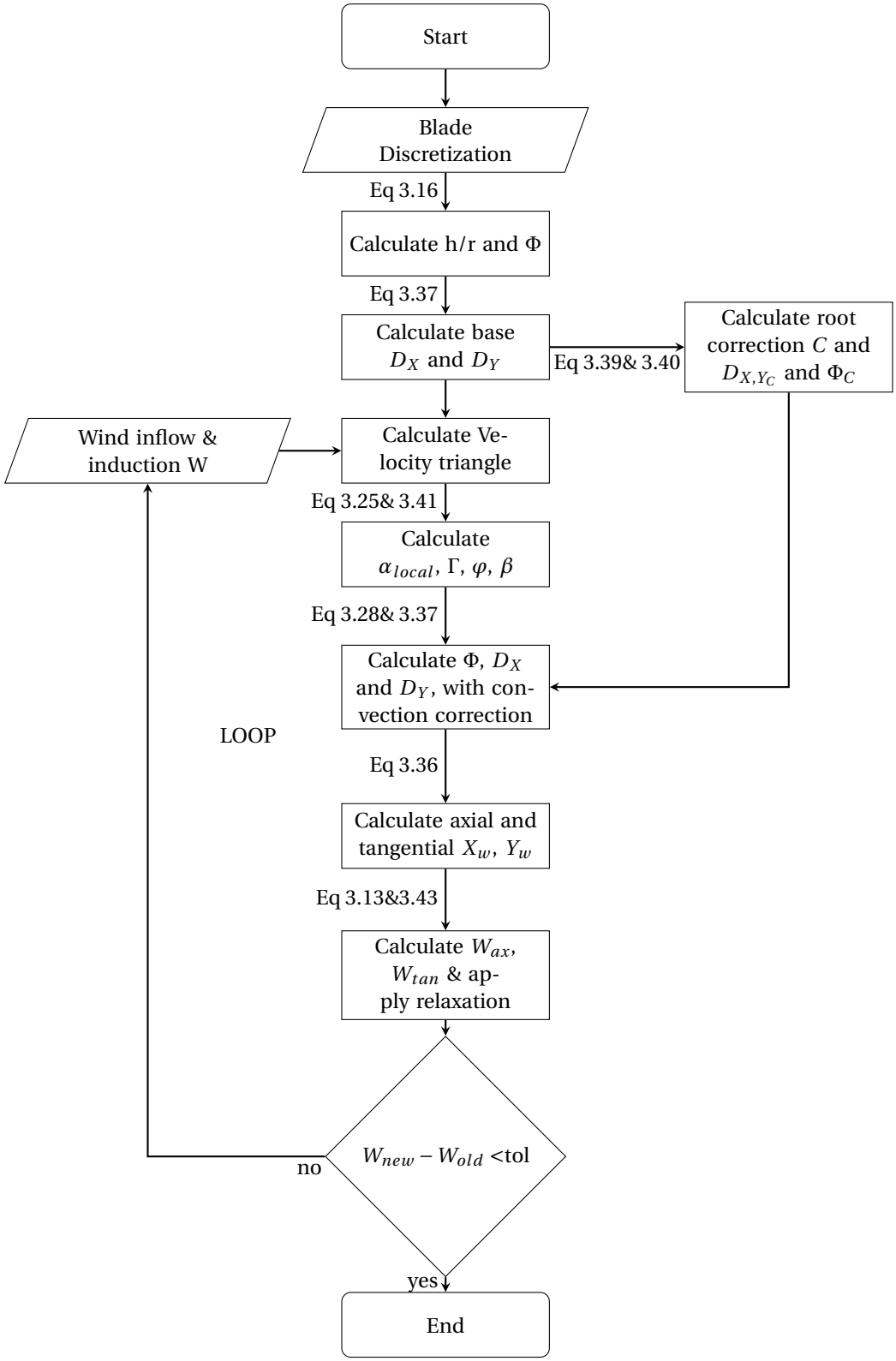

Figure 3.2: Flowchart describing the Near Wake model

3.4.2 Coupled Model with BEM

Model Definition

As mentioned before in order to get an accurate representation of the induction distribution, the NWM has to be coupled with the BEM which provides the far wake effects. This means that the total induction at each section is given as the sum of the near wake induced velocity and the far wake induced velocity u_{FW}:

$$W_{tot} = W + u_{FW} \tag{3.44}$$

As the BEM part of the model is intended to only add far wake effects, the induction from the BEM has to be reduced appropriately. This is necessary so as not to redundantly consider the near wake induction and overestimate the final result. Thus when coupling the two methods, this reduction is provided by multiplying the predicted loads from the BEM method with a certain coupling factor k_{FW}. The coupling factor essentially describes the contribution of the near and far wake to the overall induction distribution. The coupling factor is multiplied with both the in plane and out of plane loads in each iteration to adjust the value of the far wake loads accordingly. This reduction in the loads is then translated into an appropriate reduction in the induction from the far wake. Mathematically this can be shown as in Equation (3.45)

$$C_{T,red} = C_T k_{FW} \tag{3.45}$$

The local induction at each section is related to the differential thrust coefficient at each section. Different functions estimate this relation and one such expression was presented earlier in the form of Equation (2.28). However, irrespective of the function defining the relation between a and C_T, the effect of reducing the thrust is reflected in a modified induction from the far wake.

$$a_{FW,red} = f(C_{T,red}) \tag{3.46}$$

The coupling factor itself is calculated using the value of the far wake induction factor a_{FW} and the induction factor from the near wake a_{NW}. The near wake induction factor is simply calculated by dividing the induced velocity with the incoming wind speed. The goal is to reduce the induction from the far wake so as to satisfy the following condition when averaged over the rotor:

$$a_{ref} = a_{FW} + a_{NW} \tag{3.47}$$

The a_{ref} is the induction from a reference BEM calculation that takes the full differential thrust coefficient without applying the reduction factor k_{FW}. The tip loss factor briefly described in Section 2.1 is also incorporated in this reference calculation. Even though the NWM is formulated in a way that does not warrant the use of a tip loss factor, the use of such a factor is justified in the reference induction calculation. This is because the reference induction is only needed to calculate the coupling factor and scale how much of the total induction comes from the far wake and how much comes from the near wake.

The coupling factor is determined at each iteration of the model for each blade section j. This means that an additional calculation of the reference BEM induction needs to be done in each iteration. However, beyond the calculation of the coupling factor, the reference BEM induction is not needed for any other calculations such as forces or velocity triangles. The expression to calculate the coupling factor as given by [5] as:

$$k_{FW,j}^{i+1} = k_{FW,j}^{i} + \frac{a_{ref,j} - (a_{FW,j} + a_{NW,j})}{\partial a / \partial k_{FW}} \tag{3.48}$$

where the change in the induction with the change in the coupling factor $\partial a/\partial k_{FW}$ can be derived using the relation that describes the induction as a function of the thrust coefficient and replacing the thrust C_T with the reduced thrust $C_T k_{FW}$.

This sectional coupling factor is then averaged over the area of the whole rotor by summing the product of the coupling factor and sectional area A_j and dividing this by the area of the whole rotor. This results in a single coupling factor for the entire blade length which is then used in the next iteration.

$$k_{FW} = \frac{\sum_{j=1}^{N} k_{FW,j} A_j}{A} \tag{3.49}$$

Note that the coupling factor was calculated to get the same total induction from the coupled model as from a reference BEM model at each section. This essentially means that we rely on the BEM for the overall induction level but local effects are added to the induction distribution through the effect of the near wake and the near wake model.

Flowchart for coupled model

The flowchart for the coupled model in the steady state implementation is shown in Figure 3.3. There are three main loops that are necessary for the model to function correctly. Loop 1 is the main loop that represents each iteration of the model. Loop 2 represents the BEM loop which runs iteratively to get converged results of the far wake. The converged results of the far wake from Loop 2 are then used as a starting point for Loop 3 which is the Near wake loop of the model and runs iteratively to get the induction from the near wake.

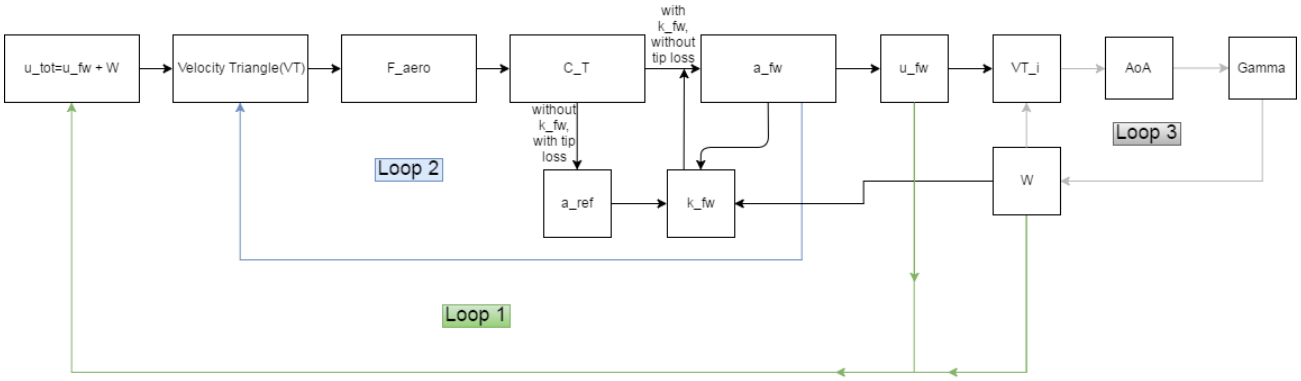

Figure 3.3: Algorithm for steady state implementation of the coupled NWM

Each iteration starts by summing the induced velocities from the near and far wake part. Based on the total induced velocity a velocity triangle is formed and the aerodynamic loads are calculated for this velocity profile. Next, the far wake induction is calculated with the reduced coupling factor and at the same time, the reference BEM induction is estimated. As shown in Figure 3.3, only the reference calculation includes the tip loss factor and this was explained in the previous section. This reference BEM value is then used in conjunction with the estimate of the near wake and the far wake inductions to calculate the coupling factor k_{FW} for the next iteration of the main loop. The coupling factor is adjusted using a relaxation factor so as to assist the convergence. These steps are repeated in Loop 2, with a changing far wake induction u_{FW} and fixed near wake W. The loop runs until the far wake induction converges and the difference between the new and old u_{FW} is less than a specified tolerance. A relaxation factor is incorporated in the calculation of the far wake induction as well in order to avoid divergence of the solution.

With this fixed far wake induction, a new intermediate velocity triangle can be formed at the start of loop 3 and then the near wake calculations are performed keeping fixed until a convergence criteria is satisfied for the Near-Wake part. The near wake calculations are done iteratively in Loop 3 using all the steps described previously in the flowchart in Section 3.4.1. With a converged induction W from the Near wake calculations, the value is fed back to the velocity triangle in the beginning of Loop 1 and the process repeats.

As explained Loop 1 is the main loop which is repeated iteratively with a converged set of far wake and near wake inductions and then these are updated in Loops 2 and 3 respectively. During the first iteration, the near and far wake inductions are assumed along with an initial estimate of the coupling factor k_{FW} for the first iteration. The time steps that are a part of the original Near Wake model are thus replaced with iterations of the main loop in the implementation developed in this study.

The steady state implementation, developed during this study removes the parts of the near wake model which model dynamic effects due to shed vorticity. A significant change in the steady state case is the addition of Loop 2 for the BEM calculations. Essentially, in the dynamic near wake model, very small time steps $d\tau$ are considered for the solution. This means that for one time step, the solution only progresses by a small amount. In the steady state version, it was seen that the far wake induction would change drastically over one iteration of the main loop. Thus, in each iteration, the far wake would change too much, making convergence more difficult for the entire solution. This

is fixed by adding an additional loop that makes the far wake induction reach a converged value before progressing to the near wake loop. With the addition of this loop, convergence is achieved.

The next chapter will detail the test setup for the model to test its performance. The rotor and the operating points for the analysis will be introduced. The CFD simulation setup will also be discussed for the comparisons that will be carried out between CFD and the model.

Chapter 4

Test Setup

The operating conditions and rotor geometry are the inputs for any wind turbine performance code. For testing purposes of the current model, the DTU 10 MW reference wind turbine is used [6]. The current chapter covers some practical information of the DTU 10 MW turbine and the operating points used for the simulations and comparisons. In addition to this, the CFD setup is described with domain description and mesh size. A brief discussion on the current induction calculation method follows. The geometry modification criteria and the modified geometries for the uneven loading cases is presented in the end of the chapter.

4.1 DTU 10 MW Reference Wind Turbine Description

The DTU 10 MW reference rotor was designed as part of the Light Rotor project [6]. It establishes a reference for future designs to be compared to it as the size of turbines continues to grow ever larger. Even though the project focused on a rotor design, the entire wind turbine is designed and documented in [6] including the controller, tower and the drive train. For a more detailed description of the rotor performance and the parameters defining the other components, the reader is guided to the official report [6]. A few noteworthy parameters of the rotor and its operation are listed in Table 4.1.

Table 4.1: Parameters of the DTU 10 MW RWT

Description	**Value**
Rating	10 MW
Rotor Orientation	Upwind, 3 bladed
Control	Variable speed, collective pitch
Hub Height	119 m
Rotor Diameter	178.3 m
Hub Diameter	5.6 m
Blade Length	86.4 m
Cut-in speed	4 m/s
Rated wind speed	11.4 m/s
Cut in rotor speed	6 rpm
Rated rotor speed	9.6 rpm

As the focus of this study is on an aerodynamic model, the chord and thickness distribution of the rotor are obviously very important inputs for the model. These two are presented in Figure 4.1 plotted against the radial distance of the blade.

For the operating points that are selected for the comparisons, the settings are chosen from the prescribed optimum operating points for the DTU 10 MW wind turbine obtained through HAWCStab2 [33]. Due to limited cluster

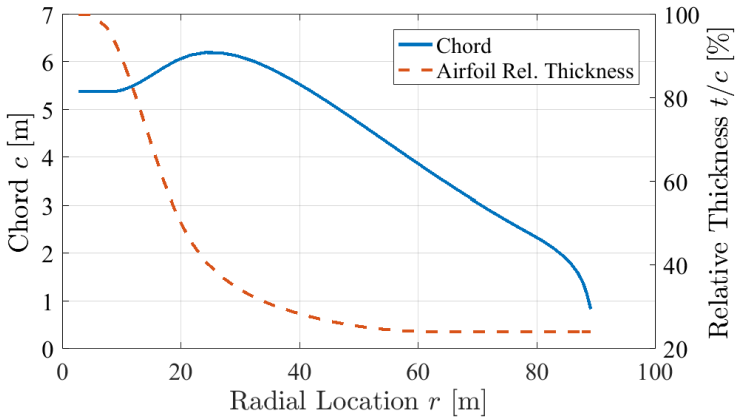

Figure 4.1: Chord and thickness distribution of the DTU 10 MW turbine [6]

availability, the following points are chosen and identified as points of interest. The first two operating points shown in Table 4.2 are selected as these are close to the rated wind speed of the turbine lying slightly below and right after the rated wind speed. These are important because the performance of the rotor and thus the model is important near the "shoulder" of the power curve. Slightly below the rated wind speed, the highest loads and thus strongest blade deformations are expected. The higher wind speed, namely 25m/s, is chosen to analyze the performance of the model in comparison with CFD at higher wind speeds, as high wind speed performance of the model in steady state is also an interesting case for study.

Table 4.2: Operating points chosen for the comparison

Wind Speed [m/s]	**Pitch [°]**	**Rotational Speed [rpm]**
7	0.00	6.00
10	0.00	8.03
25	22.97	9.60

Using these operating points, the model and the CFD simulations are carried out for a reliable comparison of the coupled model in steady state.[1]

Airfoil Polars for the DTU 10 MW rotor

The selection of airfoils in a rotor is also an important driving factor in its aerodynamic performance. For lower fidelity aerodynamic models, the airfoils are modeled through airfoil polars which are obtained experimentally or through CFD simulations. Airfoil polar data is thus an important input for both the BEM and the coupled model and reliable estimates are necessary to eliminate inaccuracies and uncertainties in model results.

The airfoil polars for the DTU 10 MW RWT are presented in the discussion of the test setup because these polars affect the outcome and results of the models. The airfoils used have thicknesses to chord ratios of 24.1,30.1,36,48 and 60%. The polars used by the aerodynamic models in this study are presented in Figure 4.2 through 4.4 and are obtained from the online repository of the DTU 10 MW RWT [34].

[1] Note that the 10 m/s wind speed is only used for some result cases and it will be explicitly mentioned when these results are presented

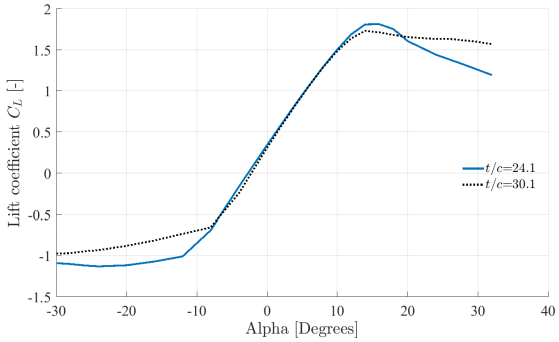

(a) C_L versus α

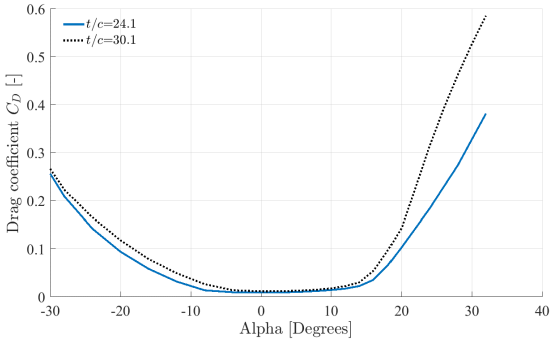

(b) C_D versus α

Figure 4.2: Airfoil polars for airfoils with t/c=24.1% and 30.1%

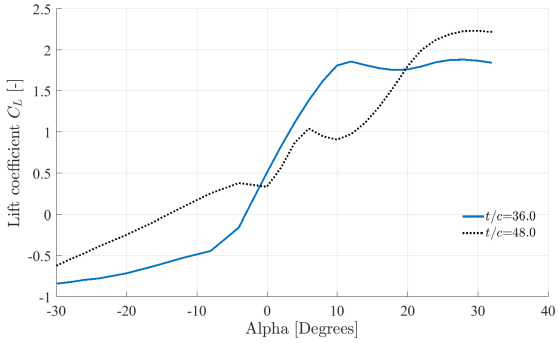

(a) C_L versus α

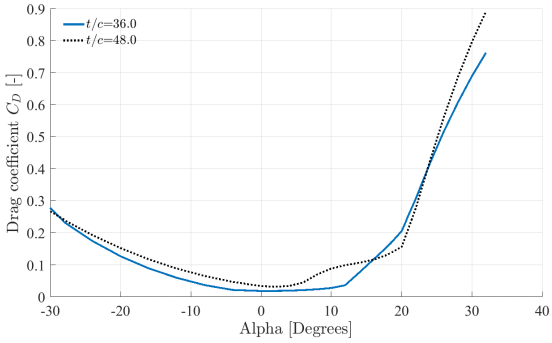

(b) C_D versus α

Figure 4.3: Airfoil polars for airfoils with t/c=36.0% and 48.0%

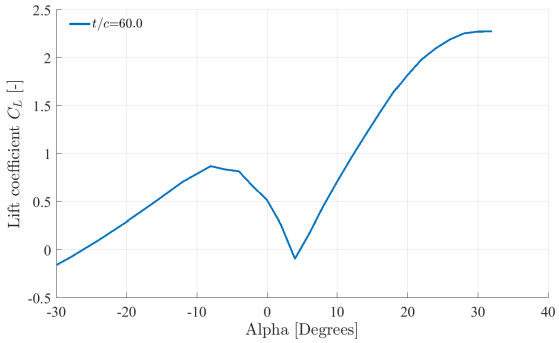

(a) C_L versus α

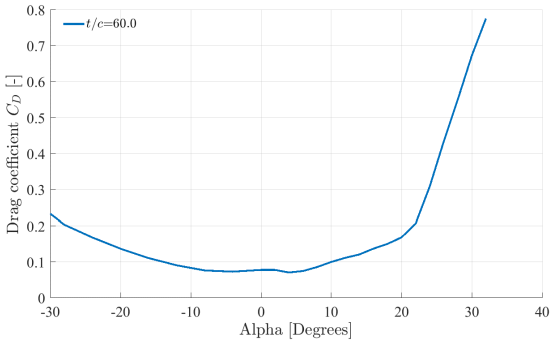

(b) C_D versus α

Figure 4.4: Airfoil polars for airfoil with t/c=60%

These airfoil polars are obtained through EllipSys 2D CFD computations and have been 3D corrected using a correction model by Bak et al. [35]. The CFD settings for these polars model laminar flow with free transition to turbulent flow. The transition is modeled based on a Turbulence Intensity (TI) of 10% at the rotor. It can be seen that the 24, 30 and 36% airfoils have rather conventional lift coefficient curves with large maximum C_L. On the other hand

the lift curves for the 48 and 60% t/c airfoils show a rather strange behavior in Figures 4.3a and 4.4a. This is due to the fact that these airfoils have simply been obtained through interpolation between a cylindrical section and other existing airfoils and their performance is therefore obviously not optimal. This performance uncertainty makes the polars and the results based on the polars to be unreliable at best. However, these airfoils are only used in the root section of the blade up to ≈ 30% of the blade span. Therefore, the results in these regions of the blade cannot be used to make reliable conclusions on the performance of either BEM or the coupled model.

4.2 CFD Setup, Domain Description and Mesh Size

The CFD computations in the current study are carried out using the commercial CFD software ANSYS® CFX, Release 15.0. The Reynolds-Averaged Navier-Stokes (RANS) equations are solved in the simulations. The turbulence model employed is the $k-\omega$ SST model and as was stated in Section 2.2 this model is most widely used in resolving the flow in the region close to the blade which makes it a good comparison reference for the Near Wake model.

The flow field itself is discretized by means of a structured and unstructured hybrid mesh. The outer mesh is a tetrahedral unstructured mesh ranging 10 rotor radii in both upstream and downstream directions. In the radial direction the extent varies between 8 to 11 radii. Closer to the blade, the mesh is structured and hexagonal. The cells closest to the blade have a height of 10^{-6} m. This means that the non-dimensional wall distance y^+ lies between the extents of 0.5 and 5. To resolve the tip vortex better, the cell density near the tip is also higher than the other regions.

The simulations are ran on parallel cores and the simulations require around 1300-2500 iterations to converge. The convergence criteria is based on the power when it crosses its local value. The rotor is modeled using appropriate boundary conditions and the geometry of a single blade is used to represent the rotor with these boundary conditions. With regards to the blade geometry, the blade is modeled first with a coning angle of 5° and an undeformed geometry. The first set of results in Chapter 5 are presented with this blade geometry. All subsequent results in that chapter are then shown with the geometry as a straight undeformed blade having zero coning. This is useful for a more reliable comparison since both the aerodynamic models that are considered in this study do not take out-of-plane deformation or coning angles into account.

In addition to these parameters, two different sets of CFD simulations are obtained for comparison to the results from the aerodynamic models. The first set of simulations represent the flow being laminar with free transition to turbulent conditions and the second considers fully turbulent flows. The fully turbulent case describes the performance of the blade if it was soiled. The results chapter will only showcase the laminar flow with free transition case for the DTU 10 MW RWT and the results for the fully turbulent case are added in the Appendix. The study focuses on the free transition case because of the airfoil polars for the DTU 10 MW RWT shown in the previous section. Since the aerodynamic models use these polars which are obtained for free transition of laminar flow, the results should be compared to the free transition CFD simulation. However, it is also important to mention that for the CFD simulations, the turbulence intensity used to model free transition is almost negligible. Where in the case of the airfoil polars the free transition was modeled for a turbulence intensity of 10% implying a higher level of turbulence considered for the polars. Despite these turbulence intensity differences, the model results are still compared with free transition CFD results for consistency, as the 2D polars are obtained based on the same flow behavior.

4.3 Calculation of Induction from CFD results

The current study involves comparing the induction results to CFD simulation results. In order to have a reliable comparison, the calculation of the induction from the CFD simulations must also be accurate and reliable. The comparison for parameters that are directly output from CFD is therefore more straightforward as compared to those parameters which require additional post processing. Forces acting on the turbine blade in and out of the rotor plane are a direct output from CFD results and therefore can be presented directly as will be shown later in Chapter 5. In the case of the inductions however, special attention needs to be paid. This is required because the induction then influences the angle of attack and thus the lift and drag acting on the rotor blade.

Different methods for calculating the induction from CFD simulations are known, however the uncertain credibility of most of these methods makes the calculation of induction from CFD a questionable subject. Guntur & Sørensen [36] reviewed some of these methods and presented a general description of the merits and limitations of the different methods. The two most common approaches to calculate the induction however are the reverse BEM and averaging method. In the reverse BEM, the loads from the CFD simulations are fed to a BEM loop which calculates the induction based on the prescribed loads from CFD. In this study however, using the reverse BEM method would be counterintuitive especially to get the induction since the very aim of the study is to improve the BEM model. Additionally, the reliability of this type of approach was questioned by Guntur et al. [36] for investigating three dimensional unknown effects such as the effect of uneven loading or induction on the rotor performance.

At this point, it is important to mention the difference between local and global induction. In terms of physical description, the global induction is the averaged induction over the ring element and the local induction is the value at the blade. For a finite number of blades on a rotor, the local induction a_l is different from the global induction denoted by $\overline{a}$. Shen et al. [37], actually describe the tip loss factor as the ratio of the global induction $\overline{a}$ to the local induction a_l. This suggests that the local and global induction are different for rotors with finite blades because of the tip loss effect which arises when considering a real rotor as opposed to an actuator disc. Elaborating on this, the tip loss factor is described as a parameter that defines the difference between the local and global induction according to Shen et al. [37]. Various methods are found in literature to estimate the local induction through CFD. Guntur et al. [36] suggest interpolating the induction at the blade after calculating the induction at all azimuth locations in the rotor blade. These estimated inductions are then interpolated at the azimuth position of the blade. However, this method leads to concerns with the exact position of the blade and the actual extent of the blade. A different approach was prescribed by Branlard [38] that takes the extent of the blade into account in a better way. Despite being more physical as opposed to the azimuthal averaging, even the approach by Branlard is not reliable for determining the local induction. Even though these methods to calculate the local induction from rotor CFD simulations exist, they are not very accurate or reliable and thus the current study focuses on the global induction from the simulations. No single method to estimate the induction is accepted as being legitimately better than the others. But the one that is most commonly used is the averaging technique mentioned above. Keeping this in mind the current study uses the averaging technique for obtaining the global inductions from CFD.

The simplest explanation for the averaging method is that it involves averaging the axial velocity in the vicinity of the blade immediately upstream and downstream of the blade. Different planes can be defined close to the blade for the determination of the average velocities at these planes. These planes are further divided into arcs to calculate the average velocity at each radial location in these planes. The induction value is calculated by taking the mean of the averaged velocities at the planes. This description for the averaging method is given by Guntur et al. [36] and different methods can be used to refine this basic approach. The Figure 4.5 shows how a 120° plane is selected ahead of the blade. Because the CFD computations rely on rotor symmetry, a 120° annular plane can be used for calculating the velocity profiles. Another plane is selected immediately downstream and then these planes are broken into smaller arcs to calculate the average velocity at the plane for each radial location. Since the global induction is defined as the induction averaged over the ring element it is clear that this averaging method results in the global induction. This leads to some differences between the induction from the models and the induction from CFD which are presented in Chapter 5. This is discussed and explained later in the discussion part of the report.

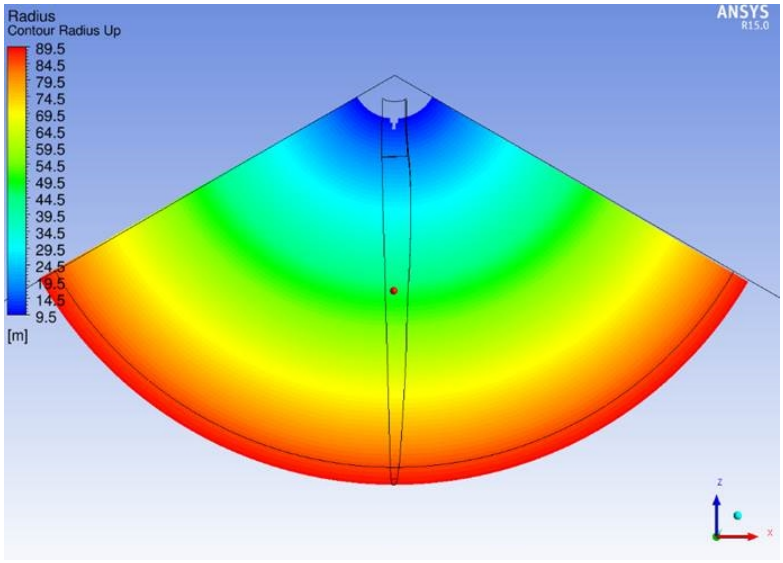

Figure 4.5: Definition of the induction plane for CFD calculation in the case of the DTU 10 MW rotor blade

4.4 Geometry Modifications for Uneven Loading

In light of the research questions highlighted in the introductory chapter, investigating the performance of the NWM when it comes to blades with uneven loading distribution is also an important goal of this study. For this comparison, the blade geometry is augmented in different ways to represent changes in the chord that result in such uneven loading. There are two different kinds of augmentations used in the current study;

- A local chord increase at a specified location along the blade span
- A chord augmentation through the entire blade span that results in a more slender blade outboard

Local chord increase

The first type of geometry modification involves simply modifying the chord by a specific percentage of the chord at a local section of the blade. Two different geometries with chord increases of 10% and 20% are generated. The chord increase is applied in the range of 60-75% of the blade span. However, in order to avoid convergence issues in CFD simulations for such an abrupt change, this change in the chord is smoothened out.

The chord is smoothed by applying intermediate modifications on larger sections of the blade surrounding the actual blade span region selected for modification. These intermediate modifications involve small incremental chord increases until the desired final percentage increase is achieved in the span section ranging from 60-75%. Then using these multiple intermediate modifications, a final chord distribution is obtained using spline interpolation. The Figure 4.6 demonstrates visually the abrupt increase in chord between 60-75% blade span, the different intermediate chords and the final spline chord distribution.

Using this technique two blade geometries are generated with 10% and 20% chord increase. These geometries are shown in Figure 4.7. Even though the geometry modifications are quite smooth and the transition to a larger chord is gradual, it is expected that the circulation distribution is affected sufficiently to study the required unevenness in the loading.

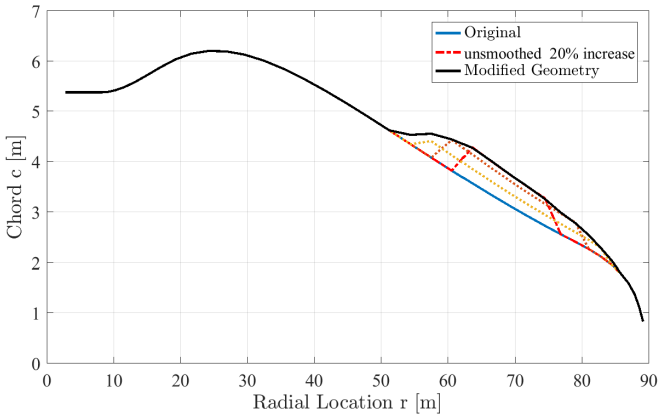

Figure 4.6: Chord modification illustration, the dotted lines show two of the intermediate chords described

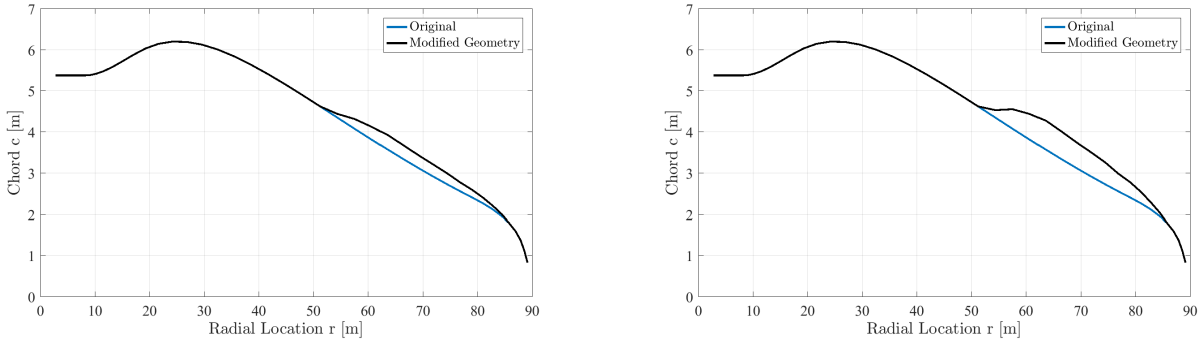

(a) 10% increase, Geometry *Local A*

(b) 20% increase, Geometry *Local B*

Figure 4.7: Geometry augmentation type I, local chord increases around 60-75% of blade span

Slender blade modification

The second type of geometry modification aims to test blades with a slender platform having a higher chord inboard and further outboard the chord decreases resulting in a more slender blade profile. This type of geometry is considered because more and more slender blades are being designed and considered in the wind turbine industry and thus it is a good test case to see the model behavior for these type of blades.

Like the local chord increase described in the section above, two different geometries were considered in this case as well. The approach used to modify the geometry in this case was to increase the chord of the blade by a certain amount starting from 20% blade span and then gradually decrease the amount by which the chord is changed. Eventually, this change becomes negative and the outboard sections are then decreased in chord as compared to the original blade. The aim was to keep the rate of change of the chord more or less the same as an estimate. This was done to ensure that there are no kinks or chord slope changes along the blade span.

Figure 4.8 shows the two different slender blade geometries generated. The figure on the left corresponds to a maximum chord increase of 5% at the root sections which gradually decreases as described above. The figure on the right has a maximum chord increase of 10%, both starting from the radial location at 20% of the blade span.

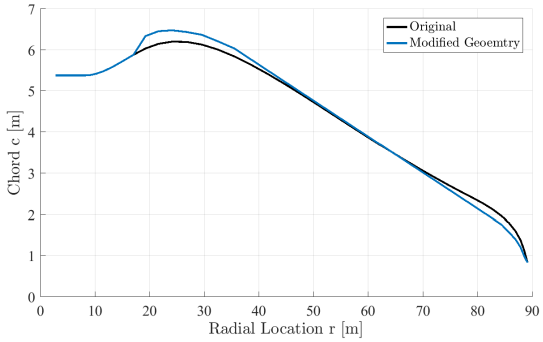

(a) 5% increase, Geometry *Slender A*

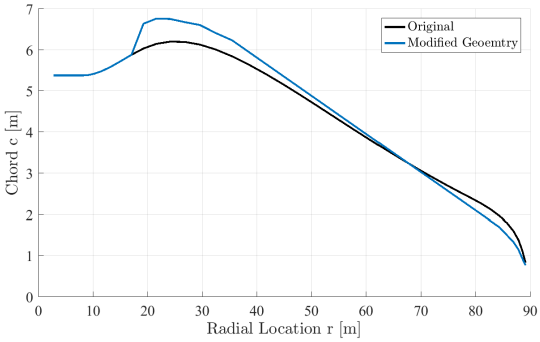

(b) 10% increase, Geometry *Slender B*

Figure 4.8: Geometry augmentation type II, Slender blade geometry with chord modification throughout the blade span

To summarize this chapter before revealing the results of the coupled model, a table describing the notation and important aspects for the geometries in the subsequent discussion is presented. The maximum chord increase and decrease columns show the maximum change in the chord relative to the original geometry and for the slender geometries, the decrease is maximum at the tip.

Table 4.3: Different geometry parameters

# [−]	**Notation**	**Part of span affected** [%]	**Max Chord increase** [%]	**Max Chord decrease** [%]
1	Local A	≈ 60-75	10	-
2	Local B	≈ 60-75	20	-
3	Slender A	Entire Span	5	≈ -12
4	Slender B	Entire Span	10	≈ -16.5

Chapter 5

Results

This chapter begins with an analytical test case to validate the induction calculation from the Near wake model alone. This is followed by the results from the different simulations and a comparison is presented between the results of the steady coupled model and standard BEM with CFD results. Next, a comparison between HawC2 and the developed coupled model is presented to validate the results. The last section shows the results from the augmented geometry simulations to analyze the uneven loading distributions. Remarks and observations are provided about visible trends however explanations for these results follow in the discussion part of the report in Chapter 6.

5.1 Analytical test case for an elliptical wing

The analytical case involves validating the near wake induction calculation from the model. This is done for the case of an elliptical circulation distribution since the analytical solution for the induction in such a case is known from fundamental aerodynamic theory. The reader is guided to [24] for a deeper look into the theory of an aircraft wing with an elliptical circulation distribution. This test case is also important to see the effect of the point discretization scheme and to decide the type of point spacing that best describes the circulation distribution.

For the validation of the NWM induction, a wind turbine blade of 10m length attached to a 0.5m hub is considered. The blade is non-rotating (i.e. Ω =0) and is pitched out 90° so that it behaves like an aircraft wing to the incoming wind speed of V_0 =35m/s. There is a constant twist of -5.45° along the blade. The blade is assumed to have an elliptical chord distribution with a maximum chord value c_0 of 5.21m. Equation (3.42) showed that the circulation depends on the chord c, thus the resulting circulation distribution for such a blade (having constant twist and uniform inflow conditions) should also be elliptical. From aerodynamic theory it is known that an elliptical circulation distribution leads to a constant downwash along the span of the blade depending on the maximum circulation value Γ_0 and the blade span S [24].

$$W_{analytical} = \frac{\Gamma_0}{2S} \tag{5.1}$$

In the current case, the chord distribution is represented as a function of the position y along the blade span S as:

$$c(y) = c_0\sqrt{1-\frac{y-5.5}{S/2}} \tag{5.2}$$

where c_0 is the maximum chord value and lies at the center of the blade. Correspondingly, the maximum circulation value Γ_0 for this distribution and given inflow conditions is 30 m^2/s. And for a 10m blade, this means that the constant downwash induced along the blade span is 1.5m/s from Equation (5.1).

Using the steps described in Section 3.4.1, the near wake induction is calculated for the blade described above with the given inflow conditions. The results for this test case are shown in Figure 5.1. The discretization used is a full cosine point discretization with 40 points. A good match is seen between the induction from the analytical solution and the induction calculated from the iterative near wake calculations. The small difference arises because of the

approximations that are used in modifying the φ parameter for the convection correction. For a straight helical vortex line the k_φ in Equation (3.26) should be equal to 1. With the approximations descirbed in Equations (3.28), (3.30) and (3.31), it is almost equal to 1 for this analytical case. If this factor is set equal to 1 an even closer fit can be seen with the NWM for the analytical comparison.

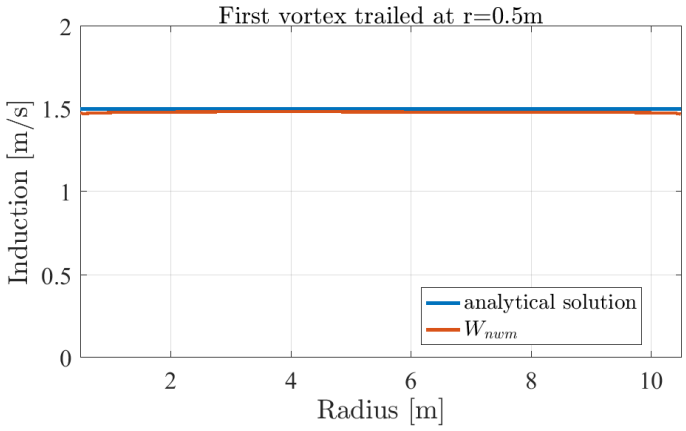

Figure 5.1: Analytical test case comparison for a 10m elliptical blade

The choice of discretization is important for most lifting line models because they rely on the circulation distribution along the span of the blade. Using an equidistant point spacing thus means that the circulation is not represented accurately since a discrete circulation value is maintained over larger sections of the span. This means that in regions where the circulation distribution changes drastically such as the root and tip, the change in circulation will not be resolved well enough for an equidistant spacing. This is graphically presented in Figure 5.2 where a equidistant spacing is compared to a cosine discretization at the root section of the 10m blade described in the discussion above. The cosine discretization uses a finer grid spacing near the root and tip of the blade which means the circulation described by the discrete points is closer to the analytical or actual circulation distribution.

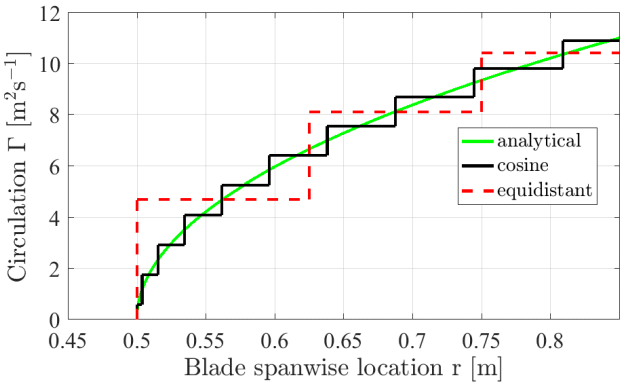

Figure 5.2: Comparison of different discretization schemes in describing the circulation distribution

Based on this, the BEM and coupled model results shown in the following section utilize a full cosine point discretization. The blade is discretized into 80 points which is deemed to be sufficient for the given rotor.

5.2 Comparison for DTU 10 MW rotor

The following section shows the various simulations done for different wind speeds. The results are compared for CFD simulations with and without rotor coning. The CFD simulations presented in this section model laminar flow with free transition to turbulent since this is the flow setting for which the airfoil polars are obtained. A separate comparison for fully turbulent CFD flow is also done and these results can be seen in Appendix A.

The first set of results shows the DTU 10 MW RWT with a 5° coning angle with no deformation in the blade. The second set of results presents CFD simulations without any coning in the rotor geometry, in addition to an undeformed blade just like the first set of results. Within each subset, the induction factors are presented first plotted against the radial location along the blade. This is followed by the out-of-plane and in-plane loads also plotted along the non-dimensional radial location.

5.2.1 CFD simulations with Coning

Axial Induction factors

The first plots show the axial induction factor a plotted against the radial location along the blade for two wind speeds. The title of the following plots shows the wind speed and the identifier for the flow conditions used in CFD, 'c' stands for clean blade or flow with transition from laminar to turbulent. The plots show that the induction value fits well with CFD for both BEM and the coupled model except for the root sections. Furthermore, the effect of the tip vortex is seen in the aerodynamic models with a large induction at the tip, this is not represented in the induction from the CFD simulations as seen in Figures 5.3a and 5.3b.

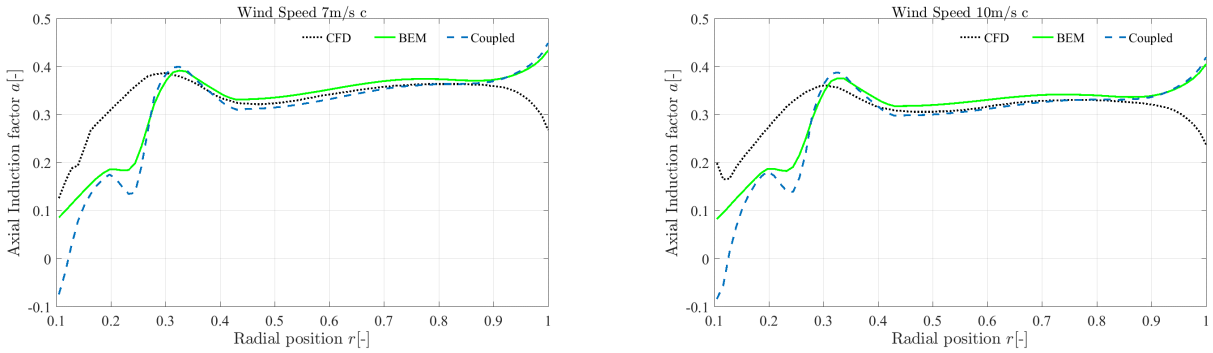

(a) 7 m/s

(b) 10 m/s

Figure 5.3: Axial induction factor comparison for rotor with coning

The difference at the tip for the different methods is caused by the induction calculation method and is explained later in the discussion chapter. In order to make a fair comparison between CFD and the aerodynamic models however, the results from the aerodynamic models are multiplied with the tip loss factor. The Figures 5.4a and 5.4b show these results and a better fit is seen with CFD for the coupled model as compared to the original BEM model.

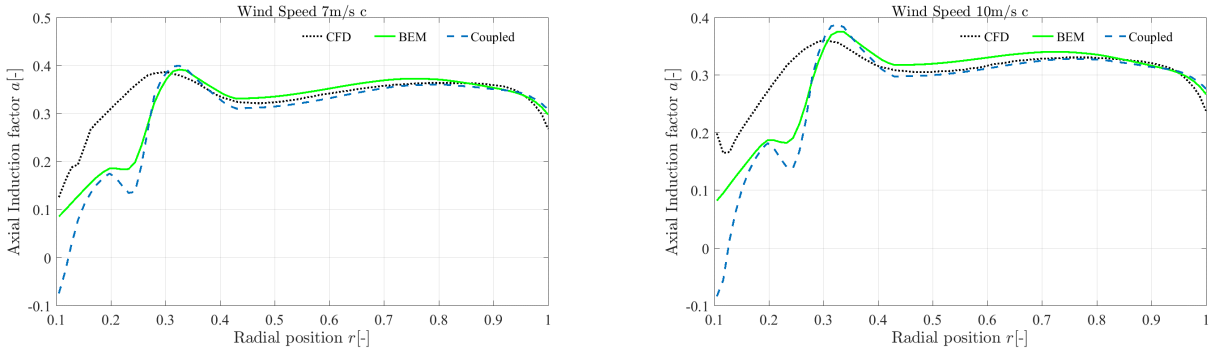

(a) 7 m/s (b) 10 m/s

Figure 5.4: Axial induction factor comparison for rotor with coning and tip loss multiplied

Tangential Induction factors

The Figures 5.5a and 5.5b give the tangential induction factor plotted against the radial locations. Apart from the root sections, it is seen that both give the same tangential induction along a major part of the blade and also lie on top of the CFD results.

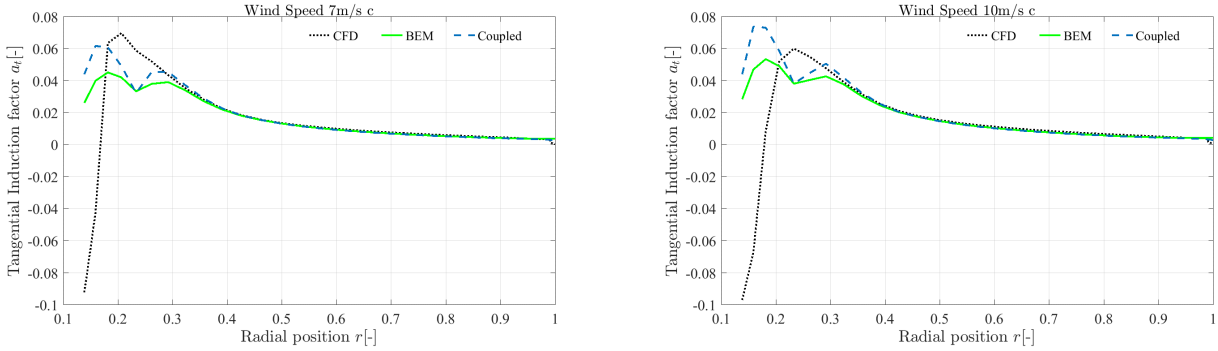

(a) 7 m/s (b) 10 m/s

Figure 5.5: Tangential induction factor comparison for rotor with coning

For the remaining cases, a similar behavior was seen, and therefore these plots will not be presented and can be found in the appendix.

Out-of-plane loads

Next, a comparison of the out-of-plane loads through the two models is shown with CFD in Figures 5.6a and 5.6b and it is seen that the coupled model in this case gives slightly higher loads than the original BEM model apart from the root sections. However, this slight overestimation still shows a good fit with the CFD results in general.

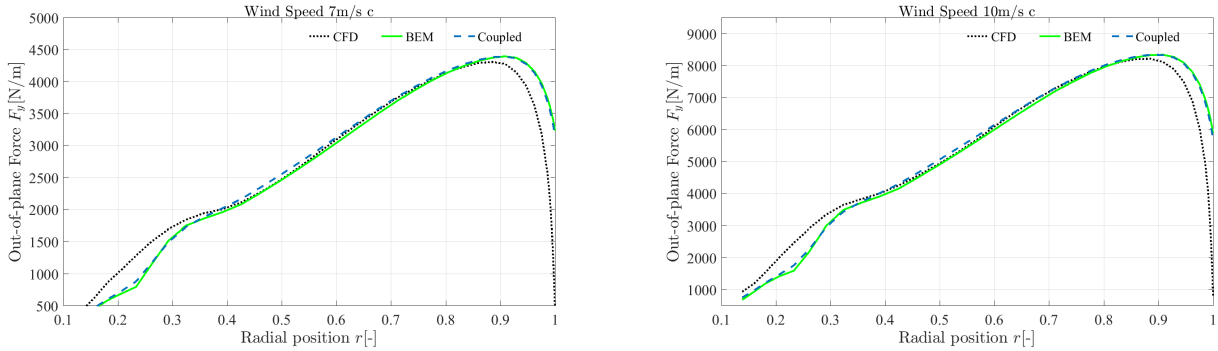

(a) 7 m/s (b) 10 m/s

Figure 5.6: Out-of-plane loads comparison for plain rotor with coning

In-plane loads

The in-plane loads are plotted against the non-dimensional radial position and compared in Figures 5.7a and 5.7b and here a significant difference is seen with the coupled model as the original BEM model is seen to have a constant deficit in comparison to the CFD results while the coupled model is closer to CFD over a wide section of the blade. Both the models however tend to drop to lower values as compared to CFD in the outboard sections of the blade and are higher than CFD at the tip.

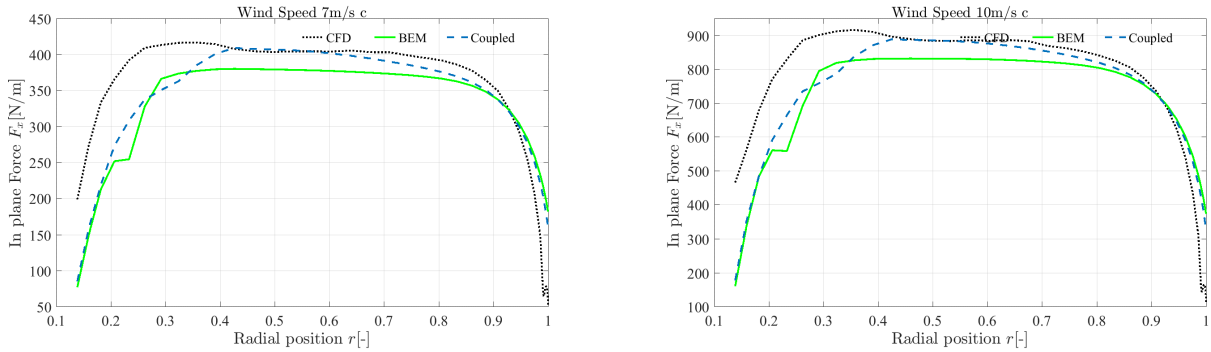

(a) 7 m/s (b) 10 m/s

Figure 5.7: In-plane loads comparison for plain rotor with coning

5.2.2 CFD simulations without Coning

In this section the results are presented in the same sequence as in the previous section with a few changes. The axial induction is shown only after multiplication with the tip loss factor to give a consistent comparison with CFD results. The tangential inductions are omitted in this section since the results do not show any difference between the three compared methods. The tangential induction results are included in Appendix B.

Axial Induction factors

The Figures 5.8a and 5.8b show the axial induction factor a plotted against the radial location along the blade for two wind speeds. A high wind speed of 25 m/s is considered for these CFD results without coning. The inductions obtained from the aerodynamic models tend to different values at the tip if not multiplied with the tip loss factor as was seen in the previous section in Figure 5.3. However as mentioned above these results are presented after multiplication with the tip loss factor.

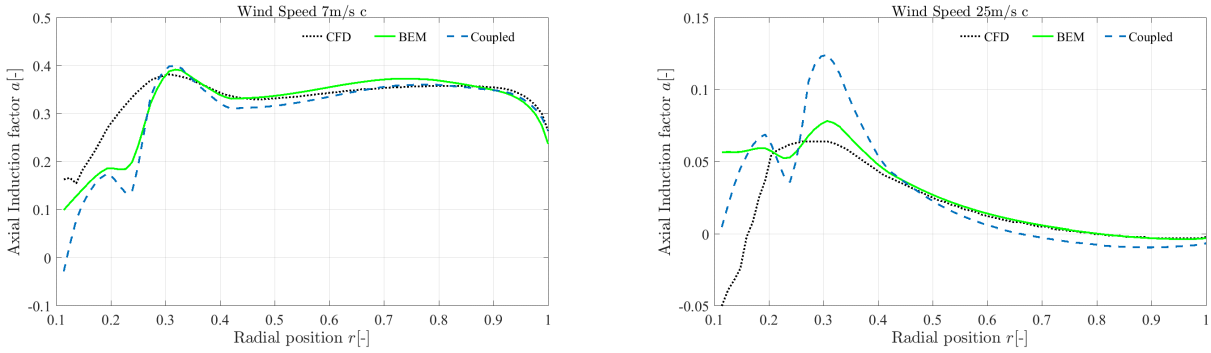

(a) 7 m/s (b) 25 m/s

Figure 5.8: Axial induction factor comparison for rotor without coning

Out-of-plane loads

Next, a comparison of the out-of-plane loads through the two models is shown with CFD in Figures 5.9a and 5.9b. Both models show good agreement with the BEM being slightly further off.

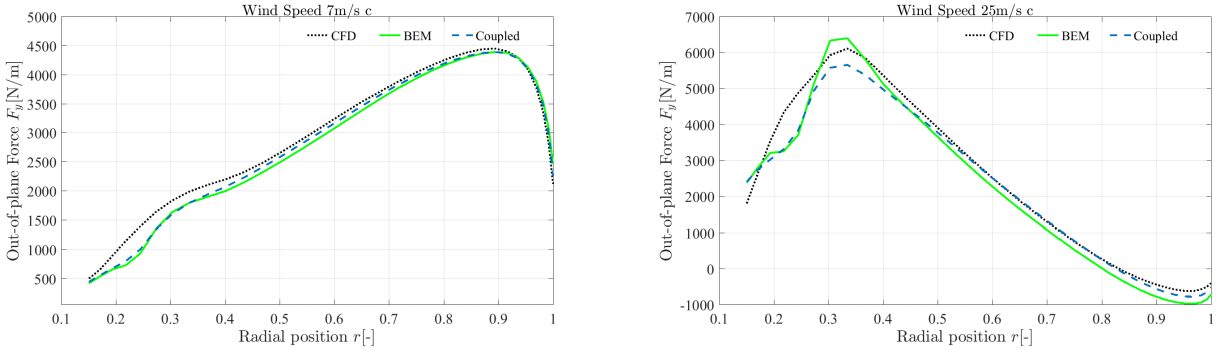

(a) 7 m/s (b) 25 m/s

Figure 5.9: Out-of-plane loads comparison for rotor without coning

In-plane loads

The in-plane loads are presented next plotted against the non-dimensional radial position and compared in Figure 5.10. Here again the deficit is seen between BEM and CFD. The tip region is more closely aligned for both models.

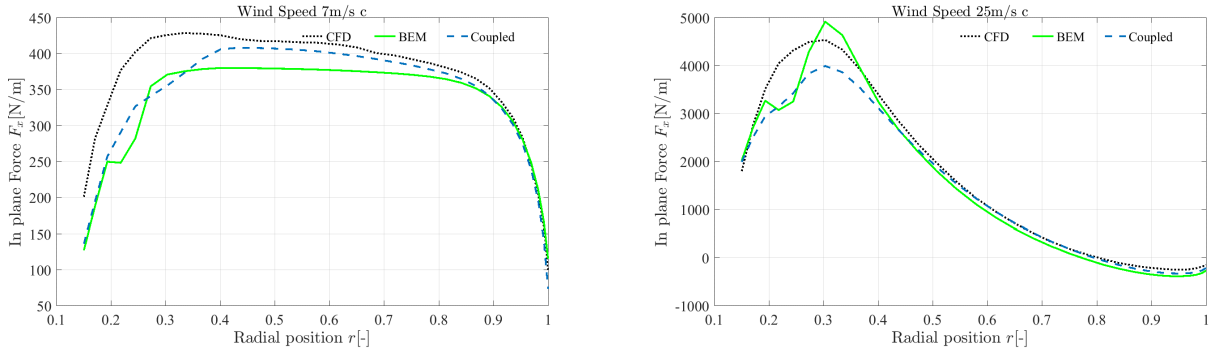

(a) 7 m/s (b) 25 m/s

Figure 5.10: In-plane loads comparison for rotor without coning

5.3 Comparison of results with HawC2 simulation results

For the purpose of validation, a few HawC2 simulations are carried out for the DTU 10 MW RWT for the same operating conditions used so far in this study. The rotor is considered to be undeformed and prescribed constant pitch settings are used from the operating conditions matrix in Table 4.2 in order to get a fair comparison between the dynamic code and the steady state NWM coupled code. The HawC2 simulations run for 100 seconds after which the response of the turbine is considered to be converged to a steady value which is suitable to compare the results from the coupled model to the HawC2 code.

Axial Induction factors

First the axial inductions are presented for two wind speeds that were shown for the no coning case in the previous section. The plots show four different lines where the solid line shows the results from HawC2 using the dynamic coupled NWM, the dot-dashed line gives the results of HawC2 without the NWM, meaning the results for the dot-dashed line show only the results from the BEM model in HawC2. In a similar manner, the dotted line gives the induction for the full coupled model and the dashed line shows the results for only the BEM code used to couple the NWM in the current work. Generally a good fit is seen for the two different models both with and without the coupled model.

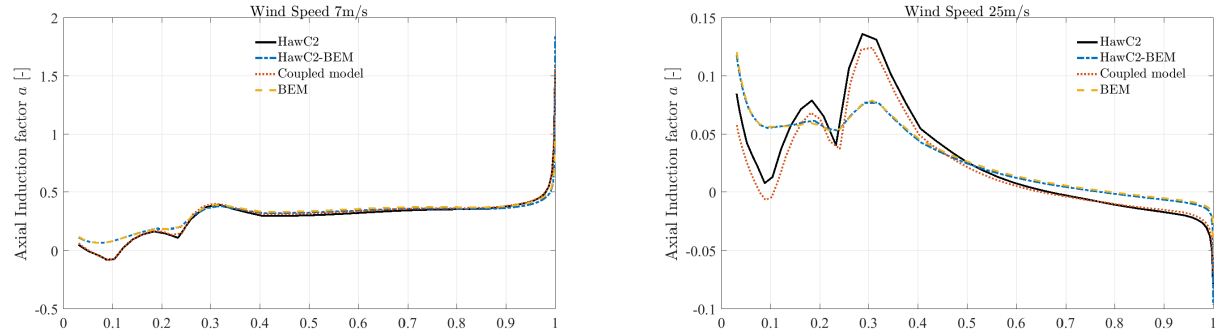

(a) 7 m/s (b) 25 m/s

Figure 5.11: Axial Induction factor comparison with HawC2 at 7 m/s and 25 m/s

Tangential Induction factors

Figure 5.12 shows the tangential induction factor plotted for both the models and here again it is seen that the tangential induction lies almost on top of each other for the entire blade span for all four methods compared here.

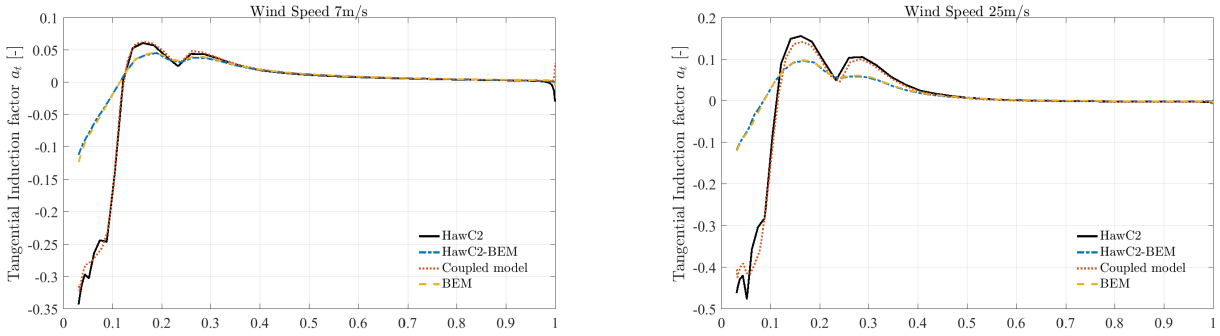

(a) 7 m/s (b) 25 m/s

Figure 5.12: Tangential Induction factor comparison with HawC2 at 7 m/s and 25 m/s

Out-of-plane loads

The out-of-plane loads for the wind speeds 7 m/s and 25 m/s are presented next and for the former case it is seen that the coupled model agrees very well with the results from HawC2. For the latter case of 25 m/s a small offset is seen between the two models both with and without the NWM coupling. However, the trend of the curve for the coupled model is the same as that of HawC2.

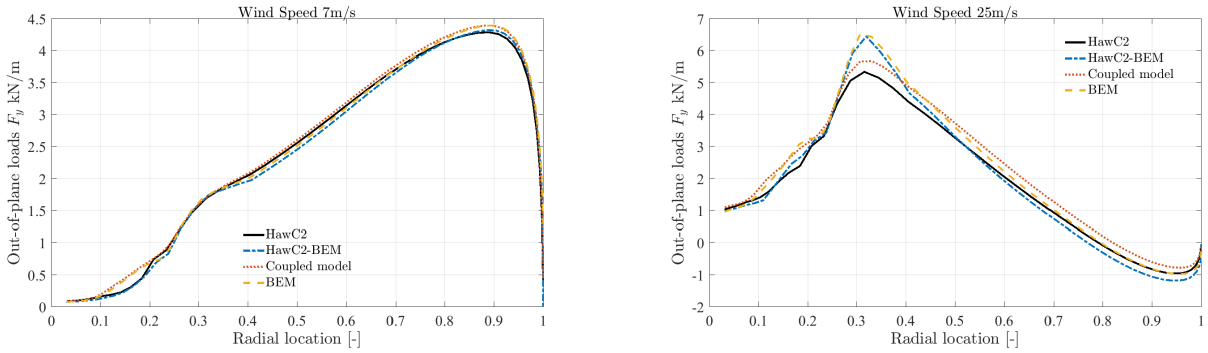

(a) 7 m/s (b) 25 m/s

Figure 5.13: Out-of-plane loads comparison with HawC2 at 7 m/s and 25 m/s

In-plane loads

Lastly, the in-plane loads are presented in Figures 5.14a and 5.14b where the same trend is seen as for the out-of-plane loads. The low wind speed case matches well and an offset is observed for the high wind speed case between HawC2 versus the coupled model, as well as HawC2-BEM versus the BEM model.

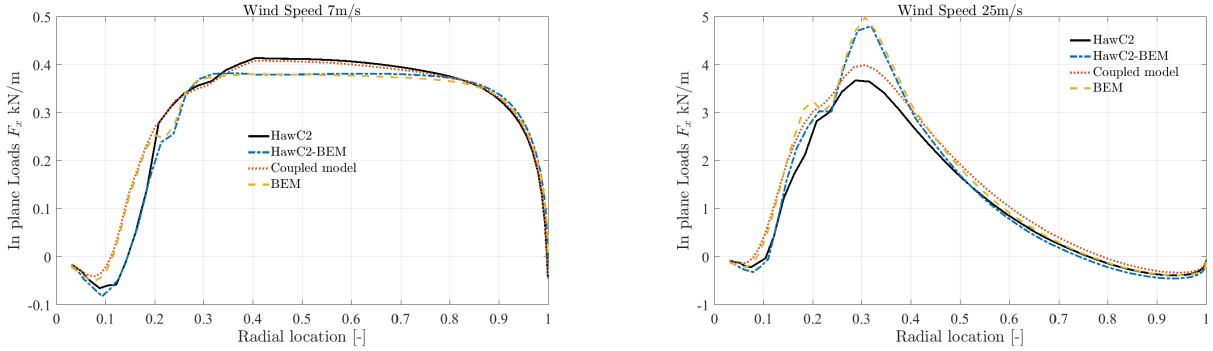

(a) 7 m/s (b) 25 m/s

Figure 5.14: In plane loads comparison with HawC2 at 7 m/s and 25 m/s

5.4 Effect of uneven loading on rotor induction

As described in Section 4.4 four different geometries are selected for testing the developed model for the case of uneven loaded blades. This section presents the results for these geometries. First the two geometries with the local chord increase between 60-75% blade span are presented. This is followed by the two slender blade geometries. The tangential inductions are again presented in the appendix.

Geometry *Local A* with maximum chord increase of 10%

Axial Induction factors

For the first local chord increase geometry, *Local A*, the axial induction factors are presented with the tip loss factor multiplied as before. The plot shows both the modified geometry as well as the plain DTU 10 MW RWT results for all three compared methods. The lines with the markers show the modified geometry results whereas the dashed and solid line shows the plain geometry. It is easy to see that the induction is higher as compared to the plain geometry in the region with the augmented chord. This increase is less appreciable for the high wind speed case. The CFD results for the unmodified and modified geometry are almost identical for most of the radius and only differ at the region where the geometry is modified. Further, this difference is even less evident for the high wind speed case.

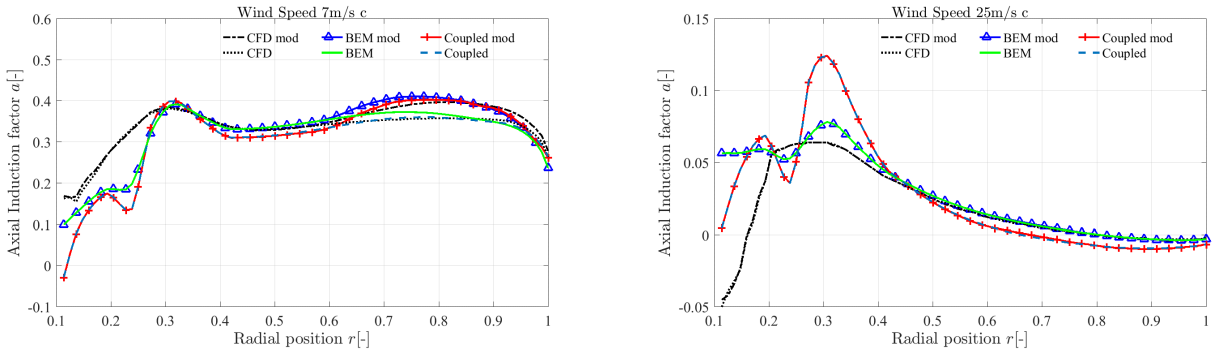

(a) 7 m/s

(b) 25 m/s

Figure 5.15: Axial induction factor comparison for geometry *Local A*

Out-of-plane loads

The out-of-plane loads are presented next and the plots follow the same scheme as described above. Generally a small difference can be observed between CFD and the aerodynamic models with the modified geometry, this difference was not that evident for the plain geometry case as can also be noted from the Figures 5.16a and 5.16b

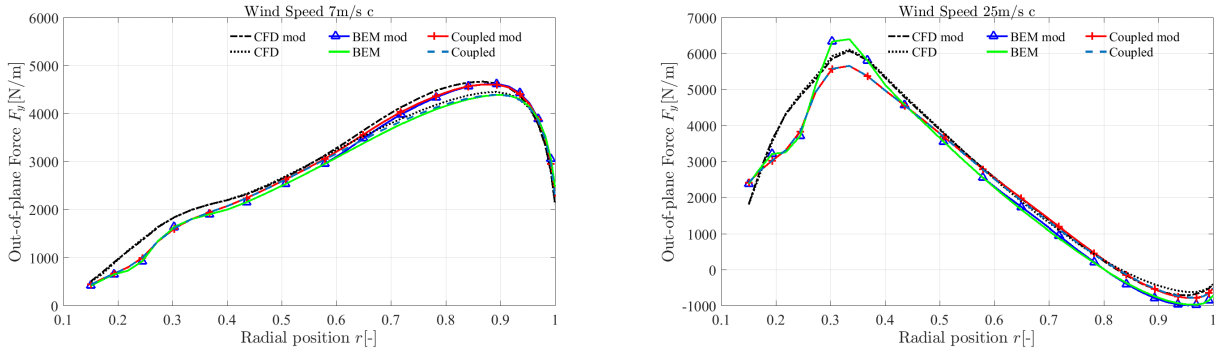

(a) 7 m/s (b) 25 m/s

Figure 5.16: Out-of-plane loads comparison for geometry *Local A*

In-plane loads

The in-plane loads presented in Figure 5.17 show that the BEM results are not significantly changed with the modified geometry. With the coupled model, it is seen that there is a drop in the in-plane force after about the radial location of 60%. A noticeable drop is also observed in the BEM results after 60% blade span.

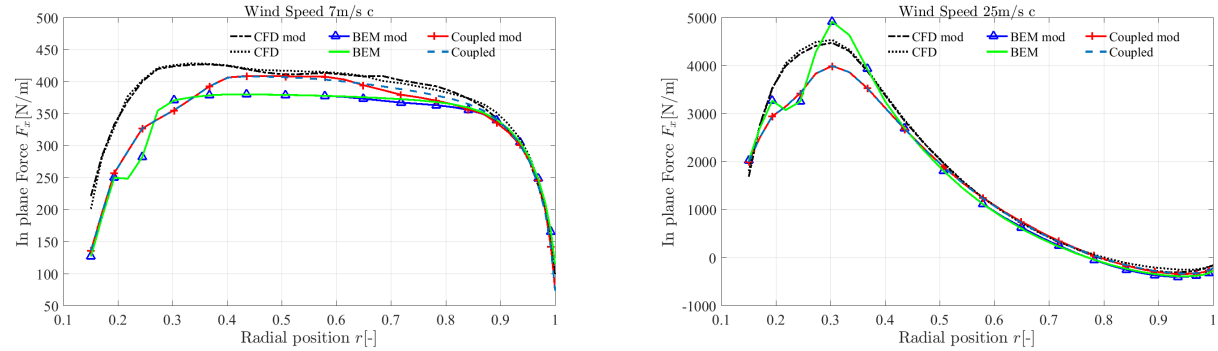

(a) 7 m/s (b) 25 m/s

Figure 5.17: In-plane loads comparison for geometry *Local A*

Geometry *Local B* with maximum chord increase of 20%

This section presents the results shown for the local chord increase of 20% in geometry *Local B*. The same trends are seen as for the *Local A* geometry but this time the effects and differences are slightly larger than for *Local A*. It should be noted that a chord increase of 20% is quite high but this case is tested as a special case to see how effective the different models are even for a potentially unrealistic chord distribution.

Axial Induction factors

The axial induction factor comparison shows a larger change in the induction for the larger local increase in the chord for all three models. This change is even noticeable for the high wind speed case after 60% blade span for the coupled model. No visible difference is seen in the BEM results for the modified and unmodified geometry at 25 m/s.

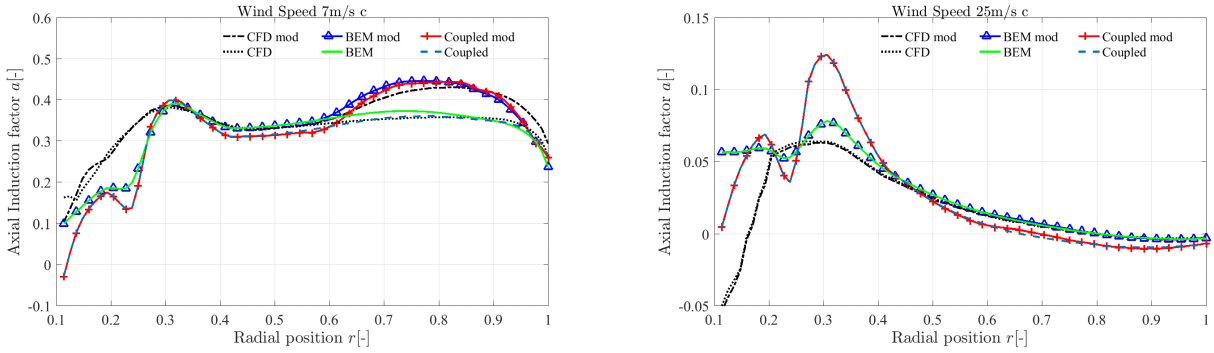

(a) 7 m/s (b) 25 m/s

Figure 5.18: Axial induction factor comparison for geometry *Local B*

Out-of-plane loads

The trends seen for the *Local A* geometry are seen for this geometry as well albeit these effects are more pronounced due to the larger chord increase.

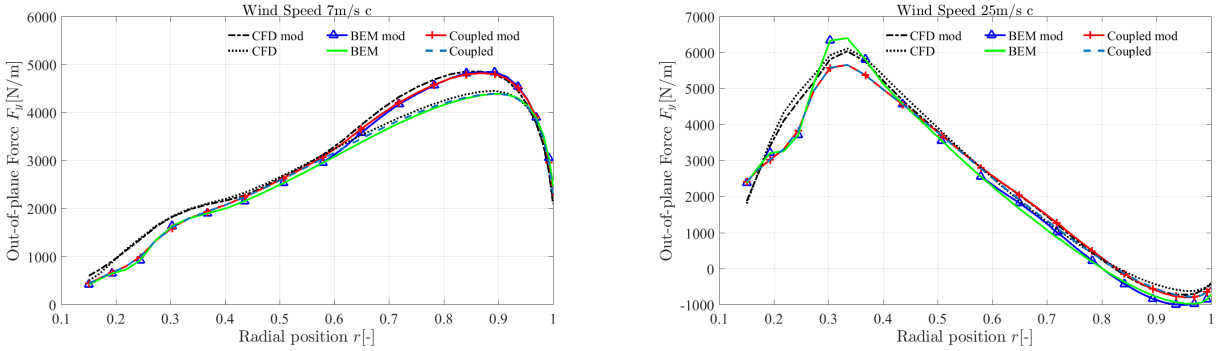

(a) 7 m/s (b) 25 m/s

Figure 5.19: Out-of-plane loads comparison for geometry *Local B*

In-plane loads

For the in-plane loads, a larger decrease is seen for both aerodynamic models in the region of the chord increase. Both models show a dip as compared to the unmodified geometry. The CFD curve on the other hand, comparatively sees a very slight increase in this region then subsequently drops to a lower value similar to the models at around 80% span.

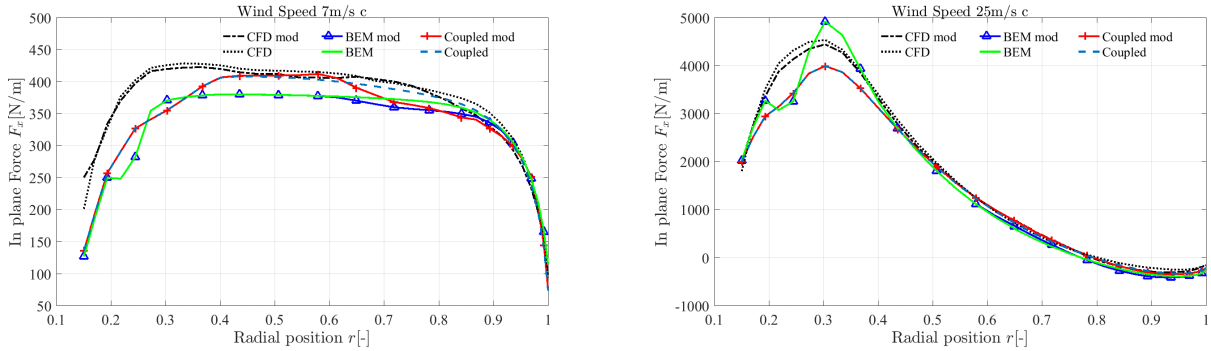

(a) 7 m/s (b) 25 m/s

Figure 5.20: In-plane loads comparison for geometry *Local B*

The next two sections present the results for the geometries with slender blades *Slender A* and *Slender B*

Slender A with max chord increase of 5%

Axial Induction factors

The slender geometries as explained before model a higher chord inboard and then a lower chord outboard than the reference rotor geometry. A maximum increase of 5% in the chord is applied at around 20% blade span for the geometry *Slender A* presented here. At the tip the chord is approximately 13% lower than the original blade. The first results plot the axial induction factor with the radial location in a non-dimensional manner. Aside from the tip, a good fit is seen between the model results for the modified geometry and the CFD results. At the tip, the CFD results show a slightly higher induction than the induction predicted by both the models.

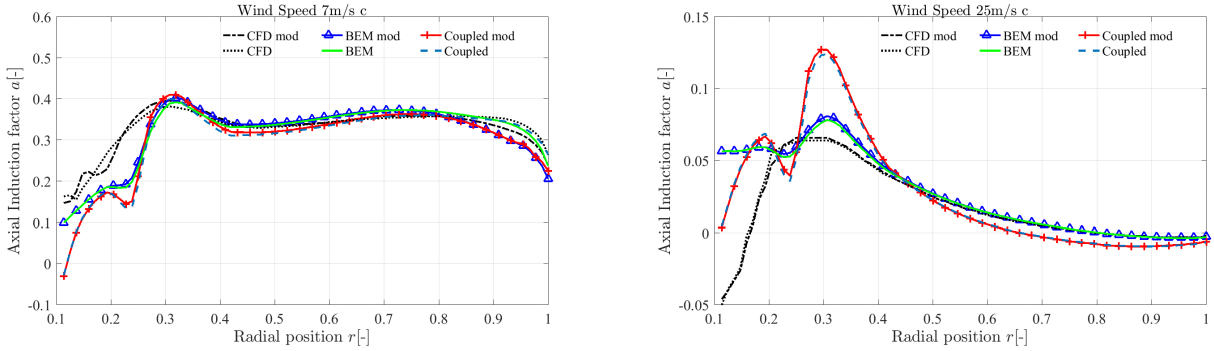

(a) 7 m/s (b) 25 m/s

Figure 5.21: Axial induction factor comparison for geometry *Slender A*

Out-of-plane loads

With the out-of-plane loads, the results from the modified geometry for the models and CFD match reasonably well and also at the tip here a good match is seen. This is true for both wind speeds.

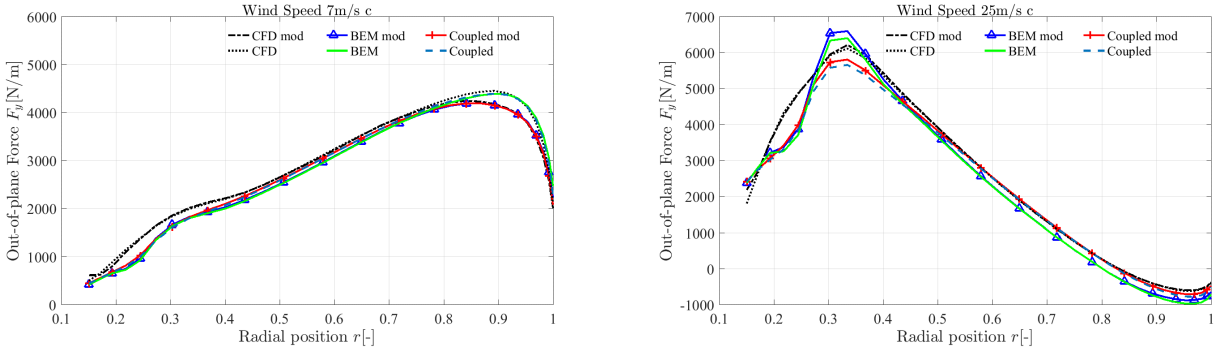

(a) 7 m/s (b) 25 m/s

Figure 5.22: Out-of-plane loads comparison for geometry *Slender A*

In-plane loads

Lastly, the in-plane loads plotted against the non dimensional radius show that like the even loading case, the in-plane forces with the BEM have a deficit compared to CFD where the coupled model does not and follows the CFD curve being slightly lower than CFD results.

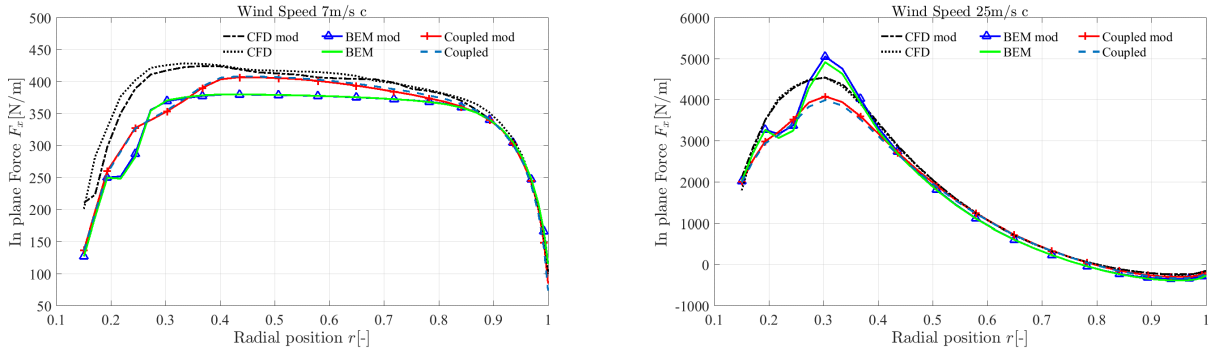

(a) 7 m/s (b) 25 m/s

Figure 5.23: In-plane loads comparison for geometry *Slender A*

Slender B with max chord increase of 10%

The last section in this chapter reveals the results for the geometry *Slender B* introduced in the previous chapter. The maximum chord increase for this geometry is 10% at the same radial location of 20% like *Slender A*. Similarly the maximum chord decrease from the reference geometry in this case is approximately 16% at the tip. The results are listed in the same order starting with axial induction factor, followed by the out of plane and in plane loads.

Axial Induction factors

The following plots show the results for both modified geometry, *Slender B*, and the plain geometry CFD results without coning. The axial induction factors plotted against the radial locations are given here after multiplication with the tip loss factor. For the low wind speed case all four lines are quite close to each other except at the tip. The difference between unmodified and modified geometry is seen to be small for the high wind speed case.

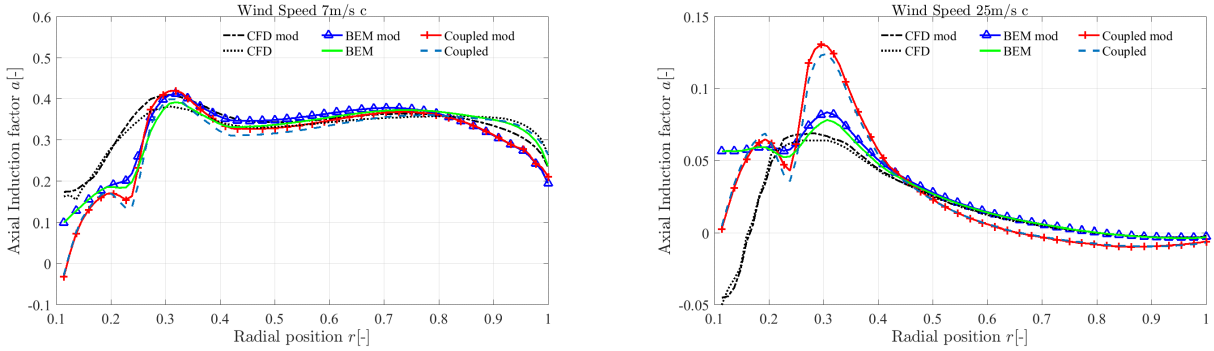

(a) 7 m/s (b) 25 m/s

Figure 5.24: Axial induction factor comparison for geometry *Slender B*

Out-of-plane loads

The out-of-plane loads presented in Figure 5.25a show the results for all three methods to be quite close to each other except for the root and a good fit is seen at the tip region as well. For the high wind speed case only a slight difference at the tips is seen with the modified geometry compared to the unmodified case.

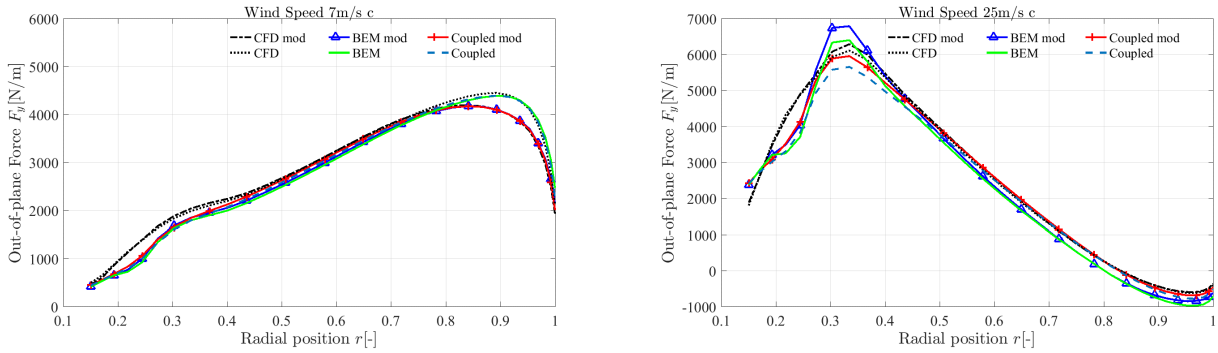

(a) 7 m/s (b) 25 m/s

Figure 5.25: Out-of-plane loads comparison for geometry *Slender B*

In-plane loads

Similar to the observations before, the deficit in the BEM results compared to CFD for the in-plane loads is seen again. The geometry *Slender B* results shown here also shows a familiar trend with all previous results at high wind speeds where the BEM slightly over-predicts the in-plane loads inboard and slightly under-predicts the loads outboard. The coupled model on the other hand underestimates the loads inboard but seems to lie almost on top of the CFD curve on the rest of the blade span.

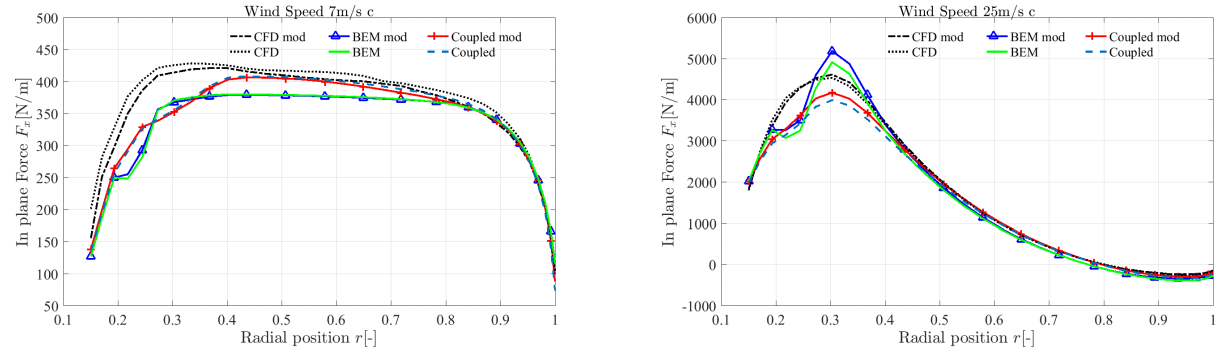

(a) 7 m/s (b) 25 m/s

Figure 5.26: In-plane loads comparison for geometry *Slender B*

Chapter 6

Discussion and commentary on results

This chapter contains the discussion and elaboration of the main findings and observations from the results presented in the previous chapter. The results are presented here in the form of delta plots describing the difference between the compared models when compared to CFD, or in the case of the modified geometries with the unmodified geometry as well. The discussion explains some of the effects seen in the results of the previous chapter. The first section presents the outcomes of the validation done with HawC2. This is followed by another validation comparison with EllipSys 3D CFD simulations. Next a brief comparison between the lift coefficeint from CFD and from the polars is presented. The discussion for the even and uneven load distribution simulations is then presented in the last two sections of this chapter.

6.1 Discussion of HawC2 comparison results

To legitimize the claims and findings of the current study, a reasonable method to validate the results is to compare the obtained results for the DTU 10 MW RWT with HawC2 [33]. HawC2 (**H**orizonatal **A**xis **W**ind turbine simulation **C**ode **2**nd generation) developed by DTU Wind Energy is a dynamic aeroelastic solver that models the aerodynamic and structural response of a wind turbine in the time domain. It is a very useful tool for wind turbine design and for load calculations carried out for certification purposes. The aeroelastic simulation code has been verified through extensive studies and measurements [39],[40],[41] over the years.

HawC2 employs the full near wake model in its dynamic form and therefore comparing steady or converged HawC2 simulation results for the DTU 10 MW RWT is a good reference to compare and validate the performance of the steady state NWM developed in this study. From the results presented in Section 5.3 the general outcome is that the current implementation gives results that are quite close to the results from HawC2 for both high tip speed ratio and thus high loading cases i.e. 7 m/s, as well as the high wind speed case for 25 m/s.

For the case of the axial inductions at 7 m/s it can be seen from Figure 5.11a that the induction given by HawC2 (solid line) lies almost on top of the induction from the coupled model in this study. The same is observed for the HawC2-BEM results when compared to the BEM model used in the current study. Given that the HawC2 uses the coupled model, it is within expectations that the steady state implementation matches with HawC2. There is a slight difference seen in the inductions given by HawC2 and the coupled model for the high wind speed case of 25 m/s. However, the general trend is seen to be the same for both implementations of the near wake model. The HawC2-BEM results given in the Figure 5.11b as the dashed line also agrees with the BEM used in the current study represented with the yellow dashed line. Here also a marginal difference is seen between the two BEM models. The tangential inductions obtained from all four models are more or less the same for almost the entire blade except for the root section where the results are unreliable because of the much thicker airfoils used in this region. This is seen for both the wind speeds.

For the case of the loads, it is seen from Figures 5.13a and 5.14a that the results from the coupled model fit very well with the results from HawC2 for both in plane and out of plane loads in the case of 7 m/s. Near the tip a slight disparity is seen between the two models but this disparity is observed even in the case of the plain BEM results from HawC2 and the code developed in this study. In the case of the high wind speed, it is seen that there is an almost

constant offset between the coupled model and HawC2 from 30% of the blade span onwards for both in plane and out of plain loads. To investigate the potential reasons behind this and the small disparity for the low wind speed as well, the angle of attack and the lift coefficient are plotted as shown in Figures 6.1 and 6.2.

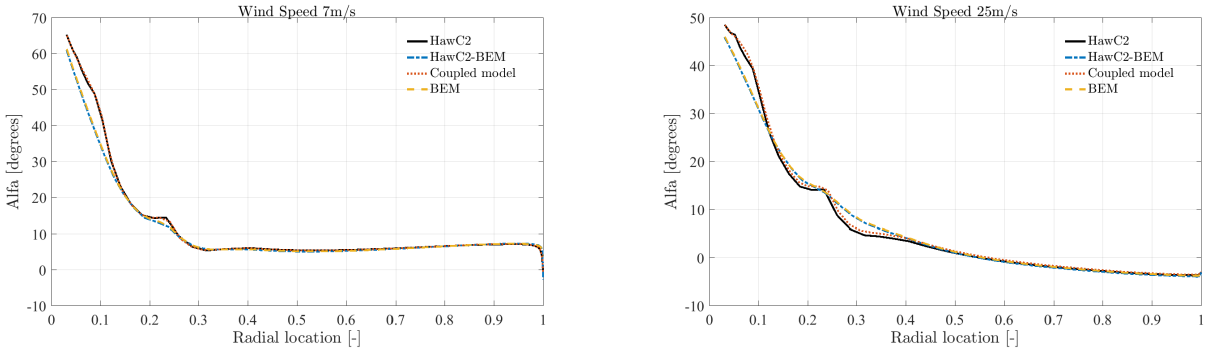

(a) 7 m/s (b) 25 m/s

Figure 6.1: Angle of attack comparison with HawC2 at 7 m/s and 25 m/s

From the two figures for the angle of attack it is immediately highlighted that the angle of attack fits slightly better between HawC2 and the coupled model for the low wind speed case while there is a small but noticeable difference for 25 m/s. In the case of the lift coefficient curves, it is seen that the roughly 1-2 degree discrepancy in the angle of attack seen in Figure 6.1b translates into a larger difference between the coupled model and HawC2 in the lift coefficient for the high wind speed case. In addition to this difference that is seen here it can again be appreciated that the BEM model for HawC2 and the BEM model underlying in the coupled model are again at a slight offset for the entire blade span.This difference is seen even in the 7 m/s case in the root sections before 30% for both angle of attack and lift coefficient in Figures 6.1a and 6.2a.

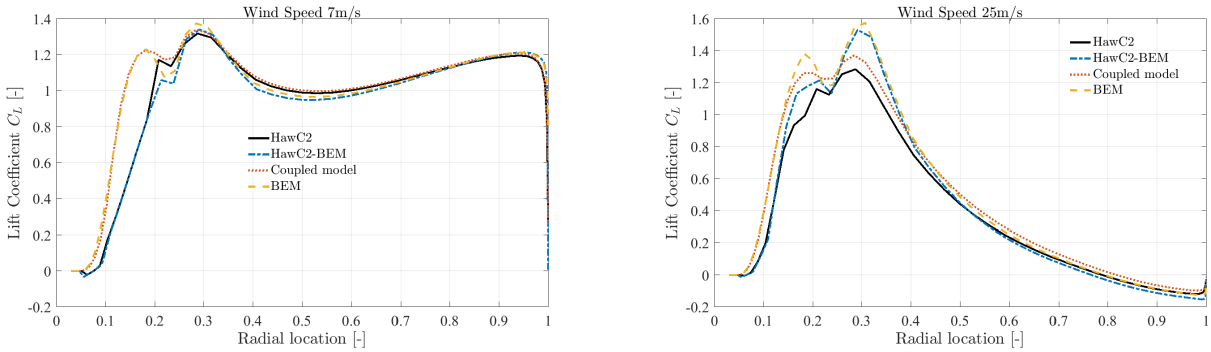

(a) 7 m/s (b) 25 m/s

Figure 6.2: Lift coefficient comparison with HawC2 at 7 m/s and 25 m/s

The difference between HawC2 and the coupled model for the higher wind speed is attributed greatly to the difference between the underlying BEM models that have been coupled with the near wake model for both the compared codes. This difference most likely arises due to the difference in the computation of the coupling factor between HawC2 and the coupled model developed here. In Section 3.4.2, it was established that the coupling factor is calculated based on the reduced thrust coefficient and a reference BEM induction calculation. This means that the coupling factor is heavily based on the BEM code used for this reference calculation, as well as the polynomial expression that relates the a to the differential thrust coefficient in the BEM code. HawC2 uses a different polynomial expression [42] to describe the thrust as a function of the axial induction a as compared to the BEM used in this study. This causes

some changes in the coupling factor that is then applied on each section of the blade. This is probably the reason behind the constant offset in the lift coefficient (see Figure 6.2) and hence the final aerodynamic loads at the higher wind speed as well as the discrepancy that is seen at the sections close to the root. In addition to this larger factor, the absence of dynamic effects in the developed coupled model also leads to minor differences between the two methods.

6.2 Comparison of NWM with Ellipsys CFD results for the DTU 10 MW RWT

In addition to comparison with HawC2, the results from the NWM and the CFD simulations in the current study are also compared with Ellipsys 3D CFD simulations for the DTU 10 MW turbine. EllipSys is a general purpose solver for the incompressible Navier-Stokes equations. It is a CFD code that is used for 2D CFD simulations to generate and validate airfoil designs as well as airfoil polars. As mentioned before the airfoil polars used in this study for the DTU 10 MW RWT are also generated using EllipSys 2D simulations. It is also used for full rotor 3D CFD simulations where the entire rotor geometry is modeled.

The comparison presented here shows results for a non-deformed straight rotor. The flow conditions modeled here for both the CFD results are laminar with free transition to turbulent flow. However it should be mentioned that both use different Turbulence Intensity (TI) levels to model transition. Where the TI for the EllipSys results is 10% and is much higher than the almost negligible value used in the CFD simulations that are carried to give the results presented so far. An operating point from Table 4.2 is chosen for the comparison namely 10 m/s. Only the loads are compared here since these are a direct output of the simulations and therefore more reliable quantities for comparison. The out-of-plane and in-plane loads for this comparison are shown in Figure 6.3

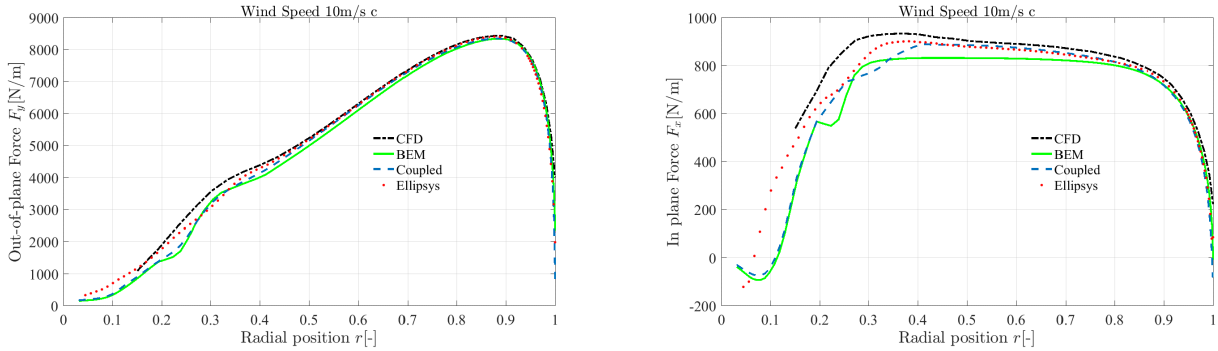

(a) Out-of-plane

(b) In-plane

Figure 6.3: Aerodynamic loads presented for the four compared methods at 10 m/s

For both types of loads it is seen that the dotted line representing the EllipSys results is almost identical to the coupled model, barring the inboard sections before 30% of the blade span. This further validates the performance of the coupled model. An additional observation from the EllipSys 3D results can be made when the same loads are plotted for a fully turbulent flow comparison. The results are plotted in Figure 6.4. From these results the difference in the TI levels used for both type of CFD simulations can be appreciated. If the laminar flow results in Figure 6.3 are compared to the turbulent ones, it can be seen that the EllipSys results change marginally when going from laminar to turbulent while the CFD results see quite a decrease in value comparatively. It should also be kept in mind that the model results do not change since they use the same polars in both comparisons. It can be seen that the EllipSys loads reduce only in the root section and are largely unchanged for the rest of the blade in the turbulent comparison whereas the CFD results see a drop throughout the blade because of the higher turbulence in the flow.

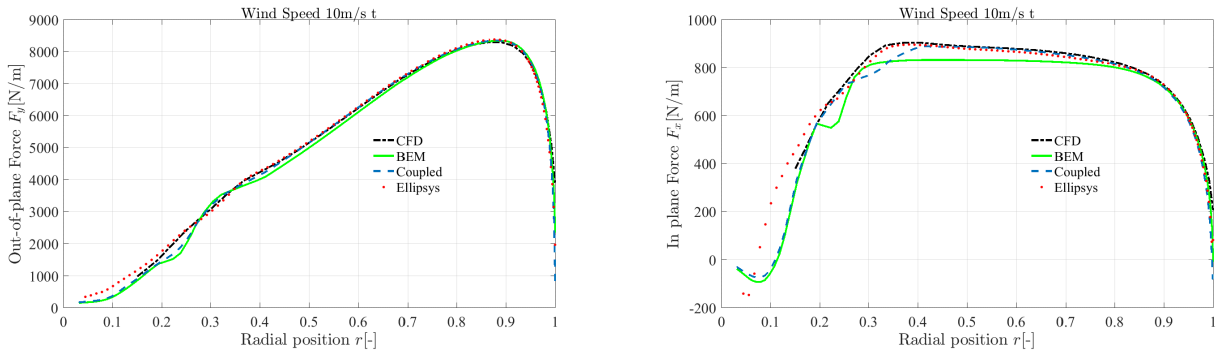

(a) Out-of-plane

(b) In-plane

Figure 6.4: Aerodynamic loads presented for the four compared methods at 10 m/s for fully turbulent flow

The discussion above indicates that the EllipSys CFD results for the free transition case may actually be quite turbulent as compared to the CFD laminar results shown in this report. Since the airfoil polars used for both the aerodynamic models are also generated using EllipSys CFD laminar flow results with the same TI settings, this potentially means that the polars may include greater turbulence effects as well. This is another reason for conducting an analysis of the model results with turbulent flow conditions in CFD and the results of this are presented in the Appendix A.

6.3 Comparison of CFD operating points and Airfoil polars

The BEM model and coupled model both rely on the airfoil polars to estimate the lift and drag forces at the airfoil sections which are then translated into the normal and tangential loads acting on the rotor. The fact that the airfoil polars play an important role in the determination of aerodynamic loads means that uncertainty in the polars can lead to undesired inaccuracies in the performance of the BEM and the coupled model. To this effect, it is interesting to investigate the agreement between the lift coefficient predicted by the CFD simulations with the lift coefficient that is estimated by the airfoil polars. Such an analysis clarifies the difference between the prediction by CFD and by the models from a polar perspective thus clarifying how much of the difference is dependent on the uncertainty of the polars.

The CFD lift prediction is compared by plotting different operating points on the lift curves from the polars. This is done by considering specific radial locations along the blade. Those radial locations are selected which have an airfoil thickness to chord ratio that is equal or close to the compared polar. In this analysis the two thinner airfoils with 24.1 and 30.1 $\%t/c$ are chosen as a wide range of the blade has airfoils with relative thickness around these values as can also be seen in Figure 4.1. CFD simulation results for different wind speeds are selected and the coefficient of lift and angle of attack as estimated by CFD at the radial locations for the different wind speeds is chosen as a set of operating points. These operating points are then plotted along the lift versus angle of attack curve from the polars to compare the C_L estimates from the different methods. The radial locations and relative thicknesses of the selected points are listed in Table 6.1.

Table 6.1: Radial locations and corresponding airfoil thickness chosen for comparison

Airfoil polar [t/c%]	**Chosen Radial Locations** [m]	**Relative thickness of airfoil at radial location** [%]
24.1	69.3 , 72.0 , 74.7	24.1, 24.1, 24.1
30.1	38.6	29

The outboard part of the DTU 10 MW RWT from roughly 60 m onwards has a fixed t/c of 24.1% which makes selection of radial locations easy for this airfoil comparison. Three different airfoil sections are selected in the outer part of the blade, all of which have the exact t/c as the available airfoil polar. For the 30.1% thick airfoil, selection of

points is not so straightforward as this airfoil is never exactly used but airfoils close to this t/c are used between 35 to 40 m of the blade span (see Figure 4.1). The closest point to the 30.1% airfoil is then selected which is an airfoil section having a t/c of 29%.

With the airfoil sections selected, CFD simulations for the evenly loaded unmodified rotor are used to derive operating points. Different wind speeds as well as the differences in twist and induction at the different radial locations gives a range of operating points from the CFD simulations. The lift and angle of attack points at the radial locations for the different wind speeds are then plotted on the original polars in Figure 6.5. For the case of the 30% airfoil only one radial location is chosen but the range of wind speeds still gives a spread set of points in the linear section of the lift curve.

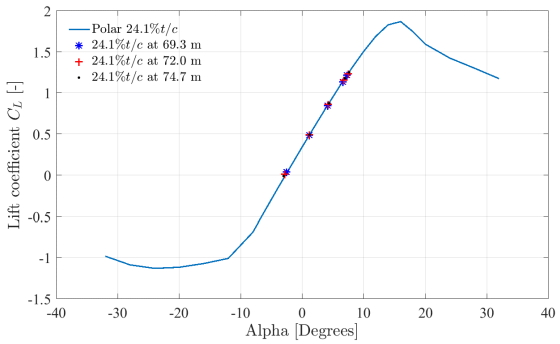

(a) Airfoil with $t/c = 24.1\%$

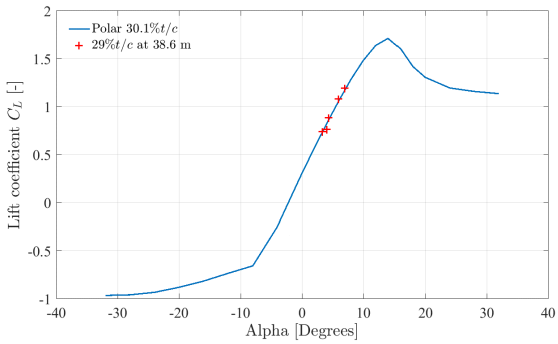

(b) Airfoil with $t/c = 30.1\%$

Figure 6.5: Comparison between CFD operating points for Lift and airfoil polars, the different markers show the Lift coefficients predicted by the CFD simulations for different radial locations along the blade

From both Figures 6.5a and 6.5b it is seen that the lift coefficient calculated by CFD is lying almost on top of the lift curve of the polars that is used by the models, the points are very marginally off for the thicker airfoil but this is also because there is a slight difference in thickness in this case. This result shows that all three methods give lift values which are very close to each other. This means that the uncertainty and difference between the models and CFD due to the polars is rather small at least for the airfoils which span a large section of the blade from roughly 30% of the span onwards. Due to this, the effect of the polars on the end results can be isolated to not create further uncertainties as both BEM and coupled model use exactly the same polars which also give similar lift coefficients as seen by CFD.

6.4 Performance of NWM as compared to the original BEM model for plain rotor

With the results presented in Section 5.2, for two rotor configurations of the plain DTU 10 MW RWT, this section discusses the important findings from the results for both coning and no coning results.

6.4.1 Rotor with coning

The axial induction plots shown in Figure 5.3, show that the induction with the near wake coupled model resembles the induction obtained through CFD better from almost 40% of the blade to outboard locations. At the tip sections, the results from both the coupled model and the standard BEM diverge to higher values as opposed to the induction from the CFD results which decreases.

The reason for this deviation lies in the induction calculation method from CFD. For one thing, the averaging method described in Section 4.3 only gives the global induction on the rotor because of the way the inductions are averaged over annular arcs. Recalling the discussion on the induction calculation from CFD in Section 4.3, it was

described that there is a distinction between local and global induction for rotors with finite number of blades i.e. real wind turbines. This global induction is very different from the local induction in regions of trailed vorticity such as the root and the tip. The model results show the local inductions where CFD only describes the global induction. This means that the effect of the root and tip vortex, which increase the induction locally, is not easy to see from the CFD inductions. Secondly, the induction is not a direct and straightforward quantity to obtain from post processing of CFD simulations, making it difficult to get a reliable estimate of the induction anyways.

In addressing the difference between local and global induction, some authors such as Shen et al. [37] suggest that the relation between the local and global induction from the BEM can be theoretically expressed as the reciprocal of the tip loss factor. Thus, one way to compare the inductions to CFD results is to multiply the BEM and coupled model results with the tip loss factor. The tip loss factor corrects for the effect of the tip vortex which is not considered in the standard BEM because of the actuator disc assumption. Since the difference in global and local induction at the tip is due to the tip vortex, by multiplying the tip loss factor, some of this difference is corrected. The result is that the inductions after multiplication with F match quite well at the wind speed cases of 7 or 10 m/s. Both wind speeds show that the coupled model slightly outperforms the plain BEM model except for the tip regions where the BEM is marginally closer to the CFD results.

The trend is better seen with the help of the delta plot shown in Figure 6.6 where the CFD results are presented as a baseline and are indicated by the dashed line lying at 0. The absolute difference between the CFD results and aerodynamic models is presented for both wind speeds in Figure 6.6, where the CFD results are subtracted from the model results. For a large section of the blade the coupled BEM model gives a lower difference from CFD as compared to the original model for both wind speeds. The curves for both BEM and coupled model however follow a similar trend and this is due to the fact that the coupled model enhances or improves the induction from the BEM by adding the vorticity effects.

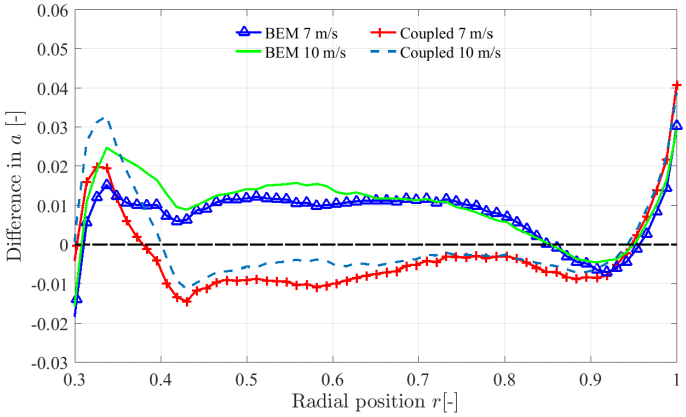

Figure 6.6: Difference in axial induction at 7 m/s and 10 m/s with tip loss factor multiplied

For the tangential inductions shown in Figure 5.5, all three models give almost identical results except for the root sections. Even though the curves for all three methods lie almost on top of each other, the absolute deltas are plotted and presented here for this first case. The differences for both models with CFD are only marginal and this is also difficult to highlight due to the scale of the tangential induction factor being very small to begin with. Further, it is likely that since the calculation of the tangential induction involves using the axial induction itself, the eventual added effect because of the coupled axial induction is small in the tangential induction.

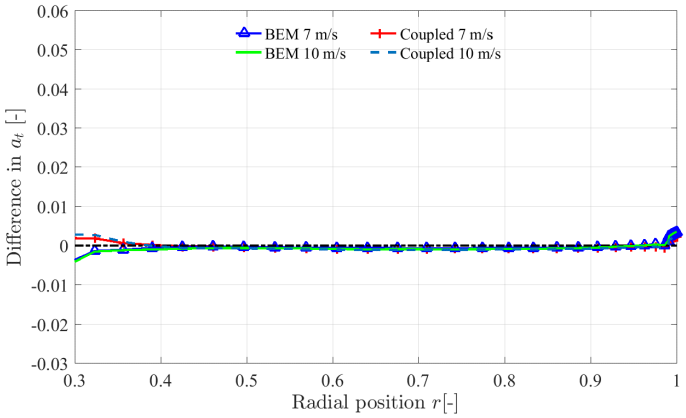

Figure 6.7: Difference in tangential induction at 7 m/s and 10 m/s

The out of plane loads for the case with a coning angle both showed in Figures 5.6a and 5.6b that the coupled model slightly overestimated the loads from CFD and BEM appears to be closer in this case. The overestimation is quantified with the help of difference plots in Figure 6.8 with CFD acting as the baseline for the comparison as in the case of the previous results. The coupled model only works better than the standard BEM in the mid-span locations.

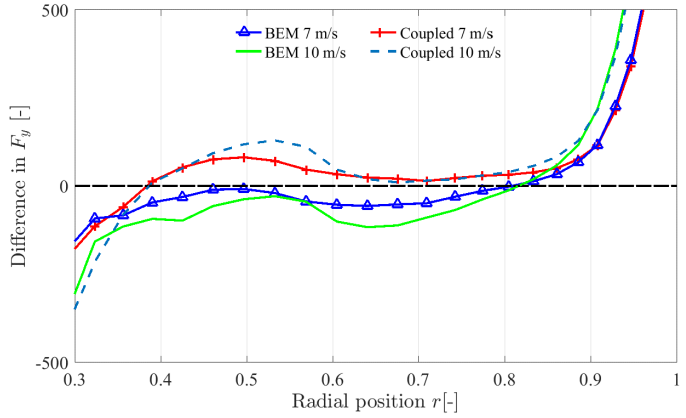

Figure 6.8: Difference in out-of-plane loads at 7 m/s and 10 m/s

It is seen that at the tip, the results from the models diverge from the CFD results since a coning angle is not resolved by the models and the loads from the models are higher than CFD. The CFD shows lower loads at the tip because of the rotor coning. The rotor is coned to achieve centrifugal relief which counteracts the higher out-of-plane loads due to the thrust loading which is also represented by the lower loads seen by CFD. To round off this section, the results from the in-plane loads also represent the disparity at the tip due to the influence of the coning angle where the models diverge. Accompanying this is the delta plot for this case.

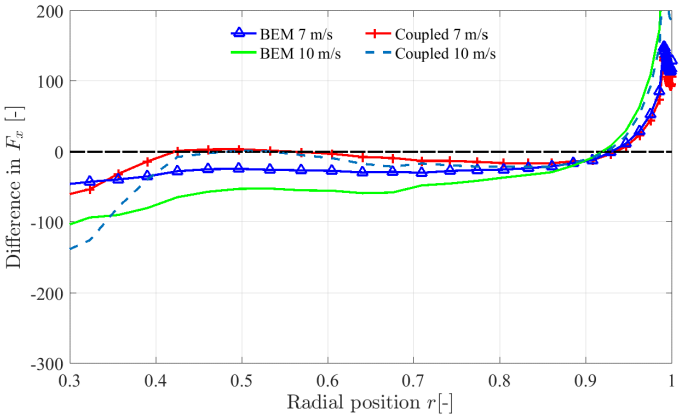

Figure 6.9: Difference in in-plane loads at 7 m/s and 10 m/s

6.4.2 Rotor without coning

The coning rotor CFD results presented in the previous chapter were followed by a comparison of the aerodynamic models against CFD simulations where an undeformed rotor was modeled with zero coning angle. The results from the models in this case were closer to the CFD calculations and this reconciled some of the effects and discrepancies seen in the previous section. Furthermore it was generally seen that the coupled model is more accurate as compared to the BEM model for most results.

This set of results also introduced a high wind speed for comparison and here it is seen from Figure 5.8b that the coupled model gives a much larger induction in the root sections as compared to both the standard BEM and the CFD. This large increase in the induction is due to the presence of the root vortex whose effect becomes more significant at this high wind speed and low loading case. For reasons explained previously with regards to the induction calculation in CFD, this increase in induction due to the presence of the root vortex is not captured by the averaging method discussed in Section 4.3 as local changes in induction are not seen in the global inductions from CFD.

In the previous section at the lower wind speeds, multiplication by the tip loss factor resolved some of the difference between the local and global induction seen at the tips due to the tip vortex. The results presented in Section 5.2.2 already show the inductions multiplied with the tip loss factor. While the lower wind speed of 7 m/s shows good agreement with both the models and CFD after multiplying with F, the higher wind speed still has a difference in the inductions between the coupled model and CFD particularly at the root as is seen in the Figure 5.8.

The reason for this can be explained in the following way: at the low wind speed the dominating effect of the tip vortex causes a difference between the two types of inductions and the effect is compensated somewhat by multiplying the local inductions with the tip loss factor. At the higher wind speed however, the load distribution is very different from the low wind speed case. Because the high loading at high wind speed is inboard and not at the tip, the BEM tip loss correction does not really correct the results in the same way as the low wind speed case. The tip vortex at high wind is not the same as it is seen at low wind, therefore the tip loss correction does not have the desired effect of completely bridging the gap between the local and global induction. A small improvement at the tip is still seen for both the BEM and the coupled model after multiplication by F (see Appendix B where the high wind speed results are shown both before and after multiplying with F). However, the dominating effect in this case is the root vortex which is not compensated simply by multiplying the local inductions from the models with the tip loss factor. This is the reason that the large difference in the root section is still seen between the coupled model and CFD.

It is also noteworthy that since there is no trailed vorticity modeling in the standard BEM, the BEM results only see a small impact of the root vortex in the induction distribution and the coupled model sees a larger impact of the root vortex. However, as shown in the HawC2 comparison with Figure 5.11b, the effect seen by the NWM coupled model is well within expectations and is also realistic considering the physical presence of the root vortex. The induction from the coupled model on the outboard sections is slightly lower than the BEM results which in a way compensates for the higher induction inboard.

The delta plot for these results in Figure 6.10 shows that for the low wind speed and thus high tip speed ratio or high loading case, the induction from the coupled model is on average better for a greater part of the blade span. This improvement is due to the near wake effects that are added to the flow physics and thus the interdependence of the annuli is better resolved than the standard BEM. For the 25 m/s case, as explained the induction from the coupled model has a larger absolute difference from CFD.

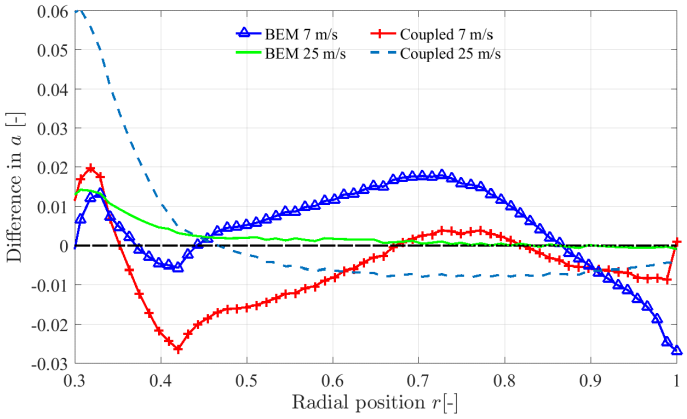

Figure 6.10: Difference in axial induction at 7 m/s and 25 m/s with tip loss factor multiplied for rotor without coning

The loads in the out-of-plane direction indicate that the coupled model has a slightly better performance for the low wind speed and a larger improvement on the standard BEM for the high wind speed. This indicates that the axial induction estimated with the coupled model is more realistic as compared to BEM as the eventual loads are much better approximated with the addition of the near wake vorticity. Even with the consistent difference with CFD at high wind speeds, it is seen that the loads for the coupled model are much closer to the baseline of CFD as opposed to the BEM.

The delta plot for the out-of-plane loads shown in Figure 6.11 confirms this and shows that even at the tip after around 90% of the blade span where both models cross the CFD loads, the coupled model is closer to the CFD estimates. While for the 7 m/s case it is seen that the BEM model itself is reasonably close to CFD, the 25 m/s case shows a significant improvement in the out-of-plane loads with the coupled model. This is because at high wind speeds the rotor is at a lower tip speed ratio meaning the helix angles in the trailed vorticity are larger and the rotor behaves less like a disc. Since the BEM is formulated on the actuator disc assumption, a larger difference is seen in the BEM results at lower tip speed ratios and high wind speeds since it is not so accurate when the rotor is far from a disc.

Additionally, the fact that the rotor behaves less like a disc at higher wind speeds also means that the induction estimation method from CFD performs worse than the low wind speed cases. Thus the inductions at the blades (which are responsible for the loads) are more different than the average induction on the disc compared to the low wind speeds as was seen in the delta plot for the inductions in Figure 6.10

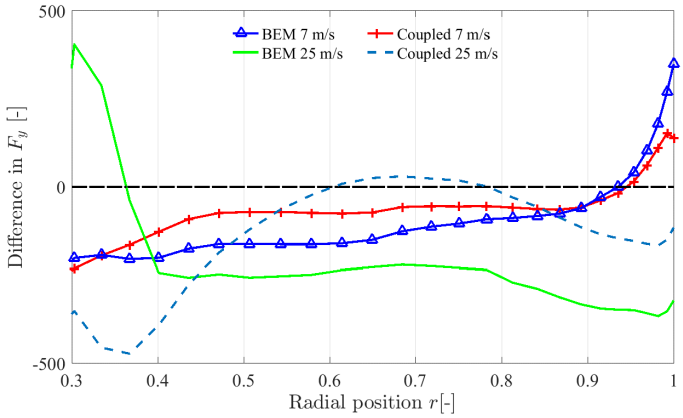

Figure 6.11: Difference in out-of-plane loads at 7 m/s and 25 m/s for rotor without coning

Figure 5.10 in the previous chapter, shows that the in-plane loads are significantly improved with the coupled model, where the BEM results had a constant deficit as compared to CFD. The coupled model follows the CFD curve quite well in the midspan regions. The added flow physics because of the trailed vorticity contribute to the improvements in the results as well as the interaction from the neighboring annuli. An interesting observation to note is that the loads at the tip both in the case of in-plane and out-of-plane directions are significantly improved as compared to the case with coning where the difference seen in the previous section was because of the coning angle. The difference between the aerodynamic models and the CFD results is expressed in absolute value in Figure 6.12.

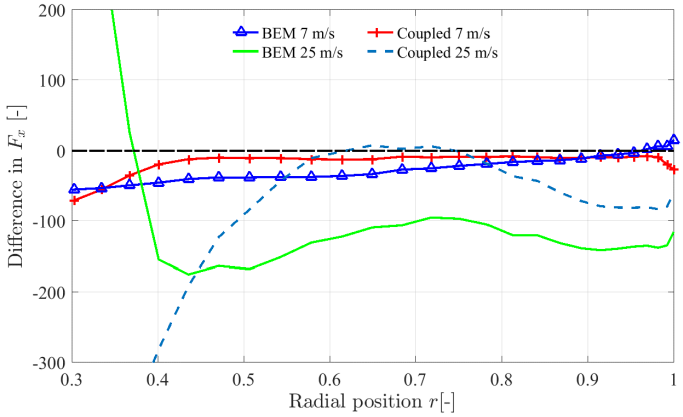

Figure 6.12: Difference in in-plane loads at 7 m/s and 25 m/s for rotor without coning

Another observation from the out-of-plane and in-plane loads at high wind speeds can be linked back to the higher local induction seen in the root sections by the coupled model. It is seen from Figures 5.9b and 5.10b that the loads at the root are much higher for BEM as compared to the coupled model. This is because the standard BEM does not capture the root vortex effect that can be seen in the local inductions from the coupled model. The higher local induction seen by the coupled model compared to the rotor plane average induction causes a lower load in the root section for the high wind speeds.

A general remark which holds true for all cases that are presented is that the root sections below 30% of the blade span show quite some difference between the models and CFD for inductions as well as loads. Even the tangential inductions are seen to be different in this region from Figure 5.5. This is a consequence of the reliance of the aerodynamic models on airfoil polars and polar data. Particularly in this case for the DTU 10MW rotor, the DU series airfoils used in the root section up until this point are very thick airfoils having thickness to chord ratios of around

60 and 48% or higher. As mentioned before, the airfoil polars for the 48 and 60% airfoils are simply obtained via interpolation between the available airfoils and a cylindrical cross section. This leads to some reservations towards the accuracy of these polars and how well they model reality. Another reason for disparity in the root sections is that the convergence criteria of the CFD simulations does not take the root convergence into consideration explicitly which also adds to the unreliability of the comparison in this region. This is also the reason why the delta plots are shown from only 30% of the blade onwards.

6.5 Performance with uneven load distribution and change in induction

The aim of the uneven distribution analysis is to test whether the NWM improves the discrepancies seen by a standard BEM code in the case of blades without an even load distribution. This can involve blades having increased chords which would result in an uneven loading or blades with large values of chord inboard and small values of the chord outboard. These are the geometries which are selected for the analysis in the current study. In addition to this, this section also shows results for a more abrupt change in the induction.

6.5.1 Local chord increase geometries

Circulation Distributions

The first thing to ensure that the required unevenness is being achieved with the geometries tested in this study is to observe if the augmented geometry changes the circulation distribution along the blade. For this purpose, the results from the model for the calculated circulation are presented first in the discussion section to corroborate this. From Figures 6.13 and 6.14 it is seen that the modified geometry has a higher circulation distribution than the plain one as was expected. However, it is noteworthy that the increase in the circulation is perhaps too smooth to mimic a sudden change in the induction distribution. Nevertheless, for ease of CFD convergence, this type of geometry augmentation is quite feasible. Also it is seen that the circulation has a much smaller change for the modified geometry in the case of the high wind speed. At high wind speeds, the blade is pitched out to create a loss of lift and reduce loads, because of this the impact of the increased chord is not that effective and the circulation distribution is not significantly affected.

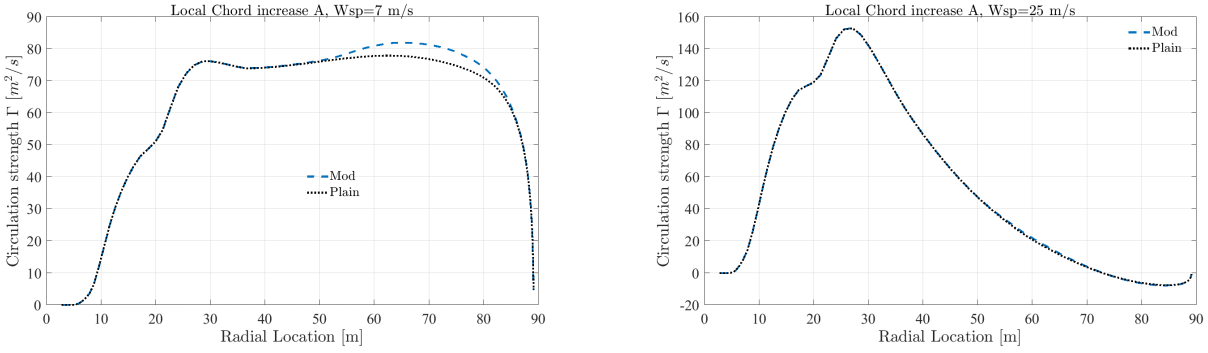

(a) 7 m/s

(b) 25 m/s

Figure 6.13: Circulation distribution for plain and modified geometry *Local A* at 7 m/s and 25 m/s

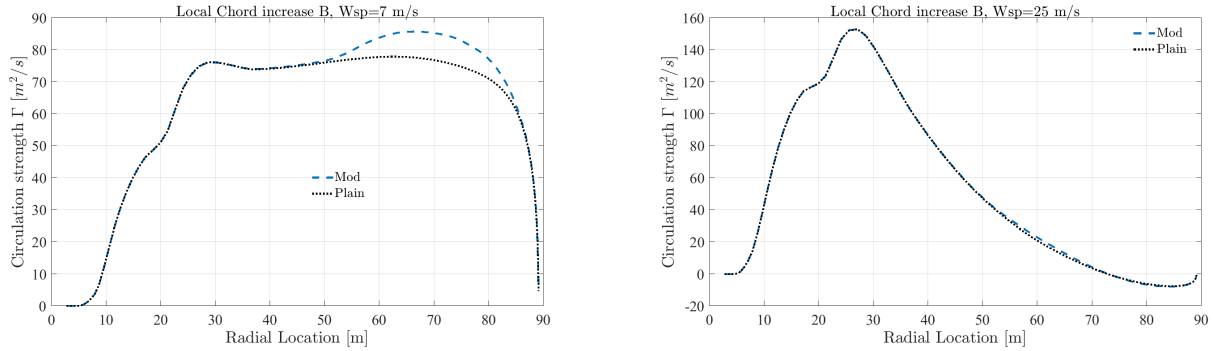

(a) 7 m/s (b) 25 m/s

Figure 6.14: Circulation distribution for plain and modified geometry *Local B* at 7 m/s and 25 m/s

Delta plots with CFD

Next, the difference for the aerodynamic models compared to the CFD results for that geometry as a baseline are presented in Figure 6.15. It should be noted that both geometries are compared to their own respective CFD simulation results which lie on the 0 or reference line in this plot. The two different set of induction lines corresponding to the different rotor geometries are thus obtained after subtracting the corresponding CFD inductions for the geometry being considered. The line with the open triangles corresponds to the difference between BEM and CFD for the modified geometry, while the line with the plus signs shows the difference between NWM and CFD for the modified geometry. Similarly, the solid line gives the difference between the BEM induction and CFD induction for the evenly loaded rotor or unmodified geometry, while the dashed line gives the same for the coupled model. The same scheme is followed for the rest of the delta plots shown in this section.

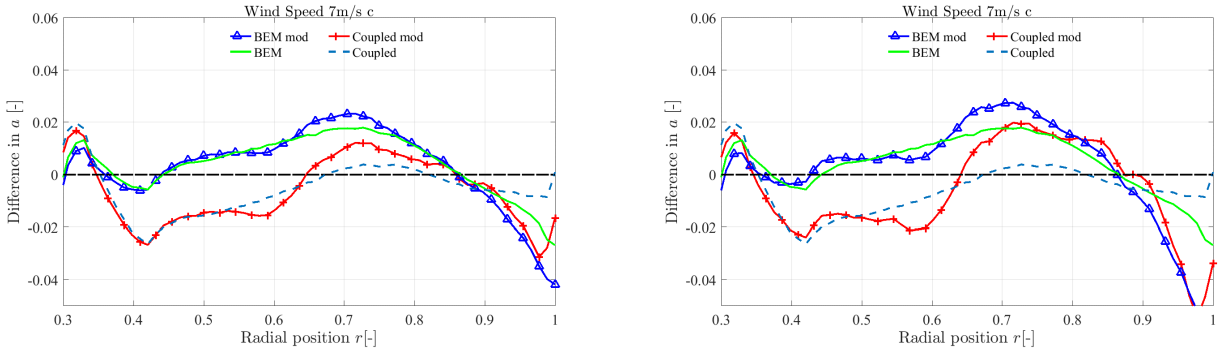

(a) Local A (b) Local B

Figure 6.15: Axial induction factor comparison for geometries *Local A* and *Local B* at 7 m/s

Two major observations of the delta plots for the induction results at the low wind speed include that the difference between the models and CFD is larger for the geometry Local B because of the larger local chord linked with it. The second observation is that both the models diverge from the CFD results with this divergence being more significant in the case of the BEM model. Looking at the dashed line for the unmodified rotor with coupled NWM model in Figure 6.15, it can be seen that for a rotor with even loading, the coupled model is quite close to the CFD result. With the modification however, the results represented through the line with plus signs shows a marked difference between CFD and the coupled model. This marked difference was already appreciable when these results were first presented in Section 5.4 in absolute terms rather than the difference plots shown here. Figure 6.16 shows that the modified geometries have barely any effect at all on the induction distribution for both the methods but this is in line with what is seen in the circulation distribution plots for the high wind speed. The models, particularly the coupled model has a

large reliance on the circulation distribution and that is why a small change in Γ results in small changes in the induction distribution. As in the cases before, the coupled model is farther off from the CFD results but this is again because of the vorticity of the root and tip vortex being resolved in the local induction seen by the coupled model.

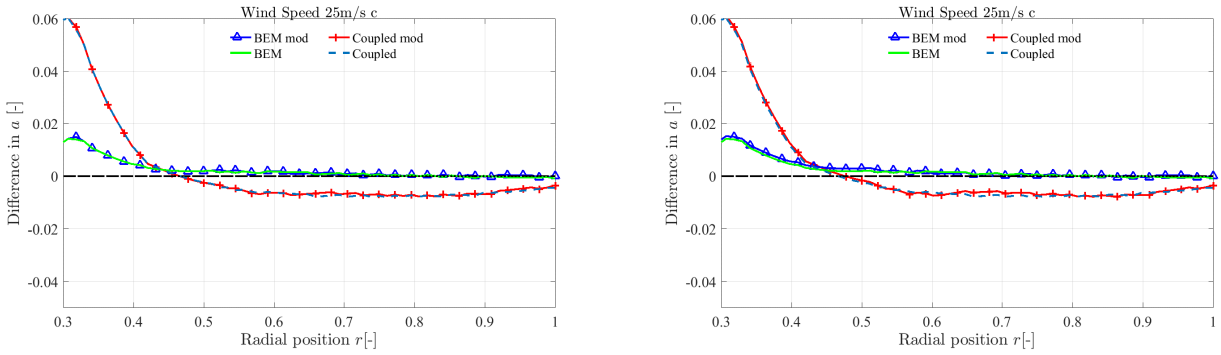

(a) Local A (b) Local B

Figure 6.16: Axial induction factor comparison for geometries *Local A* and *Local B* at 25 m/s

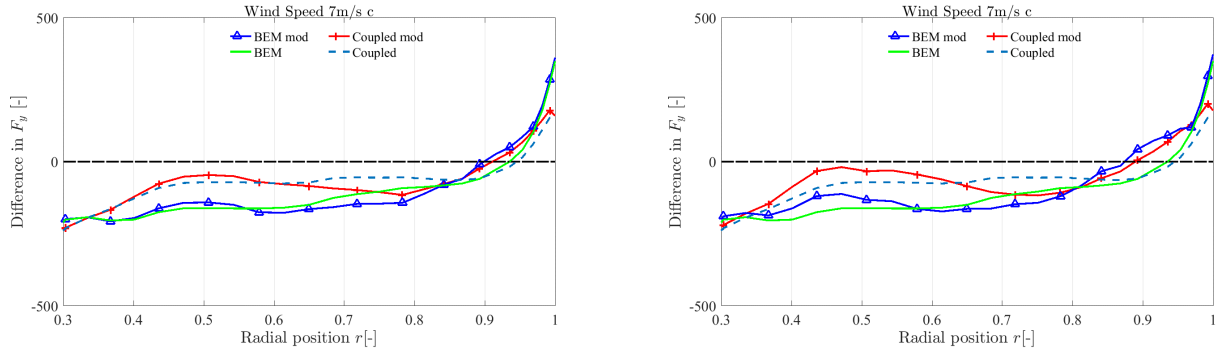

(a) Local A (b) Local B

Figure 6.17: Out-of-plane loads comparison for geometries *Local A* and *Local B* at 7 m/s

The overall impact of the increased chord is seen as an increase in the out-of-plane forces when compared to the loads for the evenly loaded rotor (see Figures 6.17a and 6.17b where the uneven geometry loads are higher than the even loading geometry). In addition the delta plots for the two modified geometries shows that the larger the chord increase, the greater the difference from CFD. In Figure 6.15, a comparatively larger difference was seen in the induction for the Local B geometry as compared to the Local A. The higher difference in the induction observed for the Local B geometry is translated into a larger difference in the out-of-plane loads as well. This is seen through Figure 6.17b, where from the line with plus signs, the coupled model shows a larger difference from CFD as compared to the Local A geometry in Figure 6.17a. It can also be seen from the presented plots that the BEM results from both the modified geometries remain mostly unaffected.

In general, even though there is a discrepancy, the coupled model is closer to CFD than the standard BEM. The high wind speed case in Figures 5.16 and 5.19 also shows that while the difference for the loads between the two modified geometries is barely noticeable, the BEM is consistently underestimating the loads and the near wake coupled model is much closer to CFD predictions. The underestimation of BEM can be explained for the same reason as the even loading i.e. departure from a disc like behavior at high wind speeds. This underestimation is also seen in the delta plots presented here in Figure 6.18 since they show the same results in a more easy to comprehend form as the absolute difference between the models and CFD.

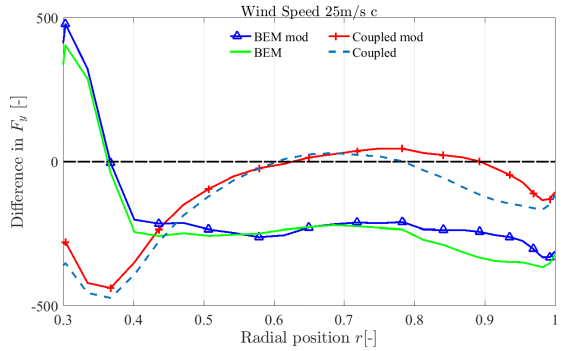

(a) Local A

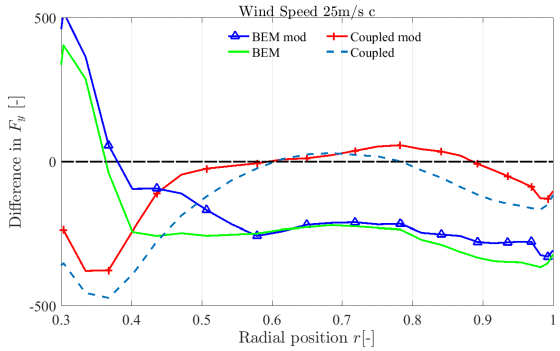

(b) Local B

Figure 6.18: Out-of-plane loads comparison for geometries *Local A* and *Local B* at 25 m/s

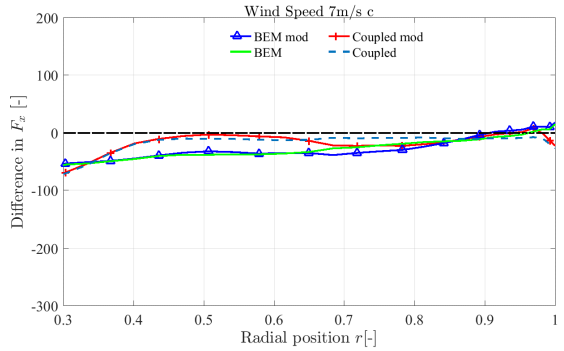

(a) Local A

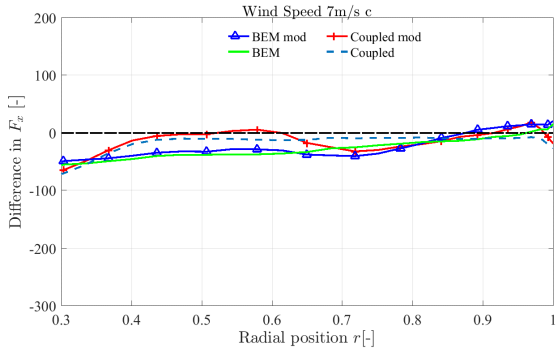

(b) Local B

Figure 6.19: In-plane loads comparison for geometries *Local A* and *Local B* at 7 m/s

The difference plots for the in-plane loads, Figure 6.19, show very little difference in the loads for the non-modified part of the blade, however it is seen that the loads decrease in the section where the chord is increased for both geometries and both BEM and coupled model, with the Local B geometry seeing a larger disparity from CFD.

A closer look at Figures 5.16 and 5.19 actually shows that the CFD results with the modified geometry first show an increased load in the increased chord region and then at around 80% of the blade span drop to lower loads compared to the even loading rotor. Whereas the models see only a drop in the load (compared to the even loading geometry) in the modified chord region starting around 60% of the blade span. This also corroborates the larger disparity between the models and CFD in the region around 60% of the blade onward where the chord is augmented in these two geometries as is seen in Figures 5.17a and 5.20a.

From Figure 6.19, it is seen that the BEM model shows only a slight decrease in the loads due to the modification in the geometry and for the rest of the blade underestimates the loading consistently compared to CFD. This is consistent with what was seen earlier in the case of the unmodified geometries as well. While the coupled model performs better up until the midspan of the blade, it also sees a decrease in the in-plane force in the region with the chord increase. This decrease is more pronounced in the case of geometry Local B which has a 20% chord increase in this region. One potential reason for the coupled model to show this pronounced decrease in the in-plane loads for a larger chord increase can be attributed to the coupling factor.

The fact that the increased chord effect is smoothed out and takes place very gradually means that the effect of the increased chord is felt on a larger section of the blade. It is useful to recall that the coupling factor is calculated for each section and then averaged over the entire rotor. This means that if a larger portion of the blade is changed in any way then the resulting effect of this change influences a larger number of sectional coupling factors. The resulting

area averaged coupling factor thus sees a larger bias because of the change. This causes an effect on the entire blade because the coupling factor is applied at each section. This could impact the final induction and load distribution causing the in-plane force to be inaccurate and farther off from the CFD results. This effect of the coupling factor can also be used to explain the larger difference from CFD in the out-of-plane loads in the region where the chord is modified.

A general observation about the out-of-plane and in-plane loads in the case of the local chord modifications can also be made from the induction distributions presented in the previous chapter. In Figures 5.15a and 5.18a it is seen that the induction factor is higher than the optimal power extraction value of 0.33. Thus increasing the induction in this range should result in a lower in-plane force (which translates into a lower power). In addition, both the BEM and the coupled model use empirical relations to model the high induction effects associated with rotors that are loaded beyond the optimal point. This also means that the BEM based models are not as accurate as CFD in estimating the loads in this region. This could also potentially be the reason why a large difference is seen between both BEM and coupled model compared to CFD for the modified geometries, particularly in the parts of the blade where the a is higher than the optimal value due to the higher chord. A clearer picture of the results could have been obtained if the pitch settings were changed slightly to reduce the induction to a more optimal value around 0.3 for these modified geometries. While this has not been done it is likely that this would reduce some of the error seen by the BEM and the coupled model for these geometries.

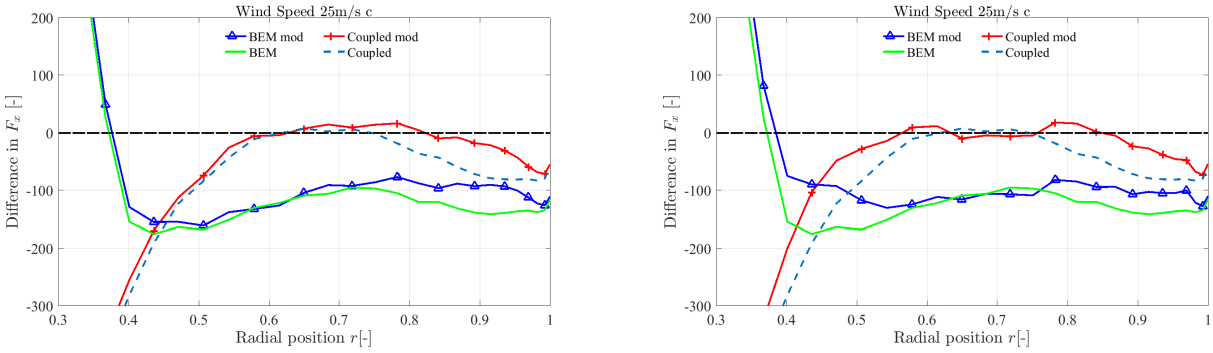

(a) Local A

(b) Local B

Figure 6.20: In-plane loads comparison for geometries *Local A* and *Local B* at 25 m/s

The high wind speed results for the in plane forces for both modified geometries appear to be almost identical with the results for geometry Local B(Figure 5.20b) showing a slight dip as compared to the results for Local A(Figure 5.17b), particularly in the section of the blade where the chord increase is highest. The improvement in the coupled model over the standard BEM at high wind speeds is again because the BEM becomes less accurate at high wind speeds due to the actuator disc assumption.

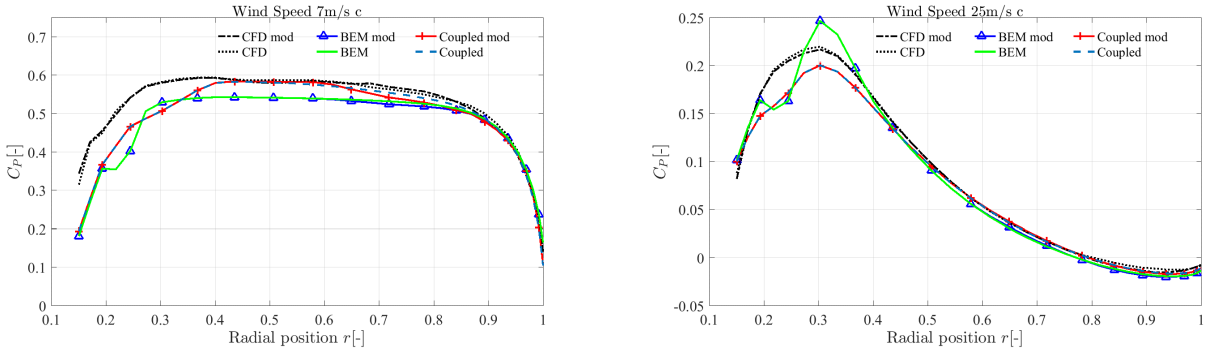

(a) 7 m/s (b) 25 m/s

Figure 6.21: Local power coefficient comparison for geometry *Local A*

Correspondingly, the trend seen for the in-plane force translates into the local power coefficient as seen in Figures 6.21 and 6.22. Here again it is observed that the BEM constantly underpredicts the C_P and the coupled model performs better but sees a drop around 65% of the blade span and coincides with the BEM results soon after. Since the C_P curves are calculated using the in-plane forces, the same behavior is seen for the high wind speed in the case of the local power coefficient for both Local A and Local B geometries.

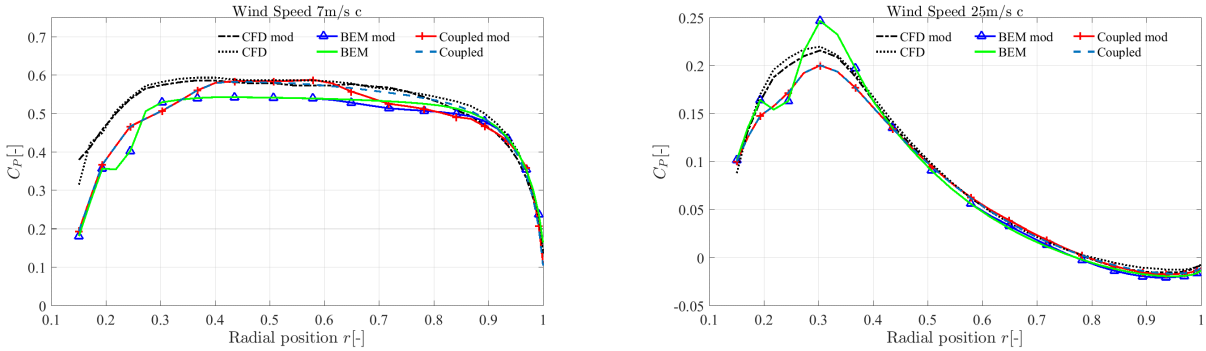

(a) 7 m/s (b) 25 m/s

Figure 6.22: Local power coefficient comparison for geometry *Local B*

Delta plots with unmodified geometry

As mentioned before, for the in-plane loads, a closer look reveals that the CFD predicts a slightly higher load and the aerodynamic models show a decrease in the loads. This is further clarified by plotting delta plots that compare the difference between the plain and modified geometry results for each model. This time the reference line or 0 line represents the results for that respective model but with the even loadin case or unmodified geometry. This type of delta plot is very useful in determining how much a model is influenced by a change in chord or circulation distribution and quantifying how each model behaves when representing said change. The result of these delta plots are shown here for the low wind speed of 7 m/s case only. From Figure 6.23, it is seen that the near wake coupled model sees the largest effect on the induction because of the changed geometry. An interesting observation here is to see that the solid line shows that the modified geometry in the BEM only affects the induction around the region where the chord starts to change for both Local A and Local B geometries. Conversely, the coupled model starts deviating from the reference line of the plain geometry much sooner along the blade span, and almost as far back as 40% span.

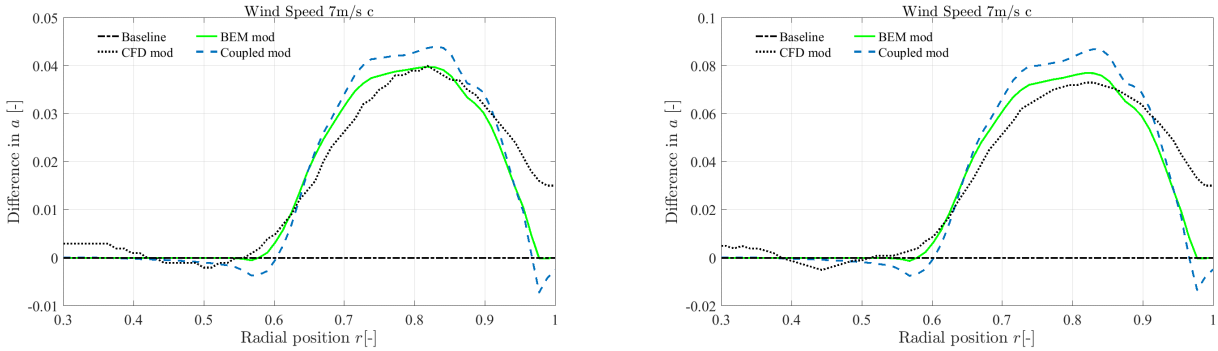

(a) Local A

(b) Local B

Figure 6.23: Difference in a for the different models between the unmodified and modified geometries *Local A* and *Local B*

The out-of-plane loads comparison shows that the CFD curve sees the largest difference between the unmodified and modified geometry, followed by the BEM modified geometry curve. The coupled model sees a slightly smaller impact of the chord increase. The increased chord does increase the loads, however it also increases the induction which then has a slightly negative effect on the final loads distribution. This plot only signifies that the loads are affected more in the BEM due to the increased chord, it does not tell qualitative information about how accurate the increased effect in the BEM is. Once again in Figure 6.25, the dashed line of the coupled model sees a deviation in the loads much earlier than the BEM for the modified geometry, indicating a higher "communication" of aerodynamic effects in the neighboring sections.

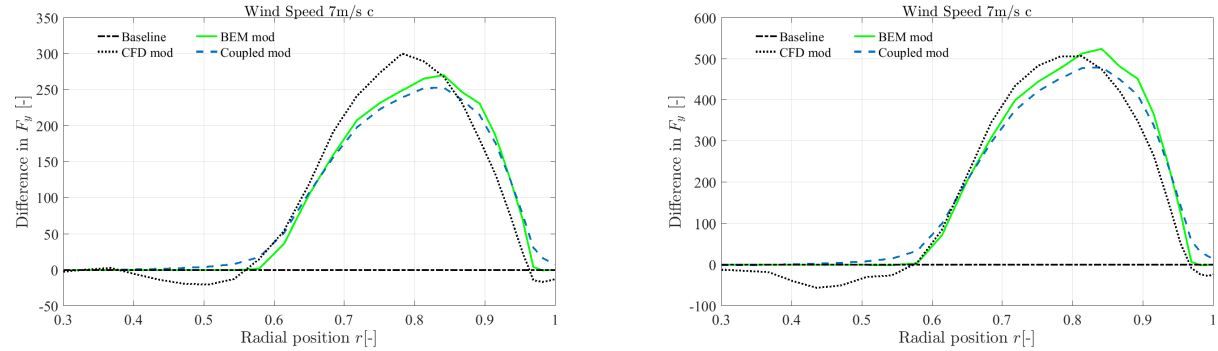

(a) Local A

(b) Local B

Figure 6.24: Difference in F_y for the different models between the unmodified and modified geometries *Local A* and *Local B*

Lastly, the differences in the geometry are seen least in the in-plane forces however here it clearly shows that while the CFD shows an increase in the loads, the aerodynamic models show a decrease. As mentioned before one of the reasons could be the coupling factor being biased because of the larger section of the blade being affected by this type of gradual chord change. Another possibility is that the aerodynamic models are more sensitive to variations in the angle of attack due to a higher induction. This can be explained in two ways. A larger chord results in a larger induction. This can then decrease both the angle of attack resulting in a lower lift, and the local inflow angle resulting in a smaller component of the lift in the rotor plane. Both these phenomena lead to a reduction in the in-plane forces. However, the CFD results show that the increased chord is the dominating effect in this case thus leading to an increase in the in-plane force, where the models show a decrease in the force as compared to the unmodified rotor. It seems here that the models disagree with CFD and that for the models, the increase in induction has a stronger negative

impact on the loads, then the positive effect of the increased chord. As mentioned before, this difference may also be simply because the CFD results are more reliable than the models due to a being higher for the larger chord in the modified sections of the uneven geometries.

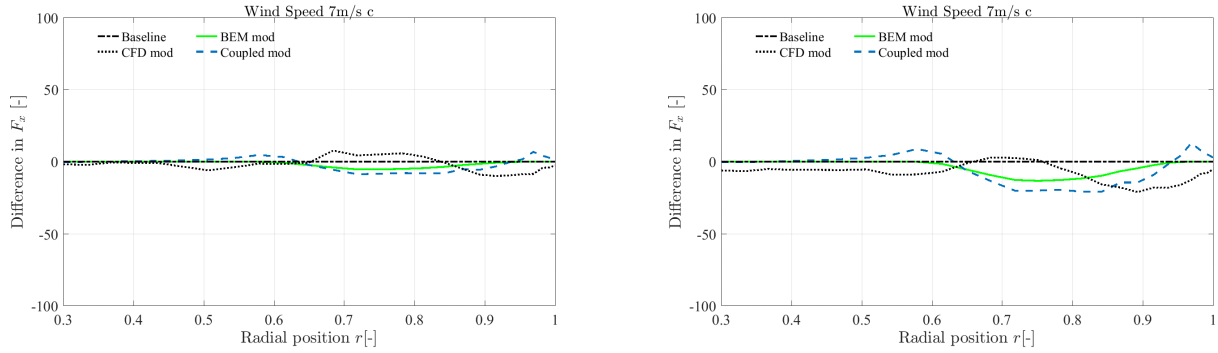

(a) Local A

(b) Local B

Figure 6.25: Difference in F_x for the different models between the unmodified and modified geometries *Local A* and *Local B*

To remove the uncertainty of the larger bias on the coupling factor due to a larger modified portion of the blade, a small test run of the aerodynamic models is carried out. This test run compares a truly abrupt increase of 20% in the chord at the 60-75% blade span location. The results for this will be presented at the end of this section and it will shed light on the performance of the model for sudden jumps in the circulation distribution which is also an interesting case for representing flaps and other add-ons.

6.5.2 Slender blade geometries

Circulation distributions

The circulation distribution for the slender blade geometries are shown in Figures 6.26 and 6.27. It is seen that for both wind speed cases, the added chord in the root section leads to a higher circulation value as compared to the unmodified circulation and the decreased chord in the outboard section leads to a reduced circulation. This conforms with expectations since the circulation is directly proportional to the chord from Equation (3.42). However for the high wind speed case, the effect on the outboard part of the blade is very small and this is because at these operating conditions the rather small lift values make the effect of the changed chord even smaller. The lift coefficient is very small because the blade experiences small negative angles of attack(can be seen from Figure 6.1b. The airfoils in this part of the blade have around 24-30% thickness and from the airfoil polars presented in Section 4.1, it can be shown that this translates into small values of the lift coefficient. Thus, the dominating effect on the circulation distribution is the relative velocity and the small C_l makes the effect of the chord difference smaller.

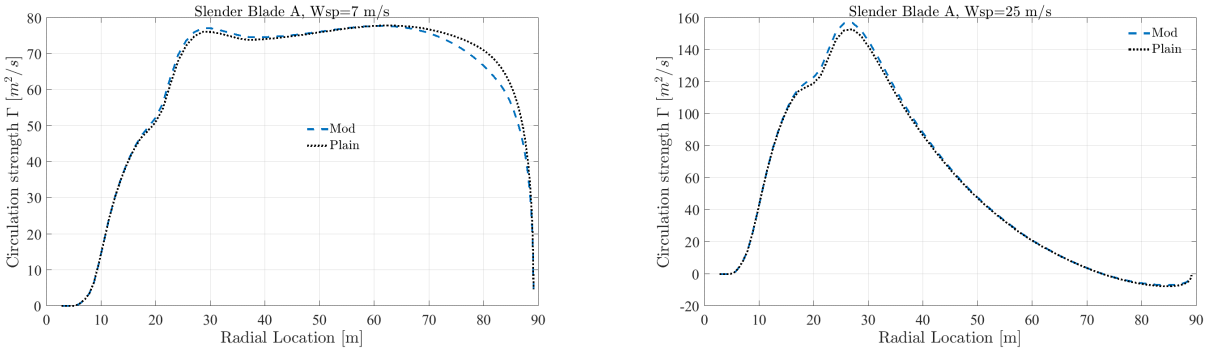

(a) 7 m/s (b) 25 m/s

Figure 6.26: Circulation distribution for plain and modified geometry *Slender A* at 7 m/s and 25 m/s

With Figure 6.27 the same trend is seen but because the chord is increased and decreased more than slender geometry A, the effect is amplified in the circulation distribution.

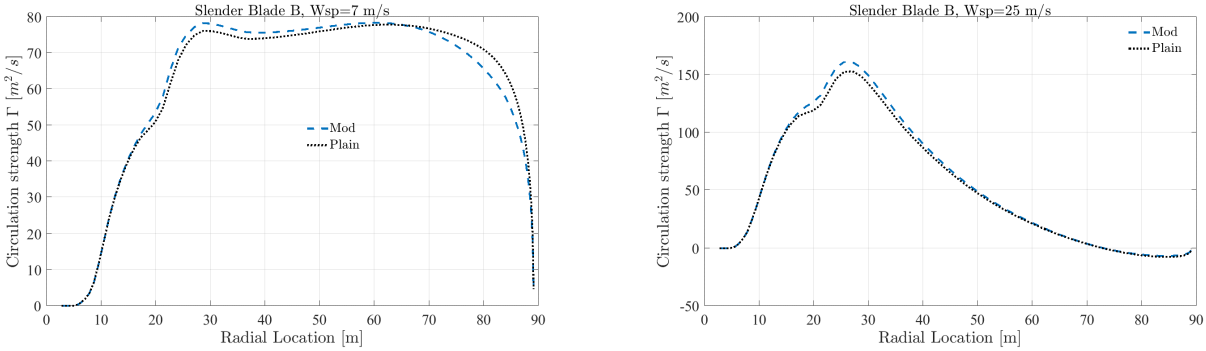

(a) 7 m/s (b) 25 m/s

Figure 6.27: Circulation distribution for plain and modified geometry *Slender B* at 7 m/s and 25 m/s

Delta plots with CFD

Next, the results shown in Figure 5.21 through 5.26 are presented in the form of delta plots where just as in the case of the geometries *Local A* and *Local B*, the differences are calculated for the aerodynamic models for each geometry to its own respective CFD results. One clear observation is that the coupled model is closer to CFD for the lower wind speed just as was observed for the case of the unmodified rotor without coning. As the rotor for the DTU 10 MW turbine is originally quite slender as well, it makes sense that both these geometries have similar trends as seen for the unmodified rotor. The high wind speed induction once again shows that the coupled model predicts something different from the global induction from CFD, however, as can be seen with the load comparisons ahead, the coupled model is more accurate in estimating the loads. This means that the local induction given by the coupled model is modeled more realistically.

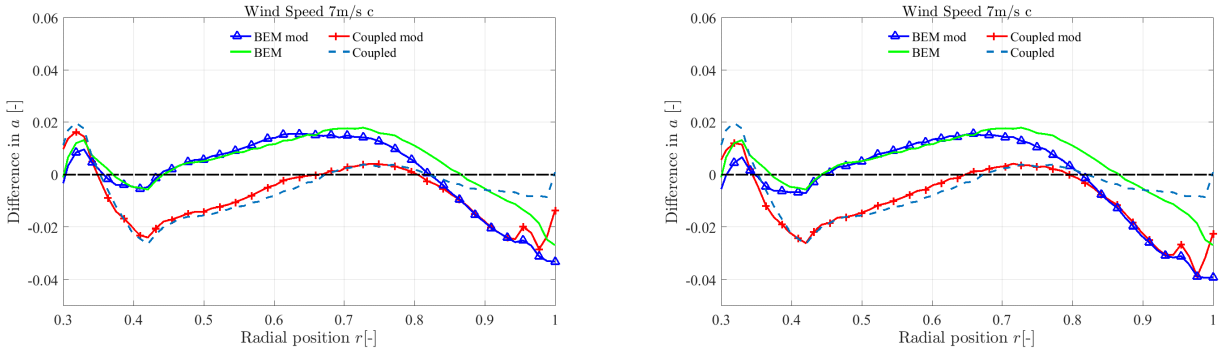

(a) *Slender A* (b) *Slender B*

Figure 6.28: Axial induction factor comparison for geometries *Slender A* and *Slender B* at 7 m/s

The observations mentioned hold true for both the geometries that are analysed and it is seen that at the tip the modified geometries show a larger deviation than for the unmodified geometry for the low wind speed. Between the two geometries tested, this delta at the tip is higher for the slender geometry B which had a smaller chord at the tip than geometry A. This means the more slender the blade, the higher the difference in the results of CFD and the couple model at the tip. The high wind speed plots for both geometries show that the induction is not significantly affected based on how much the chord is added or reduced at the different blade sections and almost identical differences are seen for both geometries in the axial inductions.

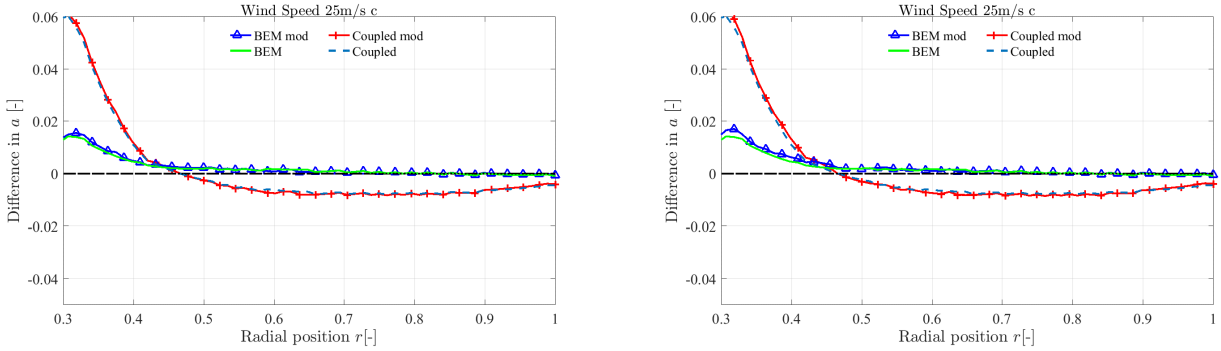

(a) *Slender A* (b) *Slender B*

Figure 6.29: Axial induction factor comparison for geometries *Slender A* and *Slender B* at 25 m/s

The next four plots show the out-of-plane loads for the two slender geometries at the two different wind speeds. The utility of the coupled model and the added benefits of the near wake vorticity for highly slender blades becomes clearer with the help of these plots. It is seen that at both wind speeds the out-of-plane loads not only have smaller deltas as compared to BEM, but they also are smaller for the more slender case with geometry *B*. The spread of the high wind speed curve for geometry *B* around the CFD reference line is smaller than that of geometry *A* i.e. it appears flatter and closer to the CFD line along the blade span. The low wind speed case also shows that the fit between CFD and coupled model is even better with the more slender blade. The results are quite consistent with what was seen for the evenly loaded rotor and this is because even though the current geometries are more slender, the change in chord distribution is applied throughout, thus allowing the coupled model to perform as well as it does for an unmodified rotor with a more even distribution.

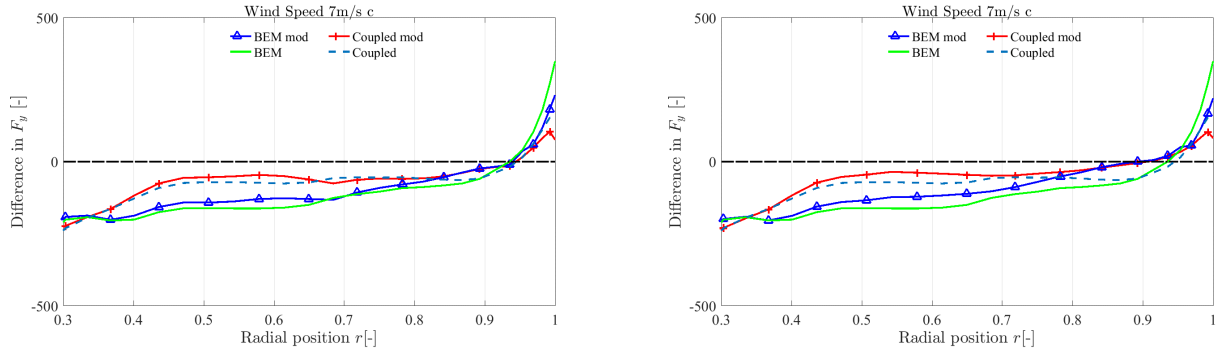

(a) *Slender A* (b) *Slender B*

Figure 6.30: Out-of-plane loads comparison for geometries *Slender A* and *Slender B* at 7 m/s

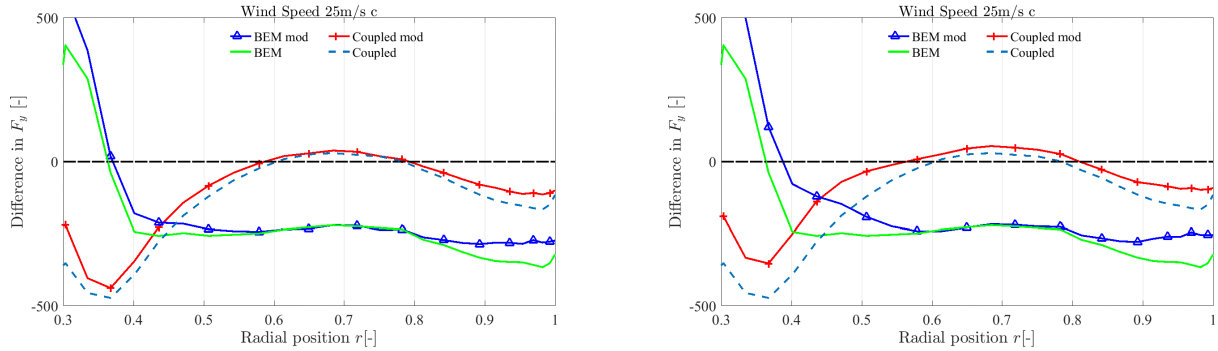

(a) *Slender A* (b) *Slender B*

Figure 6.31: Out-of-plane loads comparison for geometries *Slender A* and *Slender B* at 25 m/s

Figures 6.32 and 6.33 show that while the BEM lies quite close to the CFD calculated value of the in-plane load, the coupled model has an even smaller difference comparatively and here even with the modified geometry the coupled model is able to resolve the loads quite well because of the improvement through the near wake model. Once again, the delta plots indicate that the performance of the model is even better in the case of the more slender blade as can be seen through both wind speed cases in Figures 6.32a and 6.32b. For both the in-plane and out-of-plane loads, for high wind speeds, the delta plots show that the standard BEM has an offset from CFD results for the same reasons that were explained earlier.

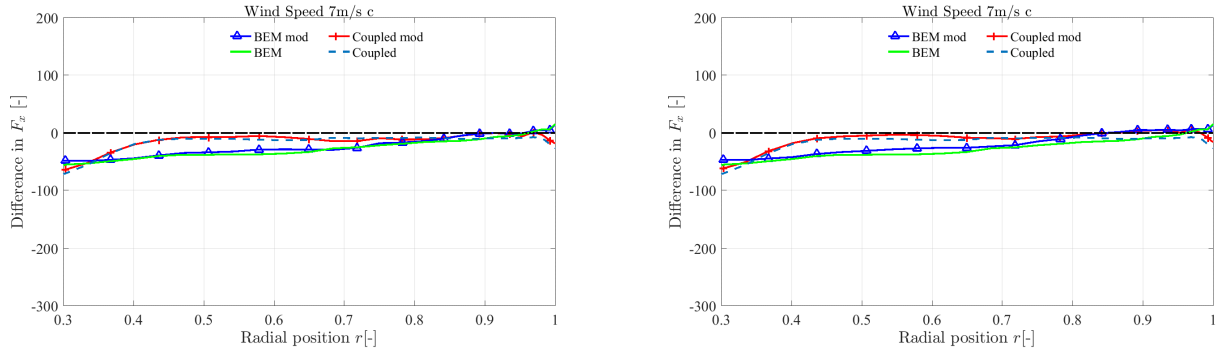

(a) *Slender A* (b) *Slender B*

Figure 6.32: In-plane loads comparison for geometries *Slender A* and *Slender B* at 7 m/s

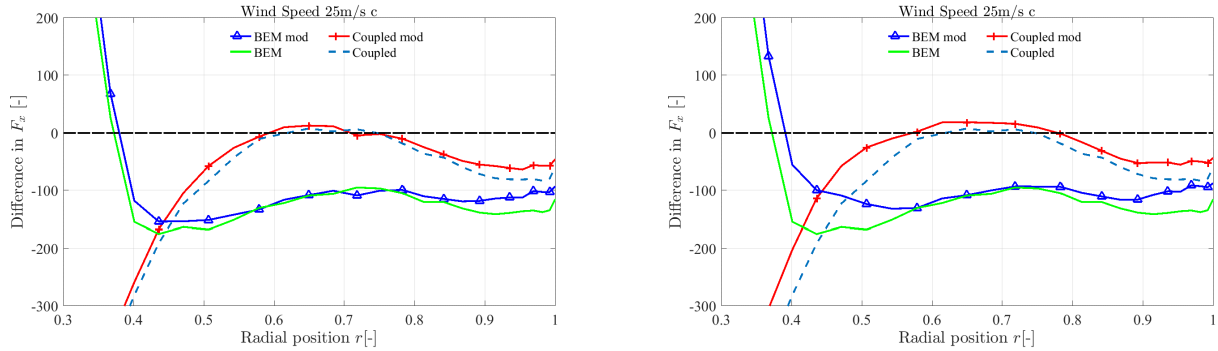

(a) *Slender A* (b) *Slender B*

Figure 6.33: In-plane loads comparison for geometries *Slender A* and *Slender B* at 25 m/s

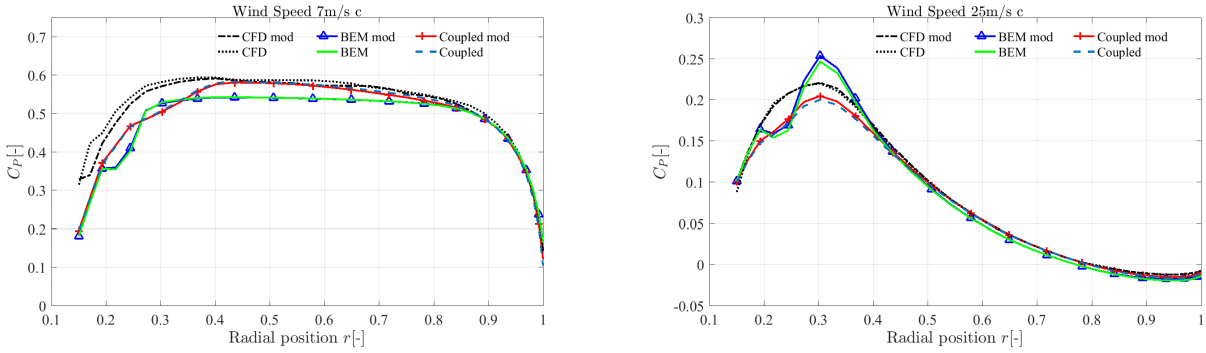

(a) 7 m/s (b) 25 m/s

Figure 6.34: Local power coefficient comparison for geometry *Slender A*

The improvement in the in-plane loads is then translated into a better approximate for the local power coefficient where it is seen through Figures 6.34 and 6.35 that there is a constant offset in the BEM results as opposed to the coupled model which is much closer to the CFD local power coefficient. Another interesting result is that the BEM

consistently underpredicts the local power coefficient and a similar result was seen by Madsen et al. [15] in a comparison with actuator disc simulations, where it was suggested that the deficiency in the power coefficient comes from the pressure variation in the rotating wake behind the rotor not being taken into account by the standard BEM model. While between 30-40% of span, the coupled model is different from CFD, it fits better after this value because of the trailed vorticity effects and interaction between the annuli. Also for the higher wind speed, the local power coefficient from the coupled model is closer to the CFD results since the root vortex is modeled more realistically as compared to BEM where the BEM results slightly overestimate the loads at the root.

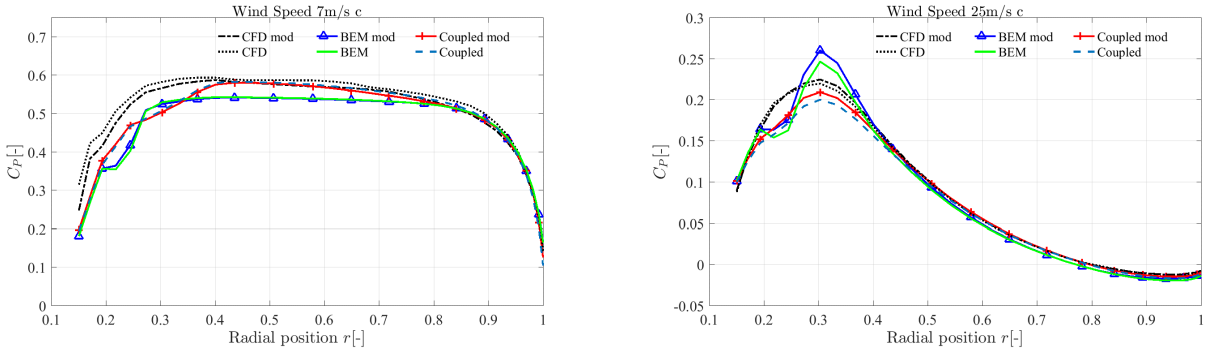

(a) 7 m/s (b) 25 m/s

Figure 6.35: Local power coefficient comparison for geometry *Slender B*

Delta plots with unmodified geometry

Just like for the local chord increase geometries *Local A* and *Local B*, it is also interesting to see to what extent each method is affected by the change in the geometry. The baseline in these plots are the results from the respective model but for the plain geometry. Only the high loading/low wind speed is shown here as the effect for the larger wind speed is small as has been seen. It is seen that in terms of induction, the largest difference is seen through the coupled model on average where the difference between the modified geometry and the plain geometry is the highest mid span as well as at the tip. The BEM sees a less pronounced effect comparatively and CFD seems the least sensitive out of the three methods shown here.

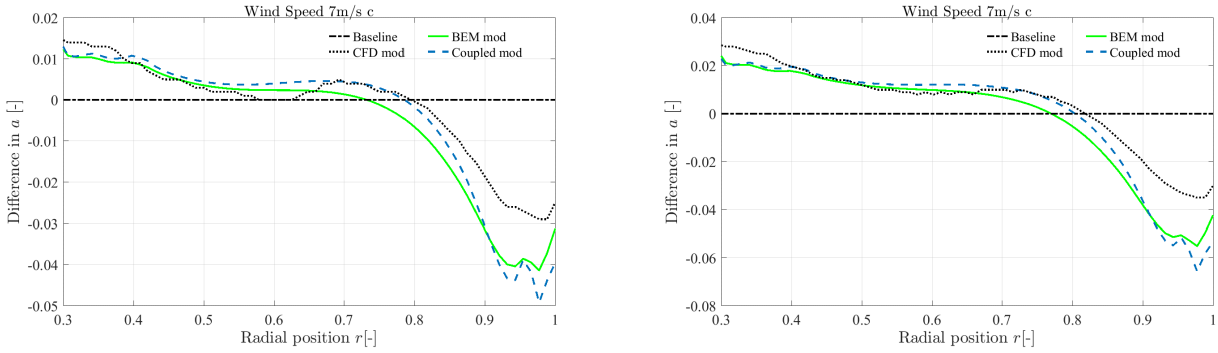

(a) *Slender A* (b) *Slender B*

Figure 6.36: Difference in a for the different models between the unmodified and modified geometries *Slender A* and *Slender B*

The out-of-plane loads comparison shows that the BEM curve sees the largest difference between the plain and the modified geometry however it must be kept in mind that the trend in the delta plots(Figure 6.30 through 6.33) comparing the models to CFD results showed that the coupled model does indeed perform better. This indicates that

even thought the largest difference is seen by BEM it does not mean it is more accurate or realistic as it is still farther away from the higher fidelity method.

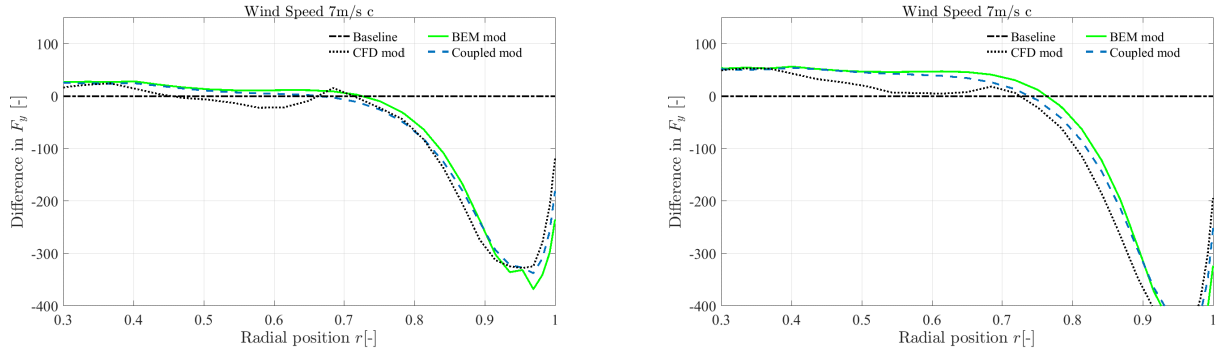

(a) *Slender A* (b) *Slender B*

Figure 6.37: Difference in F_y for the different models between the unmodified and modified geometries *Slender A* and *Slender B*

Lastly, the differences in the geometry are seen least in the in-plane forces where all three methods saw very little change because of the slender geometries. It can be seen though that the CFD sees the largest difference followed by the coupled model and then the BEM. Because the chord change was applied throughout the blade span, it is a bit difficult to ascribe trends and reasons for these trends simply by looking at these plots. However, it is still reasonable to conclude from the preceding discussion in this section that the coupled model covers some shortfalls of the standard BEM through vorticity effects and the independent annuli assumption.

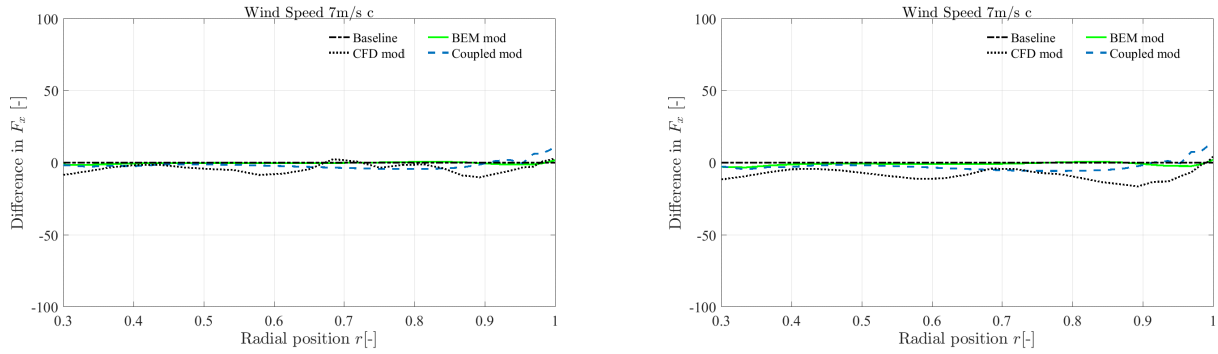

(a) *Slender A* (b) *Slender B*

Figure 6.38: Difference in F_x for the different models between the unmodified and modified geometries *Slender A* and *Slender B*

6.5.3 Abrupt change in chord distribution

The local chord increase geometries *A* and *B* analyzed in this study are purposefully kept very smooth as was explained in the geometry setup in Section 4.4 in order to avoid CFD convergence issues. However, as was seen through Figures 6.13 and 6.14 this leads to a very gradual increase in the circulation on the blade and an abrupt change would represent higher unevenness in the loading. For this reason, a small test is carried out to see how the coupled model and BEM react to an actual abrupt change in the chord distribution which no doubt results in an abrupt change in the circulation. Thus, the local geometry *B* with 20% chord increase is selected but this time, no additional smoothing is

applied and the increase in the chord between 60-75% of the blade span is kept as it is to be analyzed with the two models. The geometry is shown in Figure 6.39. It is to be noted that for this simulation 80 points are used and the point discretization is different from the full cosine discretization used earlier in the analysis. Here, the points become finer in the region close to 60-80% of the blade span. The tip also has a higher resolution than the other regions of the blade. The point spacing is adjusted so that there is no sudden increase or decrease in resolution rather the point spacing is temperately moving to a finer resolution in the areas of interest. This is done to ensure easy convergence as well as a good resolution for the induction and the loads close to the bump in the chord distribution.

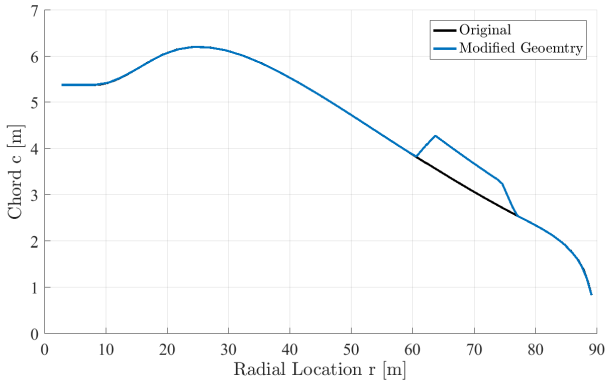

Figure 6.39: Modified geometry with an abrupt increase of 20% in the chord distribution

As expected, the circulation distribution obtained in this case is very locally affected due to the local chord change and unlike the local chord geometries *A* and *B*, the circulation change occurs only at the blade locations where the chord increase is applied. Figure 6.40 shows the circulation distribution in this case for the high loading case at 7 m/s. This means that the large effect on the coupling factor that was seen in the *Local A* and *Local B* geometry results is not expected here since the change in the chord is in a relatively smaller section of the blade.

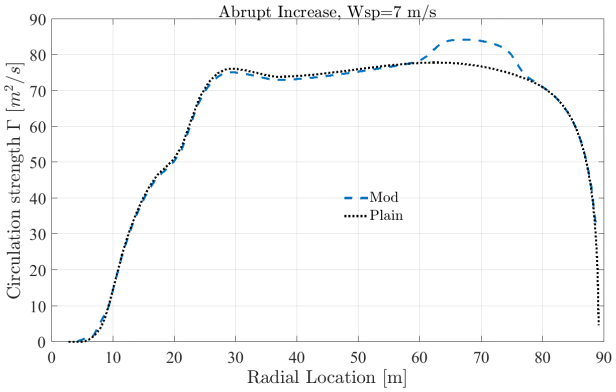

Figure 6.40: Circulation distribution obtained for geometry with abrupt change

The induction distribution is shown only for the area of interest where the chord increase is applied in Figure 6.41. It is seen through the dashed line and the red line with plus signs that with the coupled model, the modified geometry inductions see the effect of the "flap" or increased chord earlier then it physically begins. This is seen through the deviation of the line with plus signs from the dashed line starting almost 10% earlier along the blade span. On the other hand the BEM only sees the effect at the actual geometry change and this is a consequence of the assumption of the independent annuli. As mentioned in Chapter 2, when 3D aerodynamic devices are considered, different sections do "feel" the effect of the neighboring sections and this is clearly seen with the coupled model.

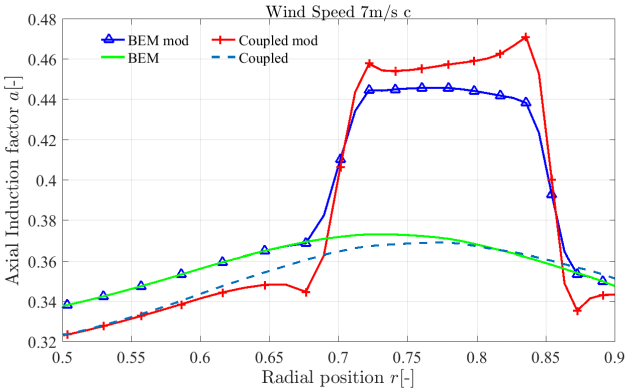

Figure 6.41: Induction distribution for geometry with abrupt change specifically in section with chord increase

The same effect is generally seen for both out-of-plane and in-plane loads where the deviation in the coupled model starts earlier as the neighboring sections are influenced by the flow field interaction of the increased chord section. The effect for the out-of-plane loads is quite well in line with expectations for a flap like device where the coupled model predicts a slightly higher axial load before the flap begins and then a slightly lower and more smoothed response as compared to the BEM. On the other hand for the in-plane loads, the higher induction decreases the angle of attack and the inflow angle which subsequently rotates the incoming flow. The results is that a smaller component of the lift force is seen in the rotor plane and this effect is seen with the sharp decrease in the in-plane force as compared to the unmodified geometry. Essentially more of the flow is now perpendicular to the blade and thus the in-plane force is smaller.

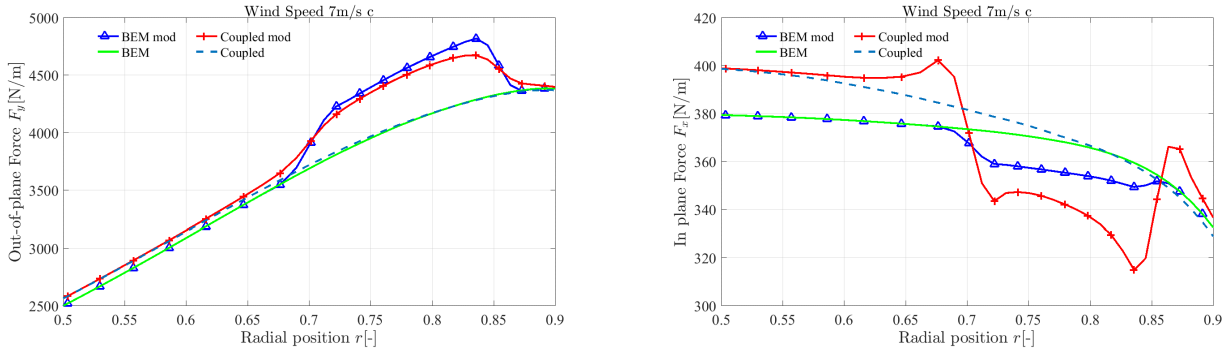

(a) Out-of-plane

(b) In-plane

Figure 6.42: Aerodynamic loads with BEM and coupled model compared for abrupt chord increase

This comparison shows that the coupled model does resolve sudden changes in the distribution more realistically and in line with common expectations. The aim of the uneven loading distribution was also to analyze whether the model performs better as compared to BEM in the presence of flaps or other aerodynamic add ons which complicate the loading distribution making it increasingly irregular and uneven. This small comparison therefore adds more credence to the model for such applications.

In conclusion, the discussion of the results has shown that the even loading cases show a good agreement between CFD with both BEM and the coupled model for the loads. The inductions at high wind speeds do not match the CFD inductions and this is because of the difference of local and global inductions. The effect of the local inductions form the coupled model however shows an improvement in the loads which is a more reliable benchmark for comparison. The in-plane loads are seen with a deficit along the blade span with BEM however this is not the case with the coupled model. Particularly at the higher wind speeds the coupled model is closer to CFD.

For the unevenly loaded rotors, both the model results are farther from CFD if a very large section of the blade is modified. The coupled model is closer to CFD but still some disparities are seen for such type of modifications. For highly slender blades, the trends show that both models are again close to CFD results with some improvements seen with the coupled model at high wind speeds and with the in-plane forces as in the case of the even loading.

Chapter 7

Conclusion

In this chapter, the results and discussions presented in the previous chapters will be summarized in a concise manner listing the most important findings. The importance of the findings with regards to answering the research questions in a larger context will be discussed followed by recommendations that could shed more light on the performance and improvement of both BEM and the coupled NWM.

7.1 Discussion

The introduction of this thesis defined that the aim is to investigate methods or ways to improve the standard Blade Element Momentum method in order to cover the shortfalls that have been seen over the years in this method. These shortfalls need to be addressed particularly in relation to Computational Fluid Dynamics simulation results. Research questions have been proposed at the start of the thesis and the work carried out during the process has been with the aim to answer these questions satisfactorily.

For this purpose, some limitations of the BEM have been identified which reduce its accuracy and render it less physical than reality. The near wake model [5] has been chosen to provide the necessary adjustments in order to compensate for some of these assumptions and limitations. Particularly the assumption of independence of the annuli as well as effects of the wake on the blade are resolved through this model giving a bit more depth to the basic BEM model by accounting for the flow field in a more physically rich description. Cases where the rotor behaves less like an actuator disc show the BEM performance to drop whereas including the trailed vorticity effects in the vicinity of the rotor improves the results in such cases. In addition, a separate tip loss factor is not necessary with the coupled model as it resolves the effect of the vorticity due to a finite number of blades in the near wake because of its formulation.

The steady state version of the model has been implemented based on the original coupled model. The results for the current implementation are validated with an aeroelastic code HawC2, as well as through comparison with another CFD solver EllipSys CFD. One of the research questions involved seeing the potential improvements due to the near wake model to the results for evenly loaded rotors. The analysis consisted of testing the NWM with the DTU 10 MW rotor with an unmodified rotor having non-deformed blades. It has been generally seen that the coupled model estimates the in and out-of-plane loads much better than the standard BEM for almost the entire blade span on a plain rotor without coning. Even for a rotor with coning included, it has been seen that in the mid span region the model predicts the in-plane loads and inductions better than the regular BEM. Higher loads are observed at the tips by both BEM and the coupled model for this comparison due to no coning being modeled in these methods.

For the case of the inductions, the local inductions from the models seem to show a different behavior than the global induction calculated through CFD using the arc averaging method. The local and global inductions on a rotor are quite different in regions of high vorticity. For the low wind speeds, this means that the results from CFD and the two models do not agree at the tip because of the dominating effect of the tip vortex. For the high wind speeds, the results for the global inductions extracted from CFD do not physically represent the effect of the root vortex which is seen by the near wake model. The difference between the two inductions can be corrected for the low wind speed case by multiplying the inductions from the models with the tip loss factor. This corrects for the effects of the tip

vortex which are seen by the models. However, the same approach cannot be used to correct for the high wind speed cases, where the load distribution is quite different from the low wind speeds, and it is not the tip vortex but the root vortex, which causes the difference between local and global induction. Thus the tip loss factor in this case cannot compensate for the difference between the local and global induction and the coupled model shows a larger induction at the root compared to CFD and also BEM. Despite this difference in the induction, the loads are seen to be better resolved than BEM at the high wind speed/ low loading case as has been observed in Section 5.2.2. This is because the standard BEM relies on the actuator disc assumption which is less physical at low tip speed ratios. The coupled model takes into account the trailed vorticity thus giving more accurate local inductions even at high wind speeds which results in the improvement in the in-plane and out-of-plane loads.

An important research question that has been studied is the case of uneven loading as more slender blades and aerodynamic add-ons on the blades are becoming increasingly commonplace with the progress in the wind energy industry. Because of this blades experience an uneven loading, and the performance of the coupled model has been investigated for such uneven loading on blades. For this purpose two different type of blade geometries have been compared with the plain geometry and with the CFD results for this modified geometries. The results for this analysis have been discussed in Section 6.5. The two types of considered geometries include a local change in the chord at a specific spanwise location and a second type which involves a highly slender blade. The results for these cases generally show an improvement however some caveats are seen for the local chord increase. For the latter case of slender geometries, it has been seen that the coupled model performs well in relation to CFD and matches quite well compared to the BEM with only slight disparities at the tip.

For the geometries with the local chord increases it has been seen that both the models have a larger difference to CFD particularly in the region with the chord modification. The coupled model still performs well however, the difference as shown in the discussion in Section 6.5.1 is higher for this case. This has been attributed to the fact that the gradual and smoothed increase in the chord for this type of geometry has an effect on a large portion of the blade, this in turn affects the coupling factor more. This has an effect on the entire induction distribution and hence loads distribution. In order to isolate the effect of this larger modification on the blade, an extra case for an abrupt chord increase of 20% has also been studied where the coupled model results show behavior that is reminiscent of a flap. Flaps are generally a source of unevenness in rotor load distributions so this abrupt increase case is rather appropriate towards the research question regarding uneven loading and the loads seen as a result are in accordance with what is expected for flaps. This case has exhibited that the larger error in the local chord increase has more to do with the bias in the coupling factor due to a large portion of the blade being modified.

The results for the different analysis for even and uneven loading are summarized . The inductions and in-plane and out-of-plane loads are described and the extent of agreement and disagreement with CFD for both models is commented upon.

Table 7.1: Table summarizing the performance of the models for the different cases analyzed

Configuration	Axial Induction (local)	Out-of-plane load	In-plane load
Even loading with coning	Improved over BEM for a large section of the blade span	Improved in large section of blade, discrepancy at tip due to coning for both models	Improvement in almost entire blade span, discrepancy at tip due to coning angle. Standard BEM has a constant deficit with CFD
Even Loading without coning	Improved compared to CFD for a large section of the blade span	Improved for entire blade span except at root. Both models close to CFD	Improved for entire blade span except root. Standard BEM has a constant deficit with CFD.
Uneven Loading with local changes in loading	Improved generally, but larger differences are observed if unevenness is spread over a larger section of the blade	Improved over the standard BEM but large differences seen if a large section of blade span is affected by the uneven loading	Improved over the standard BEM except in the region of local change in loading, where both models show similar behavior. Slight improvement with the coupled model.
Uneven Loading with spanwise change in loading i.e. highly slender blades	Improved for a large section of the blade span	Improved over the standard BEM over almost entire blade span, except at root	Improved over entire blade span except root. Standard BEM has a constant deficit.

7.2 Future work and recommendations

The steady state implementation of the near wake model has exhibited its utility based on the results of this study. Further investigations and future works can thus be proposed based on the findings so far to contribute to the body of knowledge.

- Both the aerodynamic models that have been studied in this thesis rely on airfoil polars. As has been described in the discussion of the validation case against EllipSys, the polars that are used are derived from CFD simulations and have different Turbulent Intensity settings. The CFD method used in the current study uses a different turbulent intensity to model transition. For a truly reliable comparison the polars should be used that use the same turbulence level as the rotor CFD simulations. Indeed one of the limitations identified for the BEM also included its reliance on airfoil polars and the reliability of the used airfoil polars. In this regard, generally speaking more reliable polars and accurate 3D corrections of these polars should remove uncertainties in the model results. So a more detailed analysis with better polars can shed more light on the performance of the BEM and the coupled model.
- The coupled model developed in this study is a steady state implementation that is feasible for steady state performance analysis of turbine rotors at fixed operating points. The next step is naturally to develop a full dynamic code which takes into account the shed vorticity and the dynamic effects caused by the unsteady inflow conditions of the blade. Such a tool can then be used for full scale aeroelastic simulations that are more accurate compared to the standard BEM because of the accurately accounted for dynamic effects in the near wake of the rotor.
- Even though the coupled model does not need a tip loss factor in its formulation because the effect of the tip vortex is resolved in the method, it still relies on a reference BEM calculation to adjust the coupling factor. This reference BEM calculation does need a tip loss factor in its calculation. In this way, the effect of the tip loss factor does manifest in the final results of the model. Therefore the effect of the tip loss factor can be investigated to

see how large an impact can be seen in the end result based on the tip loss factor. Many studies have been done investigating the nature of the tip loss factor and on improving its value. These can be implemented to see if there is a potential benefit of using a more advanced tip loss mechanism. The work of Branlard [38], could be an interesting option for such a study.

- As has been seen with the analysis of the rotor with and without coning, there is a slight difference in the overall loads and an appreciable difference at the tips owing to the cone angle. The BEM and the coupled model used in this study currently do not have any means to account for the out-of-plane deflections or change in rotor geometry such as sweep or cone angle. However, since there is a difference and because more rotors include sweep and coning angles it is also worthwhile to implement these angles in the coupled model in order to make it more realistic

- To remove the uncertainty between the induction from CFD and the aerodynamic models a more detailed study on induction calculation methods from CFD can be carried out. This has been one of the reasons why the conclusions of the study are based on the loads rather than the inductions. If a reliable method to calculate the local induction from CFD were to be used, the differences seen here between the local inductions from the model models and global induction from CFD would be resolved. A clearer picture could be seen then for the inductions themselves. Another step in this direction would be to see the induction distribution back calculated using the loading from the CFD as an input. This would further clarify and add credence to the results seen in this study by cross checking the induction based on the loading. This would in a way bypass the unreliable estimate of the induction from the CFD results. As has been seen the averaging method used with the CFD results is not the most reliable method in terms of resolving the effect of large sources of vorticity such as the root and tip vortex.

- A more abrupt change in the loading distribution is a better test case for the coupled model since the performance deteriorates for large sections of the blade being modified. It is recommended to compare the results for such a case with CFD simulations but special care needs to be paid to any convergence issues which may arise for such abrupt changes. However this would be a good reference for a comparison with a flap like surface. Lastly, a geometry with vortex generators can also be analyzed to see the impact of simply changing the lift curve instead of the chord as has been done in this study.

Bibliography

[1] Larsen HH and Petersen LS. *DTU International Energy Report 2014: Wind energy - drivers and barriers for higher shares of wind in the global power generation mix*. DTU National Laboratory for Sustainable Energy, 2014.

[2] International Electrotechnical Commission et al. IEC 61400-1: Wind turbines part 1: Design requirements. *International Electrotechnical Commission*, 2005.

[3] Glauert H. Airplane propellers. In *Aerodynamic theory*, pages 169–360. Springer, 1935.

[4] Madsen HÅ and Rasmussen F. A near wake model for trailing vorticity compared with the blade element momentum theory. *Wind Energy*, 7(4):325–341, 2004.

[5] Pirrung GR, Madsen HÅ, Kim T, and Heinz J. A coupled near and far wake model for wind turbine aerodynamics. *Wind Energy*, 2016.

[6] Bak C, Zahle F, Bitsche R, Yde A, Henriksen LC, Nata A, and Hansen MH. Description of the DTU 10 MW Reference Wind Turbine. *DTU Wind Energy Report-I-0092*, pages 1–138, 2013.

[7] Schepers JG. Engineering models in wind energy aerodynamics. *Aerospace Engineering. Delft University of Technology*, 2012.

[8] Hansen MO. *Aerodynamics of wind turbines*. Routledge, 2015.

[9] Glauert H. *The analysis of experimental results in the windmill brake and vortex ring states of an airscrew*. HM Stationery Office, 1926.

[10] Madsen HÅ, Bak C, Døssing M, Mikkelsen RF, and Øye S. Validation and modification of the Blade Element Momentum theory based on comparisons with actuator disc simulations. *Wind Energy*, 13(4):373–389, 2010.

[11] Himmelskamp H. *Profiluntersuchungen an einem umlaufenden Propeller*. Max-Planck-Institut, Gottingen, 1950.

[12] Hansen MO and Madsen HÅ. Review Paper on Wind Turbine Aerodynamics. *Journal of Fluids Engineering*, 133(11):114001, 2011.

[13] Wilson RE and Lissaman PB. *Applied Aerodynamics of Wind Power Machines*. Oregon State University, 1974.

[14] Fiedel M. Induction modelling of heavily loaded wind turbine rotor blades with aerodynamic add-ons (Unpublished master thesis). 2015.

[15] Madsen HÅ, Bak C, Døssing M, Mikkelsen R, and Øye S. Validation and modification of the blade element momentum theory based on comparisons with actuator disc simulations. *Wind Energy*, 13(4):373–389, 2010.

[16] Schepers JG, Heijdra JJ, Foussekis D, Øye S, Rawlinson SR, Belessis M, Thomsen K, Larsen T, Kraan I, Visser B, et al. Verification of European wind turbine design codes; final report. *Netherlands Energy Research Foundation ECN*, 2002.

[17] Hansen MO, Sørensen NJ, Voutsinas S, Sørensen N, and Madsen HÅ. State of the art in wind turbine aerodynamics and aeroelasticity. *Progress in Aerospace Sciences*, 42(4):285–330, 2006.

[18] Sanderse B, Pijl SP, and Koren B. Review of computational fluid dynamics for wind turbine wake aerodynamics. *Wind Energy*, 14(7):799–819, 2011.

[19] White FM. Fluid Mechanics. 5th Ed. *Boston: McGraw-Hill Book Company*, 2003.

[20] Sumer BM. Lecture Notes on Turbulence: Revised/Updated 2007. 2007.

[21] Boussinesq J. *Théorie de l'écoulmnent tourbillonnant et tumultuex des liquides dans les lits rectilignes à grande section*, volume 1. Gauthier-Villars, 1897.

[22] Vermeer LJ, Sørensen JN, and Crespo A. Wind turbine wake aerodynamics. *Progress in Aerospace Sciences*, 39(6-7):467–510, 2003.

[23] Katz J and Plotkin A. *Low-speed aerodynamics*, volume 13. Cambridge University Press, 2001.

[24] Anderson J. *Fundamentals of Aerodynamics*. McGraw-Hill Education, 2010.

[25] Phillips WF and Snyder DO. Modern Adaptation of Prandtl's Classic Lifting-Line Theory. *Journal of Aircraft*, 37(4):662–670, jul 2000.

[26] Leishman JG. Challenges in modelling the unsteady aerodynamics of wind turbines. *Wind Energy*, 5(2-3):85–132, 2002.

[27] Winckelmans GS and Leonard A. Contributions to Vortex Particle Methods for the Computation of Three-Dimensional Incompressible Unsteady Flows. *Journal of Computational Physics*, 109(2):247–273, dec 1993.

[28] Beddoes TS. A near wake dynamic model. In *Aerodynamics and Aeroacoustics National Specialist Meeting. Papers and Discussion*, pages 1–9, 1987.

[29] Pirrung GR, Riziotis V, Madsen HÅ, Hansen MH, and Kim T. Comparison of a Coupled Near and Far Wake Model With a Free Wake Vortex Code. *Wind Energy Science Discussions*, pages 1–28, 2016.

[30] Wang T and Coton FN. A high resolution tower shadow model for downwind wind turbines. *Journal of Wind Engineering and Industrial Aerodynamics*, 89(10):873–892, 2001.

[31] Andersen PB, Gaunaa M, Bak C, Buhl T, and Poulsen NK. *Advanced Load Alleviation for Wind Turbines using Adaptive Trailing Edge Flaps: Sensoring and Control*. PhD thesis, Risø-PhD, 2010.

[32] Pirrung GR, Madsen HÅ, and Schreck S. Trailed vorticity modeling for aeroelastic wind turbine simulations in stand still. *Journal of Physics: Conference Series*, 753(4):042007, 2016.

[33] Larsen TJ and Hansen AM. How 2 HawC2, the user's manual. Technical report, Risø National Laboratory, 2007.

[34] DTU 10 MW reference wind turbine project site. `http://dtu-10mw-rwt.vindenergi.dtu.dk/`. Last Accessed: 2016-12-15.

[35] Bak C and Andersen PB. Three-dimensional corrections of airfoil characteristics based on pressure distributions. 2015.

[36] Guntur S and Sørensen NN. An evaluation of several methods of determining the local angle of attack on wind turbine blades. *Journal of Physics: Conference Series*, 555(1):012045, 2014.

[37] Shen WZ, Mikkelsen R, Sørensen JN, and Bak C. Tip loss corrections for wind turbine computations. *Wind Energy*, 8(4):457–475, 2005.

[38] Branlard E, Dixon K, and Gaunaa M. *An improved tip-loss correction based on vortex code results*. European Wind Energy Association (EWEA), 2012.

[39] Larsen TJ, Larsen GC, Madsen HÅ, Thomsen K, and Markkilde PS. Comparison of measured and simulated loads for the siemens SWT 2.3 operating in wake conditions at the Lillgrund wind farm using HawC2 and the dynamic wake meander model. 2015.

[40] Barlas TK, Zahle F, Sørensen NN, Gaunaa M, and Bergami L. Simulations of a rotor with active deformable trailing edge flaps in half-wake inflow: Comparison of EllipSys 3D with HawC2. *Proceedings of EWEA 2012 - European Wind Energy Conference; Exhibition*, 2:1058–1070, 2012.

[41] Larsen GC, Larsen TJ, and Madsen HÅ. The nature of wind turbine fatigue loads in wind farms. *Proceedings of the 2013 International Conference on Aerodynamics of Offshore Wind Energy Systems and Wakes (icowes2013)*, pages 450–459, 2013.

[42] Madsen HÅ, Mikkelsen R, Sørensen NN, Hansen MO, Øye S, and Johansen J. Influence of wind shear on rotor aerodynamics, power and loads. *Risø*, pages 101–116, 2007.

Appendix A

CFD simulations with Turbulent Flow

It was seen that the EllipSys CFD results with a TI of 10% to model free transition from laminar to turbulent flow were more close to the turbulent results. This indicated that since the same criteria was used to generate the airfoil polars, it is likely that for a TI of 10% the polars are more turbulent even though they are said to have been obtained for laminar flow with free transition. Because of this it is worth seeing how the model results fare against the CFD results for fully turbulent flow seeing that the models rely on the airfoil polars to calculate loads to see

CFD simulations with Coning

Axial Induction factors
The first plots show the axial induction factor a plotted against the radial location along the blade for two wind speeds. The title of the following plots shows the wind speed and the identifier for the flow conditions used in CFD, 't' stands for fully turbulent flow over the rotor. The plots show that the induction value fits well with CFD for both BEM and the coupled model except for the root sections. Furthermore, the effect of the tip vortex is seen in the aerodynamic models with a large induction at the tip, this is not represented in the induction from the CFD simulations as seen in Figures 5.3a and 5.3b.

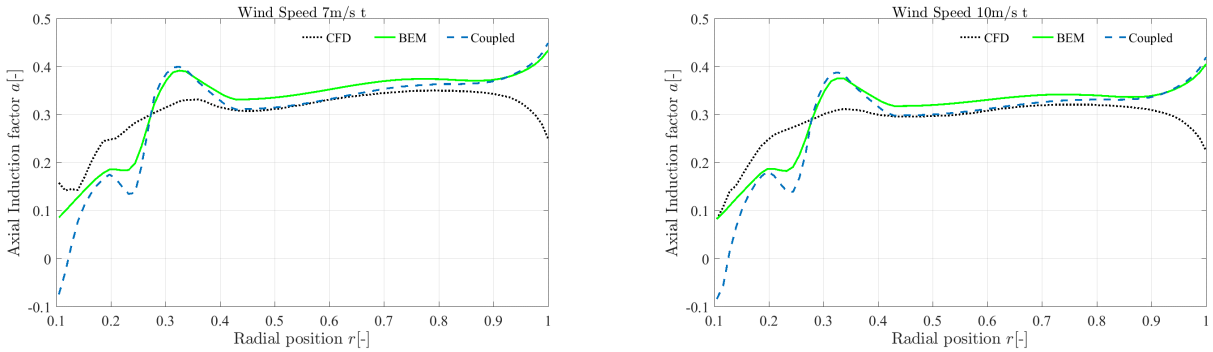

(a) 7 m/s

(b) 10 m/s

Figure A.1: Axial induction factor comparison for plain rotor with coning

The difference at the tip again lies in the difference between local and global induction and the presence of the tip vortex. To make a fair comparison the tip loss factor is multiplied. The Figures A.2a and A.2b show these results. From both these plots it is seen that the coupled model is fits better than BEM. Interestingly, the difference

between CFD and coupled model for the turbulent flow case is lower. This is further clarified with the delta plot shown in Figure A.3.

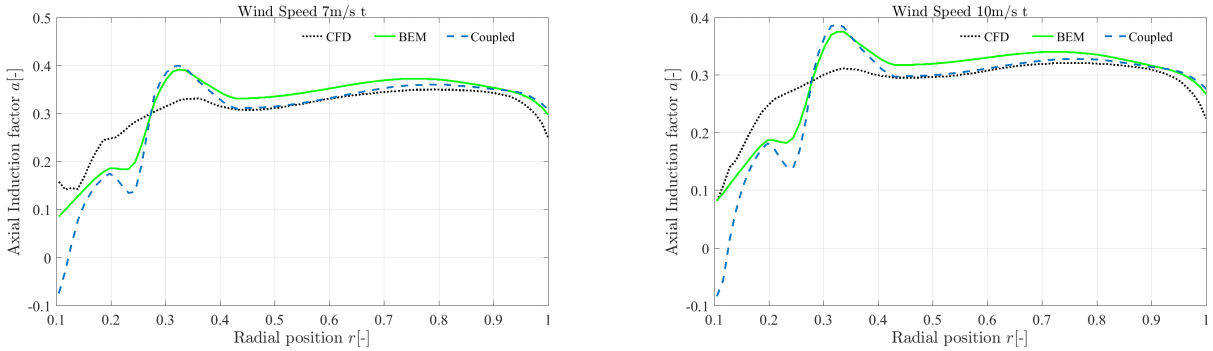

(a) 7 m/s

(b) 10 m/s

Figure A.2: Axial induction factor comparison for plain rotor with coning and tip loss multiplied

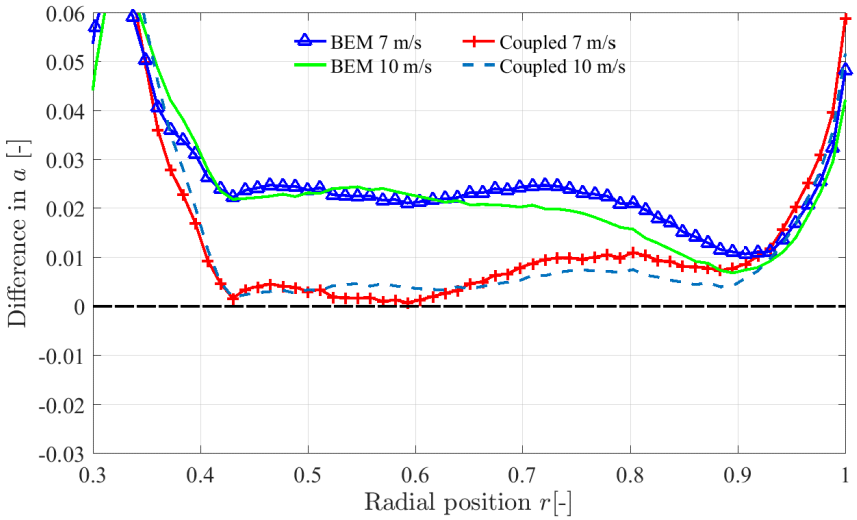

Figure A.3: Difference in axial induction at 7 m/s and 10 m/s with tip loss factor multiplied

Out-of-plane loads

Next, a comparison of the out-of-plane loads through the two models is shown with CFD in Figures A.4a and A.4b for fully turbulent flow. The coupled model in this case overestimates the loads and the BEM seems to be closer to the CFD results in this case. Delta plot shows the performance of both the models as compared to CFD in Figure A.5. Other than the tip (owing to the coning angle) the model shows a clear improvement as compared to CFD.

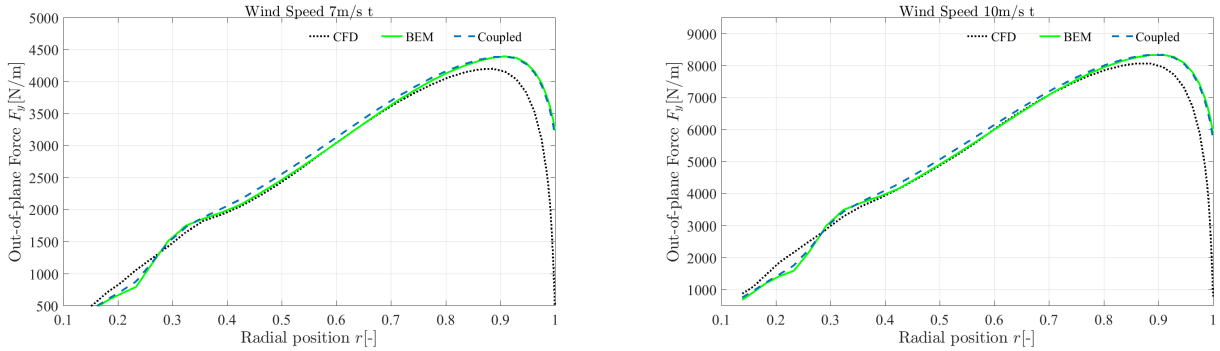

(a) 7 m/s (b) 10 m/s

Figure A.4: Out of plane loads comparison for plain rotor with coning

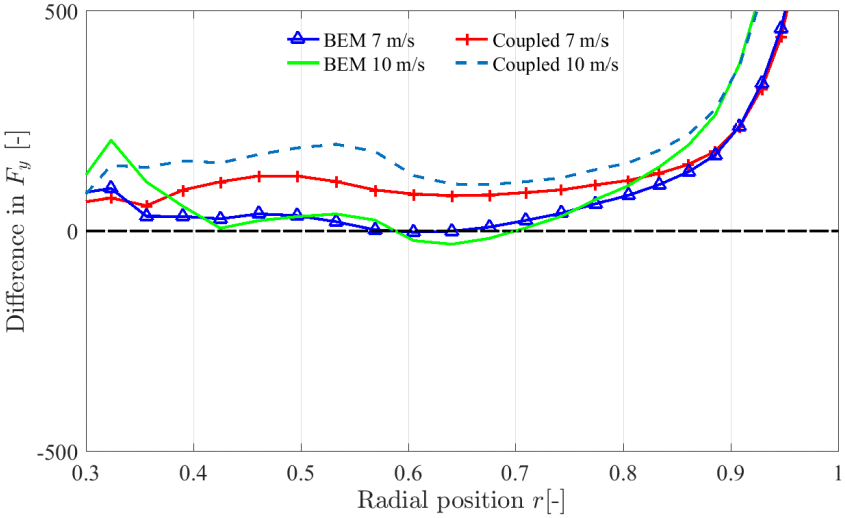

Figure A.5: Out-of-plane loads difference at 7 m/s and 10 m/s

In-plane loads

The in plane loads are plotted against the non-dimensional radial position and compared in Figures A.6a and A.6b and here a significant difference is seen with the coupled model as the original BEM model is seen to have a constant deficit in comparison to the CFD results. The CFD results lie in between the coupled model and BEM however the delta plot shows the coupled model is closer as compared to the BEM generally in this case. Both the models however tend to higher values than CFD at the tip owing to the coning angle as was seen for the laminar flow condition as well.

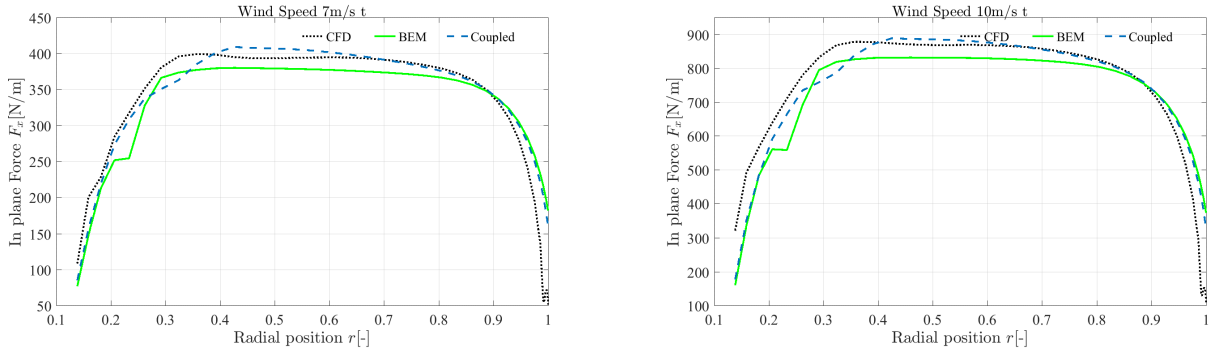

(a) 7 m/s

(b) 10 m/s

Figure A.6: In plane loads comparison for plain rotor with coning

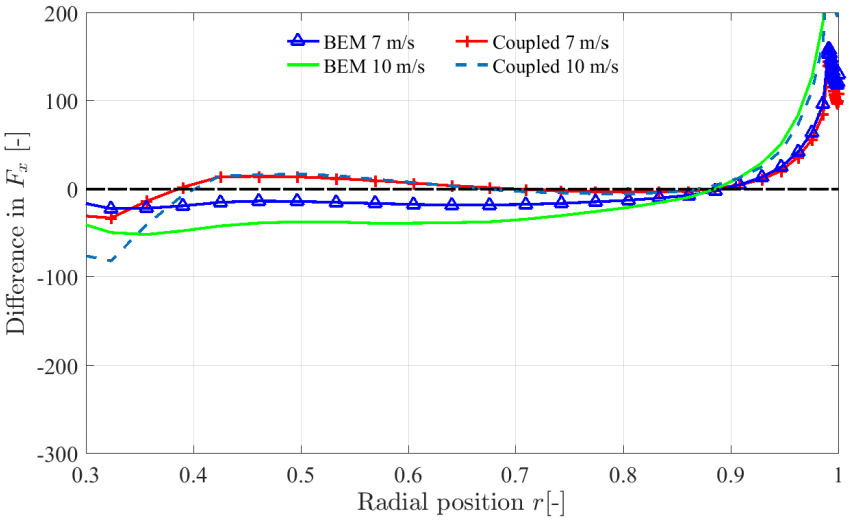

Figure A.7: In plane loads comparison at 7 m/s and 10 m/s

CFD simulations without Coning

In this section the results are presented in the same sequence as in the previous section with a few changes wherein the wind speed of 10 m/s is replaced with a high wind speed case of 25 m/s.

Axial Induction factors

The axial inductions are shown first as the direct outputs of the aerodynamic models in Figure A.8. The Figures A.9a and A.9b show the axial induction factor a after multiplication with the tip loss factor. The results are presented in the form of absolute difference through Figure A.10. for 25 m/s, because of the root vortex, the coupled model sees a high induction near the root which is not resolved by either BEM or CFD. The BEM does not see this large induction because it does not capture vorticity effects because of the way it is formulated. CFD does not see the effect of the root vortex because of the averaging method described before.

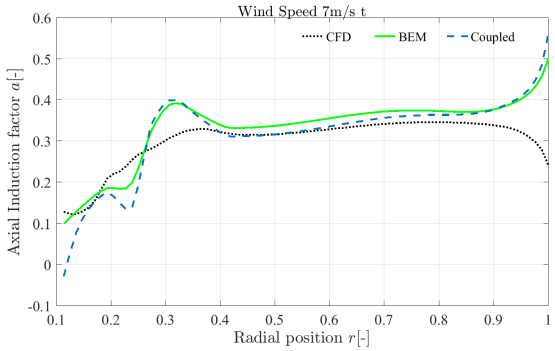

(a) 7 m/s

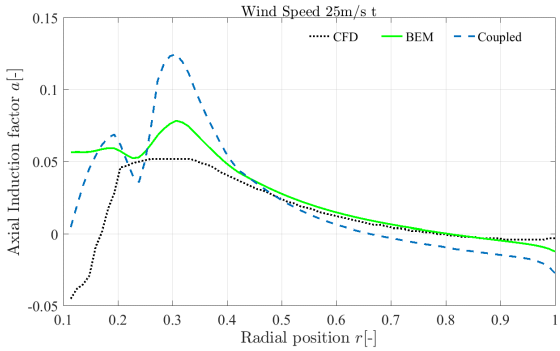

(b) 25 m/s

Figure A.8: Axial induction factor comparison for plain rotor without coning

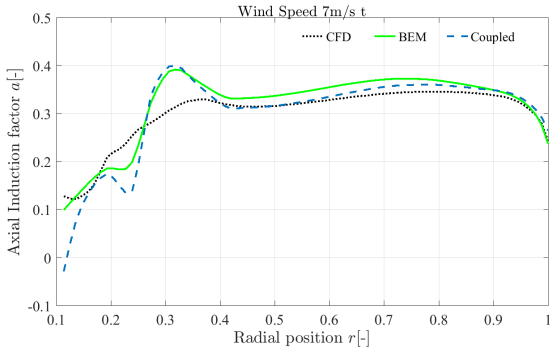

(a) 7 m/s

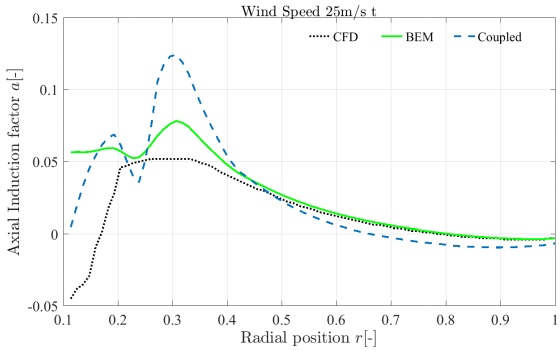

(b) 25 m/s

Figure A.9: Axial induction factor comparison for plain rotor without coning

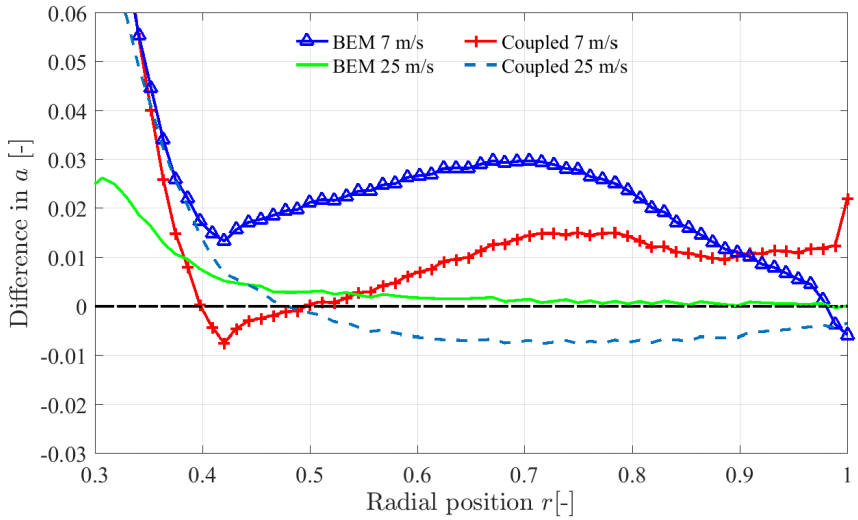

Figure A.10: Difference in axial induction at 7 m/s and 25 m/s with tip loss factor multiplied

Out-of-plane loads

Next, a comparison of the out-of-plane loads through the two models is shown with CFD in Figures A.11a and A.11b. It is seen that the coupled model agrees very well for the turbulent flow case with no rotor coning considered in the CFD simulations. There is only a slight overestimation at the tip but apart from that the coupled model fits the CFD results better than was seen for the flow with laminar conditions. This is further seen with the delta plot and here the high wind speed case can also be seen to perform well with the difference being less than BEM for a larger section of the blade. For the low wind speed and high loading case, the coupled model results almost lie on top of the reference line of CFD.

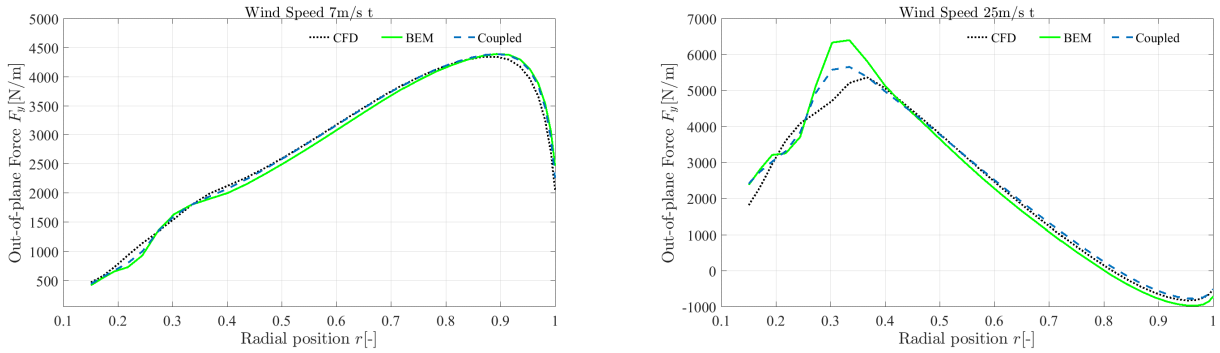

(a) 7 m/s (b) 25 m/s

Figure A.11: Out of plane loads comparison for plain rotor without coning

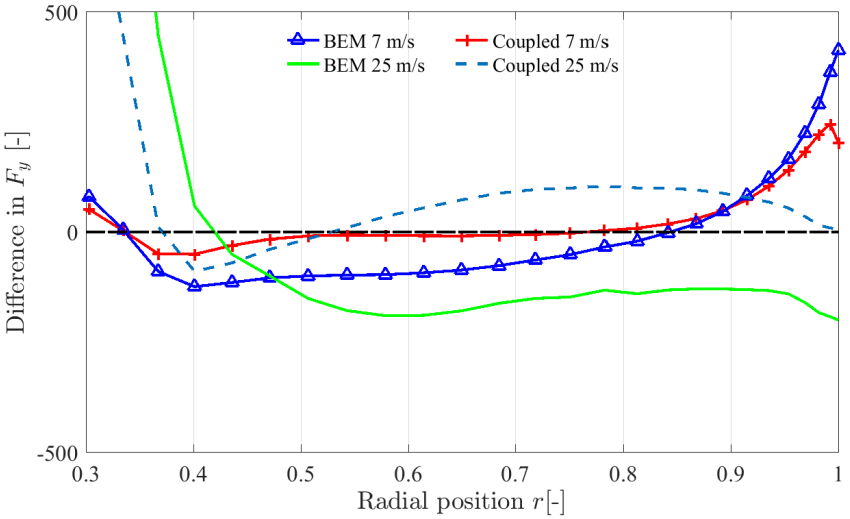

Figure A.12: Out-of-plane loads difference at 7 m/s and 25 m/s

In-plane loads

The in plane loads are presented next plotted against the non-dimensional radial position and compared in Figure A.13. The results in this case show again that for the turbulent flow results, the coupled model agrees very well with the CFD results as is seen through Figure A.14.

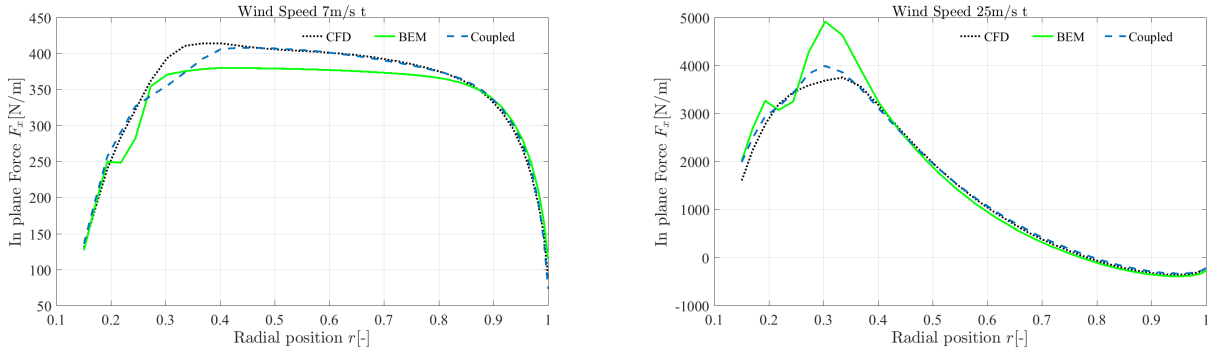

(a) 7 m/s

(b) 25 m/s

Figure A.13: In plane loads comparison for plain rotor without coning

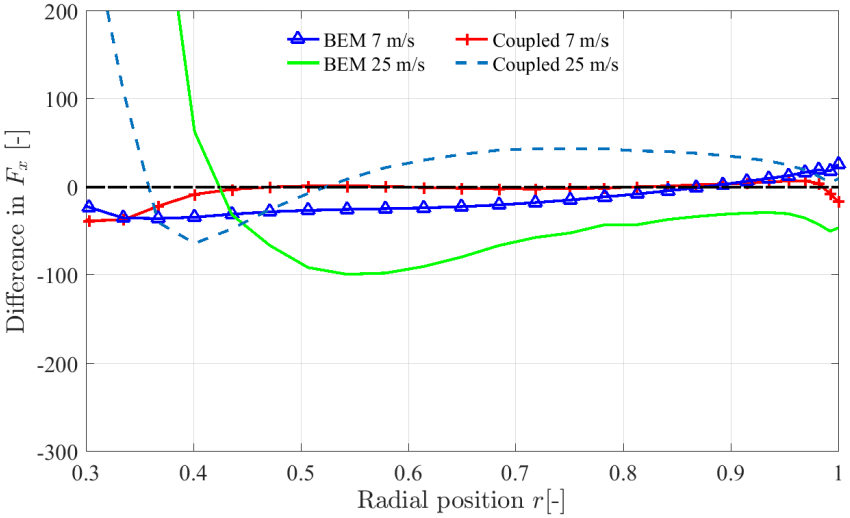

Figure A.14: Difference in In plane loads at 7 m/s and 25 m/s

Concluding remarks

The results presented here have shown that certainly in some instances, the results for the turbulent flow CFD simulations are better approximated with the aerodynamic models used. It was plausible looking at the results for the EllipSys 3D comparison that the difference between EllipSys results for transition and turbulent conditions is not as significant as the difference in the results for the CFD runs carried out in this study. Alternatively, the transition in the CFD results presented for comparison is modeled using very small values of the background turbulence to specify the turbulence intensity. The laminar flow with free transition EllipSys CFD results used to determine the airfoil polars consider a turbulence intensity of 10% at the rotor which is considerably higher than the turbulence considered for the laminar case CFD runs here. This added certain plausibility to comparing the turbulent simulations with the model results and as has been seen, the results are significantly improved if the turbulent CFD simulations are considered.

For the case with a coning angle it was seen that the out of plane loads are slightly worse than for the clean case however the in plane loads were almost unchanged compared to the results presented in Chapter 5. However, with the results for the straight rotor without any coning angle a great improvement is seen for the in and out of plane loads

with the coupled model nearly coinciding with the CFD results for almost the entire blade. Even for the high wind speed case it is seen that the coupled model clearly outperforms the BEM and also in the root section it is seen that the coupled model is closer to the estimation of CFD results. A more detailed study needs to be done however to make the most reliable comparison which would require the airfoil polars to be obtained through the same type of CFD solver with similar conditions as the flow conditions for the 3D simulations. This would at least remove uncertainties related to the source of the data. However, a large portion of the uncertainty in the BEM results comes from the accuracy of the airfoil polars themselves and therefore a method which would improve the accuracy of these polars would be even more useful for improving the accuracy of the end result.

Appendix B

Tangential Inductions

This chapter presents the omitted tangential induction results for the different cases. The inductions for the no coning angle, followed by the four modified geometries and ending with the abrupt change geometry comparison of the two aerodynamic models alone.

Rotor without coning angle

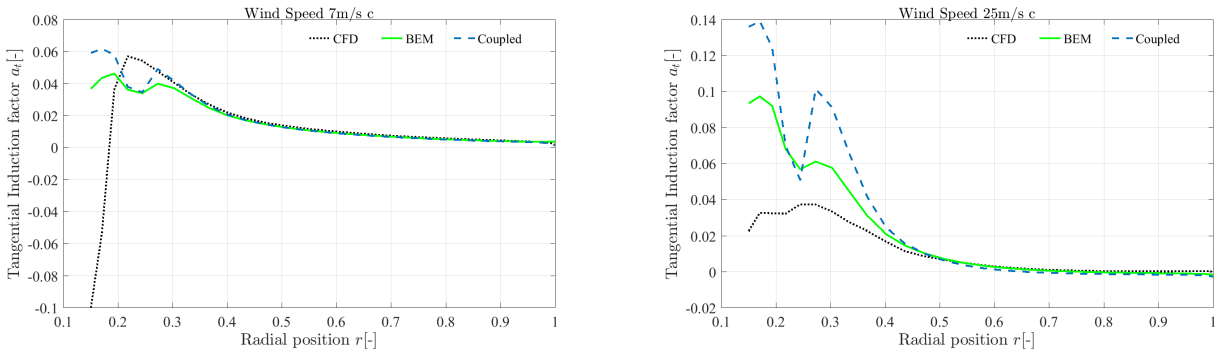

(a) 7 m/s

(b) 25 m/s

Figure B.1: Tangential induction factor comparison for plain rotor without coning

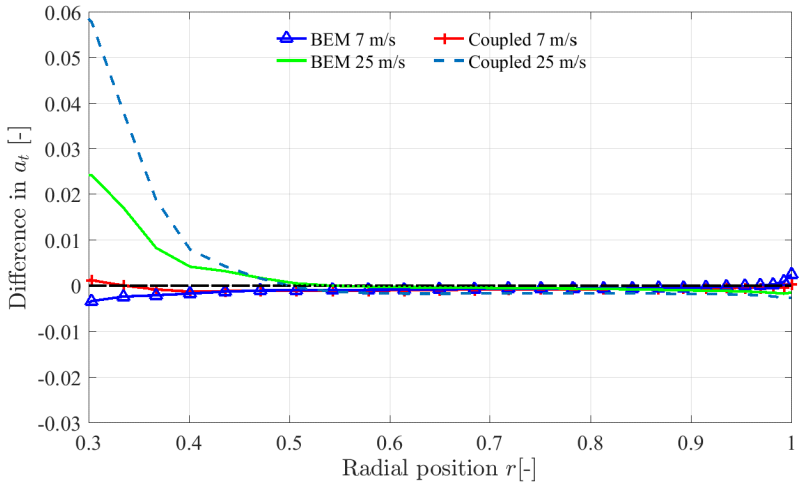

Figure B.2: Difference in tangential induction at 7 m/s and 25 m/s

Local A geometry with 10% local chord increase

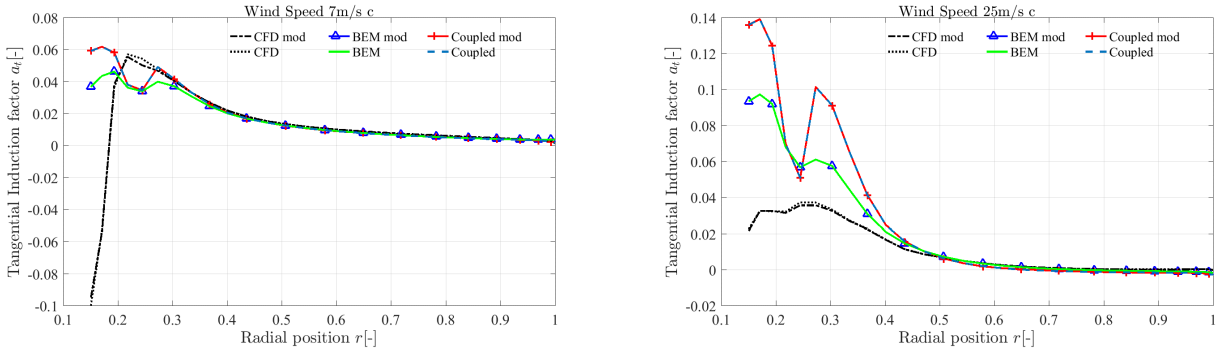

(a) 7 m/s

(b) 25 m/s

Figure B.3: Tangential induction factor comparison for geometry *Local A*

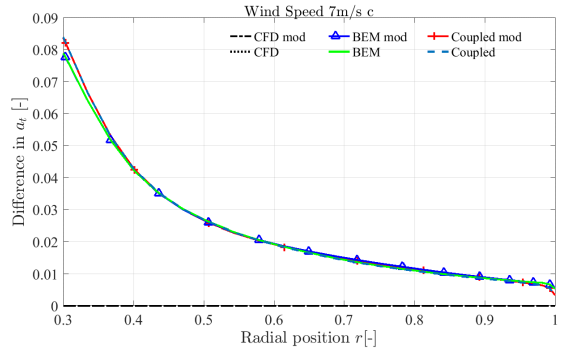

(a) 7 m/s

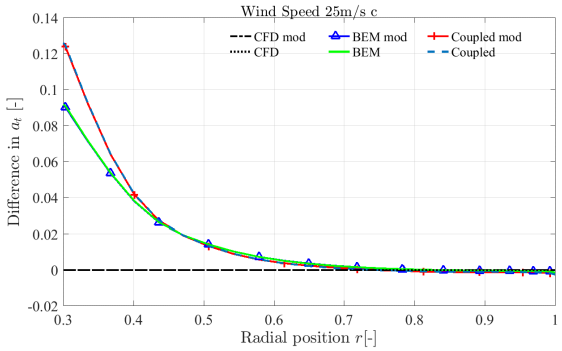

(b) 25 m/s

Figure B.4: Difference in tangential induction at 7 m/s and 25 m/s for *Local A* geometry

Local B geometry with 20% local chord increase

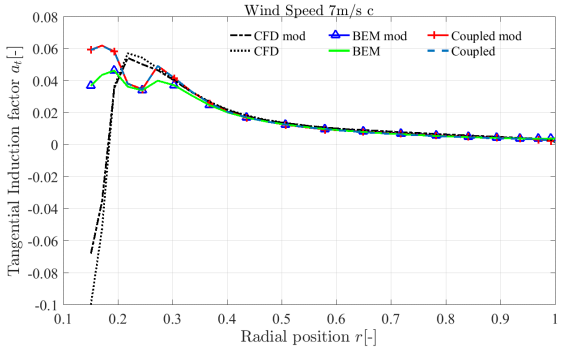

(a) 7 m/s

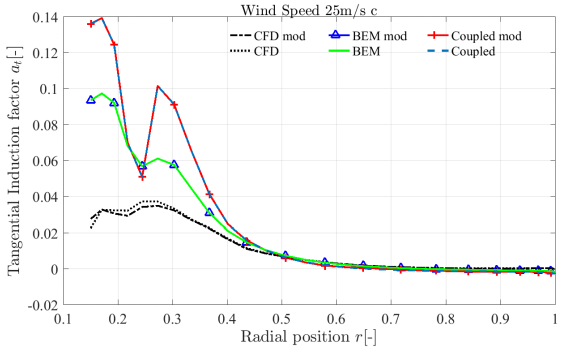

(b) 25 m/s

Figure B.5: Tangential induction factor comparison for geometry *Local B*

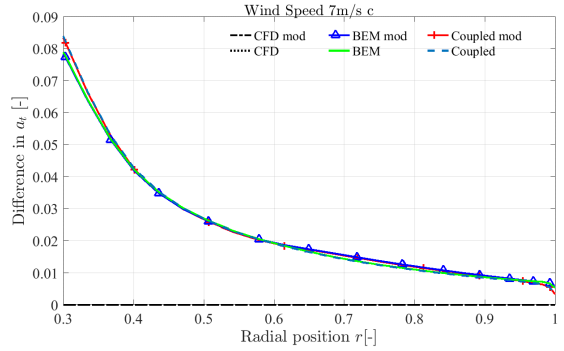

(a) 7 m/s

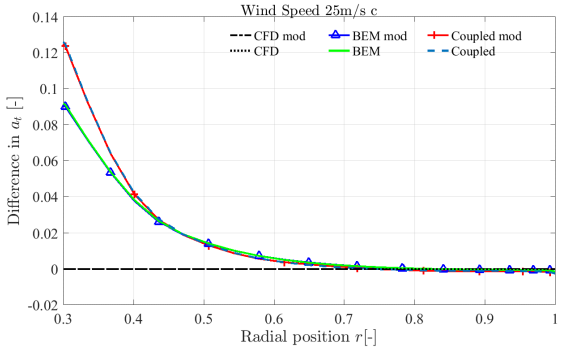

(b) 25 m/s

Figure B.6: Difference in tangential induction at 7 m/s and 25 m/s for *Local B* geometry

Slender A geometry

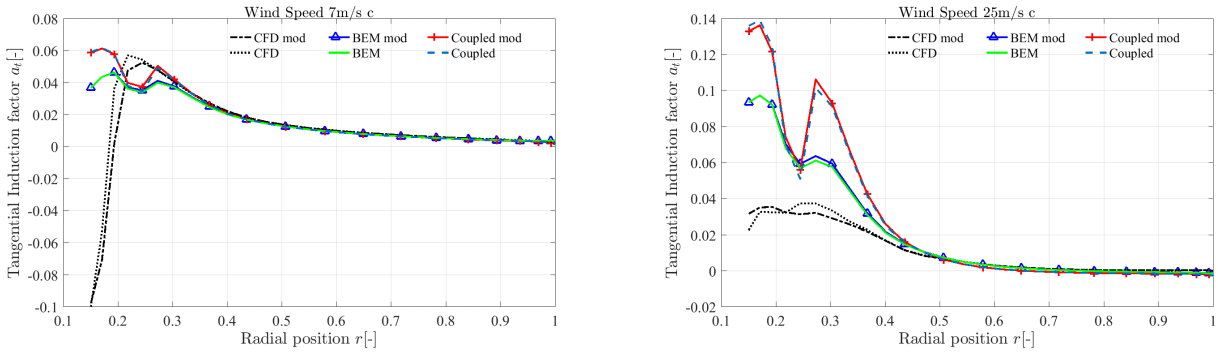

(a) 7 m/s (b) 25 m/s

Figure B.7: Tangential induction factor comparison for geometry *Slender A*

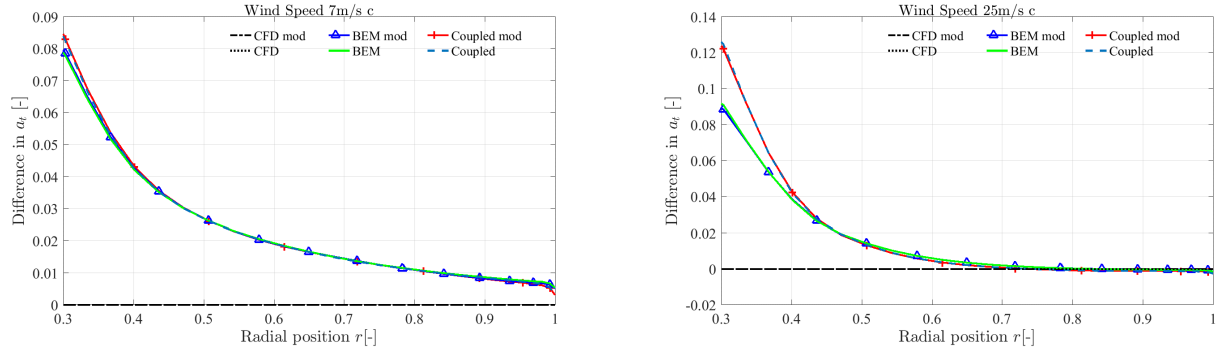

(a) 7 m/s (b) 25 m/s

Figure B.8: Difference in tangential induction at 7 m/s and 25 m/s for *Slender A* geometry

Slender B geometry

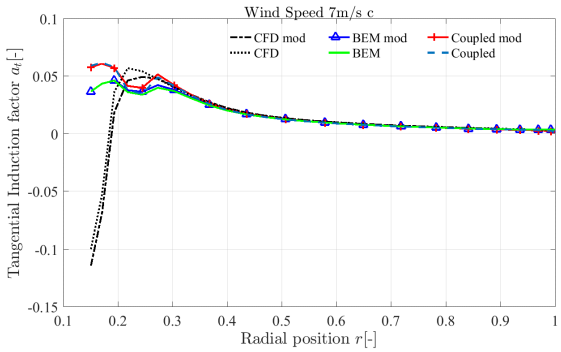

(a) 7 m/s

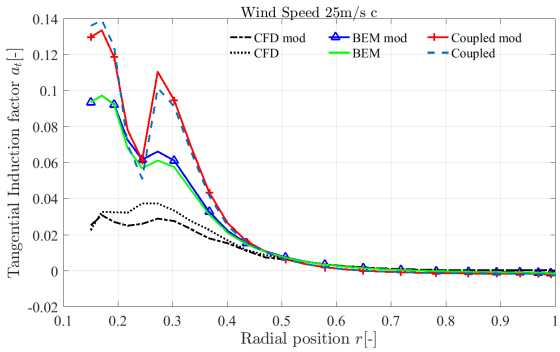

(b) 25 m/s

Figure B.9: Tangential induction factor comparison for geometry *Slender B*

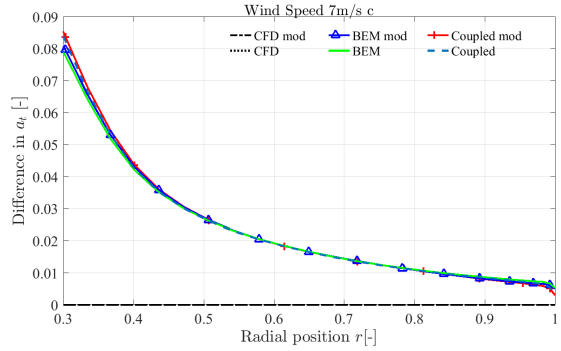

(a) 7 m/s

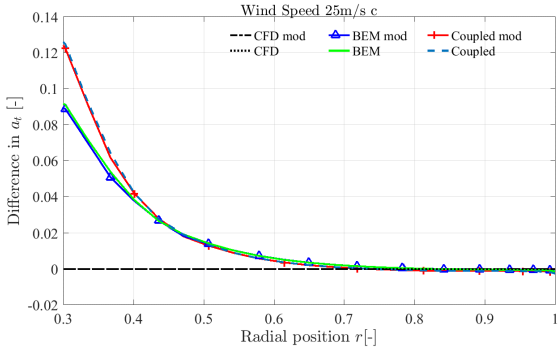

(b) 25 m/s

Figure B.10: Difference in tangential induction at 7 m/s and 25 m/s for *Slender B* geometry

Geometry with abrupt chord increase

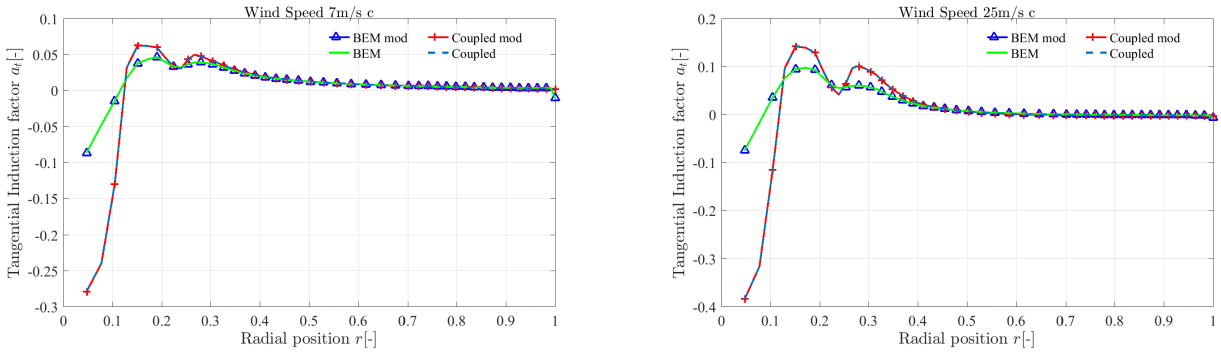

(a) 7 m/s

(b) 25 m/s

Figure B.11: Tangential induction factor comparison for geometry with abrupt chord increase

Concluding remarks

It can be seen from all the presented results that there is unanimously a great match for all three methods in the tangential inductions. Differences, if any, exist only in the root section of the blade and this is partly owing to the thick airfoils that are used for this rotor in the root sections. Additionally, the performance of the BEM in the root sections has always been skeptical at best and thus the NWM which also relies on the BEM in some major ways also has questionable results because of this causal relationship. The case with and without coning both show that the tangential inductions lie on top of each other indicating that the changes in the tangential induction added due to coning may be so small that they are irrelevant on the grand scale of things. Because the magnitude of the tangential induction is so small it is anyways quite difficult to see changes in the induction and in the larger context of things the tangential induction is not that important anyways as the main focus of most studies has been the axial induction factor as this has a larger implication and impact through the BEM method. For the different geometries that are tested in this study, it is seen that for the local geometries the only negligible difference lies where the difference in chord takes place. The rest of the inductions for the three models are almost identical for the plain and modified geometry. Even after the modification, the difference is very small. The slender blade geometries *Slender A* and *Slender B* see a larger difference in the inductions at the root sections but this is because the geometry changes in this region. The differences along the rest of the blade if any are also likely because of the changes in geometry but these are very small changes and almost negligible so nothing significant can be said about the consequence of these differences and results.